UNIVERSITÀ
DEGLI STUDI
DI PADOVA

Università di Padova

Dipartimento di Fisica G. Galilei

SCUOLA DI DOTTORATO DI RICERCA IN
SCIENZA ED INGEGNERIA DEI MATERIALI
CICLO XXIII

# TWO DIMENSIONAL SELF ASSEMBLY OF NANOSPHERES, A VERSATILE METHOD FOR NANOFABRICATION

**Direttore della Scuola:** Ch.mo Prof. Gaetano Granozzi

**Supervisore:** Ch.mo Prof. Giovanni Mattei

**Dottorando:** Giovanni Perotto

*"If I have seen further*
*it is only by standing on the shoulders of giants."*

*Isaac Newton*

# Contents

# List of Figures

# Abstract

Nanotechnology is one of the most innovative and multidisciplinary fields in modern research. Techniques to manipulate and control matter at the nanometric scale, giving the possibility to change the morphology and the physical and chemical properties are growing in number. At the nano scale, changing the morphology implies changing also the properties of matter: many properties are no longer intrinsic but they depend on the size, shape, and even on the environment. One of the most striking example is given by gold and silver colour when they are in the nanoparticle form. Gold, for example could be vine-red or green, or bluish or black simply by changing the morphology of the particles. Appropriate manipulation of the matter could also give birth at new proprieties such as the transmission of light through holes much smaller that the light wavelength, allowing the possibility to control at a very intimate scale the propagation of light.

It is clear that to exploit the great potential of nanotechnology it is important to have nanofabrication techniques that have a very precise control on the production of nanometric materials or materials with nanometric structures. There are many technologies that can produce structures with an outstanding resolution of just a few nanometer (Electron Beam Lithography, Focused Ion Beam). These technologies are "serial" fabrication tool, they can produce one object at time and this means high costs and low throughput. On the other hand parallel technologies derive from the semiconductor industry and are mostly optical lithographic methods that are limited by the diffraction limit of light ($\approx 200nm$).

In this thesis work the need for a nanofabrication tool that can allow the production of smaller nanostructures will be addressed by using a nanofabrication tool that meets the following criteria:

- parallel processing
- low cost
- large area processing ($\sim$cm$^2$)

- scalability
- reproducibility
- easy implementation

We choose to exploit the ability of self aggregation of matter in ordered structures. In particular we exploited the tendency of spherical monodisperse nanoparticles to assemble in ordered, close packed structures known as colloidal crystals. One monolayer of such colloidal crystal is a very interesting structure because it has a well ordered array of pores among the particles that have a well defined size and shape, that could be tuned by simply changing the size of the self assembled colloidal particles.
A simple and easy method to create and deposit on different substrate these self assembled monolayer of polystyrene nanoparticles will be presented. Monolayers will be used to synthesize arrays of monodisperse plasmonic nanoparticles with a very good control on their size and shape, allowing the tuning of the plasmonic proprieties on the desired application. We will use the array of plasmonic nanoparticles to realize molecular sensors and to amplify the Raman signal by the Surface Enhanced Raman Scattering effect. We will study the rise in temperature induced by illumination with a laser light resonant with the nanoparticle's plasmonic transition. This information could be very interesting for the biological application of the nanoparticles arrays since temperature variation in such a very complex environment could have relevant effect.
Moreover we will use these 2D colloidal crystal to synthesize different kinds of nanostructures like an array of holes in a metal film. This nanostructure is very interesting since the discovery of its ability to transmit light even if the hole size is much smaller than the light's wavelength. A synthesis method based on self assembled nanospheres could be useful for the fabrication of such nanostructures because of its high flexibility in changing the nanoparticles size and so the array geometric parameters like hole size and the lattice period.
Self assembled monolayers will be used as a template for the synthesis of nanostructured thin films of $TiO_2$. Titania is a semiconductor of great technological interest in many different fields: catalysis, energy conversion, gas sensing. We will fabricate using the same technology two different nanostructured thin film: a macroporous thin films and a surface patterned with a nanobowl pattern. Finally we will demonstrate the use of self assembled monolayers coupled with a standard technology used in the semiconductor industry such the ion implantation. Nanometric patterns will be produced on Si wafers using the ordered

monolayer as a mask for the ion beam.

# Abstract

Il campo delle nanotecnologie è uno dei più innovativi e multidisciplinari della ricerca moderna. Sempre più numerose diventano le tecniche per manipolare la materia su scala nanometrica, modificando così le proprietà fisico, chimiche e morfologiche a livelli mai raggiunti prima. Alla nano scala la manipolazione morfologica è accompagnata dal cambiamento delle proprietà che smettono di essere intrinseche della materia ma diventano dipendenti da altri fattori come la forma, la dimensione e l'ambiente in cui le nanostrutture sono immerse. Uno dei casi più eclatanti è il colore dell'oro e dell'argento quando sono sottoforma di particelle nanometriche. L'oro, ad esempio, può essere di colore rosso-vino, verde, blu e nero, semplicemente cambiando la forma o l'ambiente attorno ad esso. Manipolando la materia opportunamente possono comparire nuove proprietà come la trasmissione della luce attraverso aperture che sono molto più piccole della lunghezza d'onda della luce, dando la possibilità di ottenere il controllo della propagazione della luce ad un livello molto intimo. Si può capire quindi come per poter sfruttare le enormi potenzialità offerte dalle nanotecnologie sia importante avere tecnologie di fabbricazione che permettano un preciso controllo nella produzione di oggetti nanometrici o con strutture nanometriche. Le tecnologie al momento disponibili che permettono di creare strutture con precisione molto elevata (pochi nanometri) sono tecnologie "seriali" come l'Electron Beam Lithography o il Focused Ion Beam. Queste tecniche sono limitate alla produzione di un oggetto alla volta e quindi comportano costi elevati e lunghi tempi. Le tecnologie "parallele" derivano dall'industria dei semiconduttori e sono tecniche litografiche che hanno come limite la risoluzione della luce utilizzata ($\approx 200nm$).
In questo lavoro di tesi si cercherà di dare risposta alla domanda di tecniche di fabbricazione di strutture nanometriche utilizzando una tecnica che abbia le seguenti caratteristiche:

- quickness
- low cost

- ability to synthesize very small nanostructures
- reproducibility
- easy implementation

Si è scelto di utilizzare la capacità della materia di organizzarsi spontaneamente in strutture ordinate. In particolare si è sfruttata la tendenza di nanoparticelle sferiche di polistirene ad impaccarsi in strutture compatte ed ordinate costituendo dei "cristalli colloidali". Un singolo strato di nanosfere autoassemblate è una struttura interessante perché presenta dei pori tra le particelle di forma e dimensioni ben definite, che possono essere modificate cambiando le dimensioni delle sfere che costituiscono il cristallo bidimensionale.
Verrà illustrato un metodo semplice e rapido per ottenere questi monostrati di particelle ordinate e per poterli depositare su vari substrati. Questi cristalli bidimensionali verranno utilizzati per depositare una matrice ordinata di nanoparticelle plasmoniche, con un ottimo controllo sulla loro forma e dimensioni, consentendo di realizzare particelle con proprietà su misura per l'applicazione desiderata. Verranno anche studiate applicazioni di queste nanoparticelle come sensori di molecole e per amplificare il segnale raman grazie all'effetto SERS. Verrà inoltre studiato l'aumento di temperatura di queste nanoparticelle quando vengono illuminate da un laser risonante con la loro risonanza di plasma di superficie. Per applicazioni spettroscopiche applicate a sistemi biologici il cambiamento di temperatura può avere effetti rilevanti in un ambiente complesso come quello biologico.
In seguito verrà dimostrato come questi cristalli colloidali bidimensionali possono essere utilizzati per creare altre classi di nanostrutture, come ad esempio una matrice di buchi nanometrici in un film metallico. Queste strutture sono studiate da quando è stato scoperta la loro capacità di far trasmettere attraverso strutture che sono molto minori del limite di diffrazione per le lunghezze d'onda trasmesse. Una sintesi che si basa sulle nanosfere autoassemblate può essere interessante per queste strutture grazie alla sua intrinseca flessibilità. Si possono infatti cambiare in modo molto semplicei parametri geometrici che caratterizzano la matrice di buchi quali le dimensioni dei buchi e il periodo degli stessi.
Un'altra tipologia di nanostrutture che verrà realizzata sono film sottili nanostrutturati di $TiO_2$. La titania è un semiconduttore di grande interesse tecnologico in molti campi diversi: dalla catalisi, alla conversione di energia ai sensori di gas. Verranno fabbricati, con la stessa tecnologia, dei film con una

porosità ordinata e delle superfici nanostrutturate con un motivo a incavi.
Infine verrà dimostrata la possibilità di utilizzare i cristalli colloidali 2D accoppiati con una tecnologia molto utilizzata dall'industria dei semiconduttori quale l'impiantatore ionico. Pattern nanometrici verranno realizzati su silicio utilizzando le nanoparticelle autoassemblate come maschera per il fascio ionico.

# Chapter 1

# Self Assembly

There are several reasons for interest in self assembly [1]. Self-assembly is one of the few practical strategies for making ensembles of nanostructures. It will therefore be an essential part of nanotechnology. Manufacturing and robotics will benefit from applications of self-assembly. Self-assembly is common to many dynamic, multicomponent systems, from smart materials [2] and self-healing structures [3] to computer networks [4, 5]. Finally, the focus on spontaneous development of patterns bridges the study of distinct components and the study of systems with many interacting components. Humans are attracted by the appearance of order from disorder. The cell also offers countless examples of functional self-assembly that stimulate the design of non-living systems. Living cells self-assemble, and understanding life will therefore require understanding self-assembly. It thereby connects reductionism to complexity and emergence.

There are two main kinds of self-assembly: static and dynamic [6]. Static self-assembly involves systems that are at global or local equilibrium and do not dissipate energy. For example, molecular crystals are formed by static self-assembly; so are most folded, globular proteins. In static self-assembly, formation of the ordered structure may require energy (for example in the form of stirring), but once it is formed, it is stable. Most research in self-assembly has focused on this static type. In dynamic self-assembly, the interactions responsible for the formation of structures or patterns between components only occur if the system is dissipating energy. The patterns formed by competition between reaction and diffusion in oscillating chemical reactions are simple examples; biological cells are much more complex ones. The study of dynamic self-assembly is in its infancy. In the presence of template, interactions between the components and regular features in their environment determine the structures that form. Crystallization on surfaces that determine the morphology of the crystal is one example; crystallization of colloids in three-dimensional optical fields is another.

### 1.0.1 Common Features of Self-Assembly

Self-assembly reflects information coded (as shape, surface properties, charge, polarizability, magnetic dipole, mass, etc.) in individual components; these characteristics determine the interactions among them. The design of components that organize themselves into desired patterns and functions is the key to applications of self-assembly. The components must be able to move with respect to one another. Their steady state positions balance attractions and repulsions. Molecular self-assembly involves non covalent or weak covalent interactions (van der Waals, electrostatic, and hydrophobic interactions, hydrogen and coordination bonds). In the self-assembly of larger components meso- or macroscopic objects interactions can often be selected and tailored, and can include interactions such as gravitational attraction, external electromagnetic fields, and magnetic, capillary, and entropic interactions, which are not important in the case of molecules. Because self-assembly requires that the components be mobile, it usually takes place in fluid phases or on smooth surfaces. The environment can modify the interactions between the components; the use of boundaries and other templates in self-assembly is particularly important, because templates can reduce defects and control structures. Equilibration is usually required to reach ordered structures. If components stick together irreversibly when they collide, they form a glass rather than a crystal or other regular structure. Self-assembly requires that the components either equilibrate between aggregated and non-aggregated states, or adjust their positions relative to one another once in an aggregate.
This work is focused on self assembly of colloidal particles into ordered monolayer of nanospheres (NS) deposited on a substrate. We exploited the order induced proprieties of the monolayer to produce ordered array of nanostructures with well defined size and shape. Results are presented in chapter 2. We also studied this system for the ease in obtaining ordered structures, aiming to transfer the order to other systems. Patterning of the substrate on which nanospheres are deposited, or synthesis of ordered features in thin film of technological relevant materials such as $TiO_2$ are the presented in 4.

## 1.1 Methods of self assembly

Self assembly of colloidal nanoparticles made of $SiO_2$ or polystyrene (PS), can be performed using several techniques, each with different variables that will affect the overall size, shape, and uniformity of the nanostructures.
The main method to produce a good assembly of silica nanospheres is a controlled evapo-

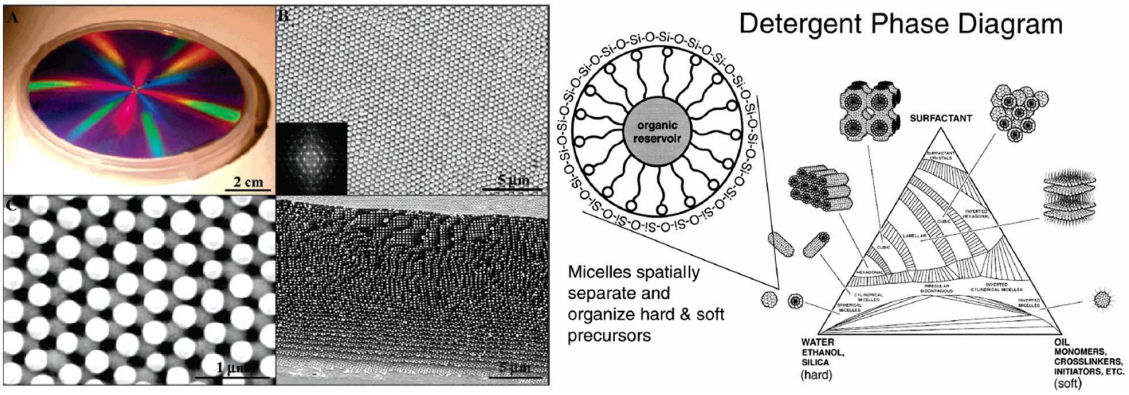


**Figure 1.1:** Left: *sample made by spin coating self assembly, as reported by Jiang and McFarland [8].* Right: *phase diagram of surfactant-oil-water system. Hydrophobic and hydrophilic precursors partition the system in micelles, and evaporation promotes further self assembly, from [7].*

ration of nanospheres in solution, that can also provide a great variety of nanostructures, by changing the medium and the presence of surfactants [7]. It has the capability of obtaining very good colloidal crystals, but the fabrication takes very long time.

### 1.1.1 Evaporation-induced Self Assembly

This approach built upon earlier studies on the fundamentals of colloidal crystallization [9, 10, 11], where it was shown that colloidal particles will spontaneously assemble into ordered structures under the appropriate conditions. By careful drying, such crystals can be collected as dry, compact, crystalline packings that are sufficiently robust to be further processed. This material, often referred to as a synthetic opal due to its similarities to natural gemstone opals, is a photonic crystal namely a material with a periodic variation of the dielectric proprieties, with period comparable to the light wavelength. They can also serve as a template to synthesize other photonic structures. Unfortunately, these sedimented opals contain numerous defects such as vacancies, dislocations, stacking faults, and grain boundaries. In particular, sedimented opals are polycrystalline, reducing their usefulness in photonic applications. To improve this situation, more recent researches have explored alternative approaches to form synthetic opals. This has included colloidal crystallization on pre-patterned substrates, between narrowly spaced plates, and in the presence of various external fields. However, the approach that is most relevant to our discussion here is that of Colvin and co-workers,[12] who have reported a simple method (discussed in detail below) to obtain thin opaline films from colloidal spheres less than

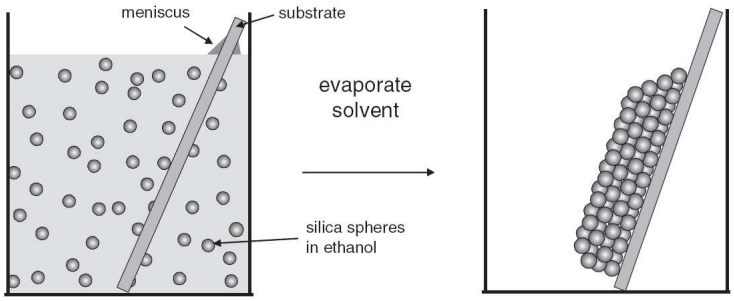


**Figure 1.2:** *Self Assembly of silica nanoparticles from diluted dispersion as described by Colvin et al [12]. Opaline film can be formed by slow evaporation*

400 nm in diameter. Such planar opals are extremely attractive as templates for photonic bandgap materials since they can be single crystals that contain defect densities that are significantly lower than in sedimented opals.
As these materials are in a technology-friendly format (a thin coating deposited directly on a silicon wafer) and are mechanically robust (constructed from silicon), they are potentially useful for applications.

The mechanism that underlies the Colvin method and its extension to large colloidal spheres is not fully understood. Although qualitative explanations have been proposed, a detailed picture has not emerged. In the laboratory, the general procedure, which is depicted in figure 1.2, involves placing a nearly vertical substrate in a suspension of colloidal spheres (typically 1 vol.%). Under the proper conditions, evaporation of the solvent leads to the deposition of an ordered three-dimensional packing of more or less uniform thickness on the substrate, starting from a position below the initial level of the contact line at the top of the meniscus. After the opaline film is dried, the silica spheres adhere well enough to each other, and to the substrate that the film can be easily handled (or even re-immersed in solvent) without detaching or dissolving. With spheres smaller than 400 nm, successful conditions are relatively easy to achieve. The solvent (typically water) is simply evaporated slowly from the suspension at room temperature. However, for larger spheres, this simple approach is unsuccessful. The spheres sediment quickly and are not deposited. Later [13], it was discovered that opals could be formed from larger spheres under a different set of conditions. A more volatile solvent (ethanol) was chosen and a temperature gradient was applied to the vessel. Unfortunately, in this case, successful conditions exist only in narrow ranges of initial particle concentration, substrate inclination, temperature, temperature gradient, gas-phase confinement, gas-phase replacement, etc. Initially, this led to a process that produces opals that are relatively small in area ($< 1cm^2$) and with low yield ($< 10\%$). Although this situation has improved dramatically,

a detailed understanding of the underlying process is still not available. If obtained, it could not only allow the above process to be optimized or improved, but may also yield interesting information about self-assembly processes in general.

### 1.1.2 Spin Coating

Gravity sedimentation, electrostatic repulsion, template assisted assembly, physical confinement, capillary forces induced convective self-assembly, and electric field induced assembly, have been developed to create colloidal crystals with millimeter to centimeter-size single- or poly-crystalline domains in a time period from days to weeks. Although these techniques are favorable for low volume, laboratory-scale production, their scaling-up to an industrial-scale mass-fabrication seems unfeasible due to their tedious fabrication processes and incompatibility to the wafer-scale batch microfabrication widely used by the semiconductor industry. In addition, these methods lead to either nonuniform or noncontrollable crystalline thickness over large-area. These restrictions also greatly impact the mass-fabrication and practical applications of another two types of technologically important materials as macroporous polymers and polymeric nanocomposites, as most of their fabrication methods involve the preformation of colloidal crystals as structural scaffolds. Spin coating is by far the most fast technique to create self assembly of nanospheres. In principle it is possible to control the thickness, in terms of number of layers, of the resulting sample adjusting properly the spin coating parameters: concentration of nanoparticles in the dispersion, speed of the rotation, evaporation rate of the solvents. P. Jiang and M. J. McFarland [8] obtained extraordinary results. They could obtain single, double, multilayer colloidal crystal of nanospheres with an outstanding quality.
Wafer-scale samples, that are at least 1 order of magnitude larger than current available ones, can be routinely fabricated in minutes. The resultant planar samples have highly uniform thickness, which can be easily adjusted by changing the spin speed and time. They could also show that patterns with micrometerscale resolution can be created using standard semiconductor microfabrication techniques for potential device applications.

Spin coating of volatile colloidal dispersions has been widely used in preparing colloidal masks for "natural lithography" [14]. However, only thin-layer samples (typically 1-2 layers) with centimeter-sized area can be created and the resultant polycrystalline samples have poor crystalline qualities. Well-ordered multilayer colloidal crystals have been made by spin-coating of submicron spheres within pyramid-shaped etch pits [15]. A combination technique of centrifugation and spin-coating has been developed to assemble centimeter-sized colloidal crystals with tapered thickness profile. Jiang and Mc Farland

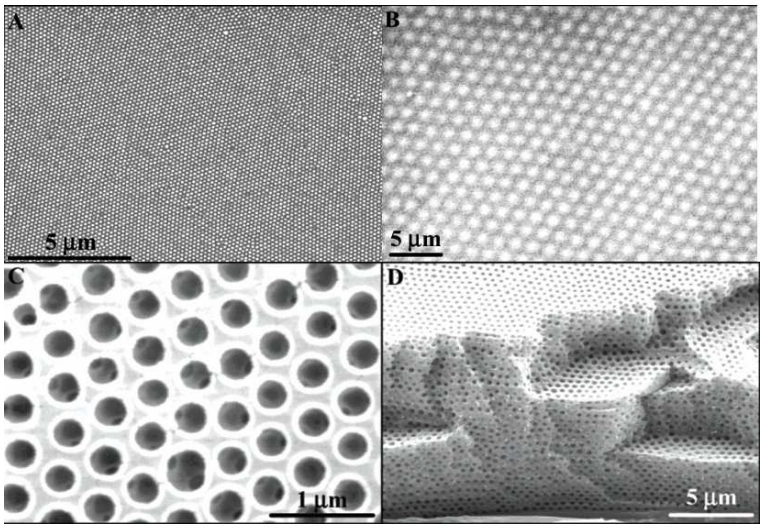


**Figure 1.3:** *Self Assembly of silica nanoparticles by spin coating from a concentrated dispersion.* (A)*: a sample made from 130 nm diameter spheres;* (B) *a sample made from 1320 nm diameter spheres;* (C) *and* (D) *are high and low magnification of a nanocomposite film after the removal of the silica nanoparticles. From [8].*

disperse uniform silica colloids in viscous and nonvolatile monomers, ethoxylated trimethylolpropane triacrylate (ETPTA), with 1% Darocur 1173 as photoinitiator to make a final particle volume fraction of 19.8%. The spin-coating technique described here has a number of advantages over previous self-assemblies. First of all, it is rapid and highly manufacturable. Four-inch-diameter planar crystal (81 $cm^2$, 1.4), which is an order of magnitude larger than currently available ones, can be routinely made in minutes; whereas early methods take days or even weeks to produce a centimeter-size crystal. The wide particle diameter range achievable with this technique is another advantage over previous methods, as quick gravitational sedimentation of large silica spheres (¿400 nm) causes serious problems in making high-quality crystals. From the well-known sedimentation equation, $v = (2/9)(R_s^2 \Delta\rho g/\eta)$, ($R_s$ is the sphere radius, $\Delta\rho$ is the density difference between silica and solvent, $\eta$ is the solvent viscosity), we can estimate that the sedimentation velocity of silica in ETPTA is about 70 times slower than that in water. Given the short spin-coating and photopolymerization time (in minutes), the formidable challenge of sedimentation can be completely avoided. Using this spin-coating technique, monodisperse silica colloids with a wide diameter range from $100nm$ to $2\mu m$ can be cast to form 3D ordered nanocomposite films. Crystalline thickness is another important parameter in determining the quality of resultant crystals. Highly uniform and tunable film thickness over a large area is much favored for the simultaneous production of multiple devices on a single substrate.

Spin-coating is a well-established technique for reproducibly forming large-area, highly

uniform thickness films from viscous solutions. The film thickness (from monolayer to over one hundred colloidal layers) can be controlled easily by changing the spin speed and time. It is inversely proportional to the final spin speed and the square root of the final spin time. This agrees well with the model of spin coating of solvent free liquids, which predicts $H \approx (A/\omega\sqrt{t})$, where $H$ is the film thickness, $A$ is a constant determined by the viscosity and density of the solution, $\omega$ and $t$ are the final spin speed and time. The nanocomposite film thickness determines the number of layers of the resultant colloidal crystals and macroporous polymers, illustrated by three crystals of 2 colloidal layers (Figure 1.4A), 5 layers (Figure 1.4B) and 41 layers (Figure 1.4C) made at different spin-coating conditions. The resultant 3D ordered planar nanocomposites with well-controlled thickness are highly desirable for the development of ultrahighdensity magnetic and optical recording materials [16]. Besides providing a versatile route to create 3D ordered nanocomposites, this technique major merit is its ability to mass-fabricate planar colloidal crystals and macroporous polymers. Due to their substantial difference in chemical properties, ETPTA and silica can each be selectively removed without disturbing the structure of the other, resulting in the formation of colloidal crystals and macroporous polymers, respectively. Oxygen plasma etching is a better method than calcination to remove ETPTA, while silica spheres could be removed by HF.

The colloidal crystallization by spin-coating could be due to both shear induced ordering and subsequent monomer polymerization. Being a valuable model for probing the effect of shear flow on the generic properties of atomic systems, shear ordered colloidal crystallization has been extensively studied [17, 18, 19]. These studies have revealed a sliding layer structure at large strain amplitudes and a twined fcc structure at small ones. In a typical spin-coating experiment, the shear rates are high ($> 10^5$), resulting in a sliding layer mechanism, where 2D hexagonally packed colloidal layers are readily formed due to the coupling of the centrifugal and viscous forces. The interparticle electrostatic repulsion plays only a minor role due to the low dielectric constant of the ETPTA medium ($\approx 3$ at optical frequency). Salt effect on the colloidal crystallization process during spin coating was tested. $10^{-3}M$ tetrabutylammonium chloride was added to the silica- ETPTA dispersion to screen interparticle electrostatic repulsion and make silica colloids more "hard-sphere" like. The resultant spin-coated nanocomposite exhibits the same in-plane particle separation and optical transmission spectrum as those samples made without the addition of salt, indicating minor contribution of the electrostatic force to the colloidal crystallization. This experiment is different from previous shear-annealing studies as there is material spin-off during the spin-coating process. Colloids close to the wafer edges and surfaces experience the highest rotational velocities, thus are repelled from the wafer first. To keep the conti-

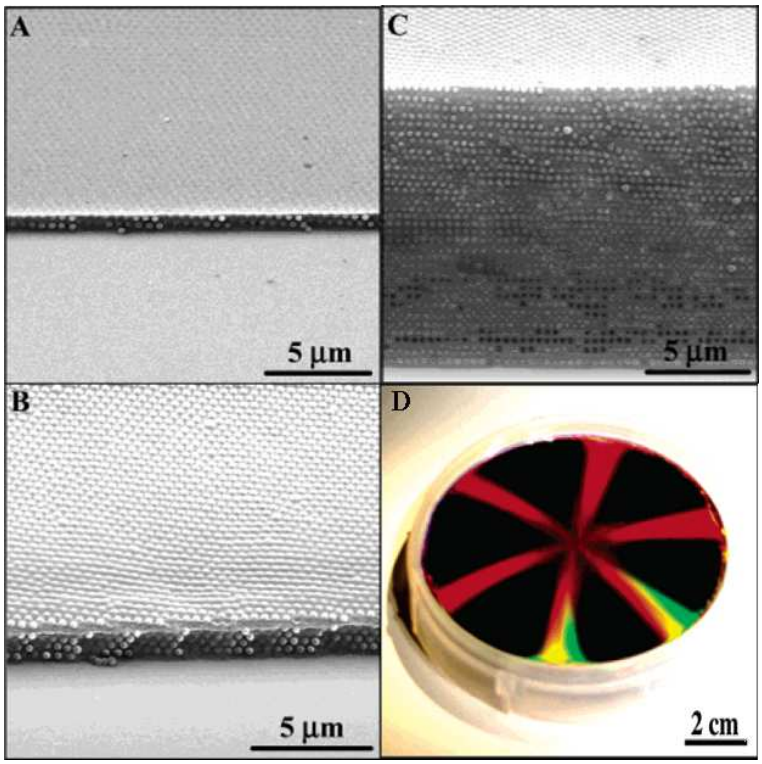


**Figure 1.4:** *Typical side-view SEM images of spin-coated nanocomposite films with different thickness.* (A) *A 2-layer sample coated at 6000 rpm for 900 s.* (B) *A 5-layer sample coated at 6000 rpm for 170 s.* (C) *A 41-layer sample coated at 600 rpm for 120 s 325 nm diameter colloids are used for all cases. From [8]*

nuity of the film, neighboring spheres move to the vacancies left by the repelled colloids, resulting in a convective radial particle flow, which leads to a pressure gradient exerted normal to the free film surface.

To make practical devices, patterning of as-synthesized nanocomposites, colloidal crystals, and macroporous polymers with micrometer regime resolution is important. The planar configuration, globally uniform thickness and wafer supported tructure of these samples allow the simultaneous construction of multiple micrometer-dimensioned patterns using two standard semiconductor microfabrication techniques, proximity photolithography and reactive ion etching (RIE). A patterned macroporous polymer film (Figure 1.5) made by proximity photolithography, shows iridescent colors, indicating the preservation of the ordered structures throughout the patterning and etching processes. When viewed at higher magnification under SEM, the regularly arranged silica spheres of patterned nanocomposite are evident. RIE can also be used to pattern polymerized nanocomposite films. Due to isotropic etching of the RIE process, slanted surfaces of ordered spheres with well-defined

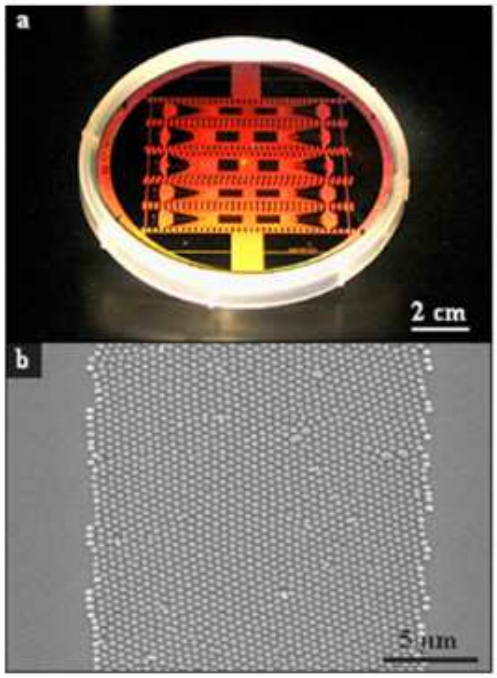


**Figure 1.5:** *Patterned monolayer of self assembled silica nanospheres by standard microfabrication.* (a) *Photograph of a micropatterned 4 in. sample.* (b) *Top-view SEM image of an* $18\mu m$ *wide line.*

angles are formed.

## 1.2 Dynamics of Self Assembly

Close-packed monolayers of colloidal spheres can be produced by stranding particles on a solid surface by evaporating or draining the solvent down to a layer that is thinner than the particle diameter. Regions of hexagonal close packing one layer thick have been produced by the simultaneous draining and drying in spin-coating and dip-coating, as well as by less controlled drying of thin drops of dilute suspension and other thin coatings. In general, these monolayers form due to the lateral capillary forces that act when the spheres protrude from the solvent. The spheres are pushed together and nucleate an ordered monolayer. Flow of solvent brings in more spheres and the monolayer grows. This effect can be utilized to deposit large-area ordered colloidal monolayers on planar substrates. It has also been shown that 3D structures could be formed by using these ideas; however the size and quality of these films was not well controlled. Later, Colvin and co-workers found an easy route (**FIGURA**) to extend these two-dimensional methods

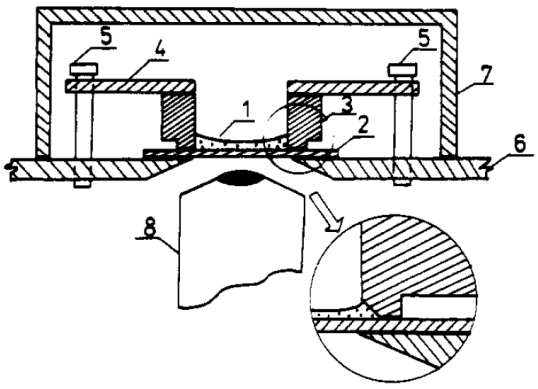


**Figure 1.6:** *Experimental Cell used to study the dynamics of 2D self assembly, from [20].*

to form three-dimensional structures.
Denkov, and co worker investigated the mechanism of 2D self assembly of sub micrometers polystyrene particles on a substrate from a water dispersion [20, 21, 22].

With a custom built setup 1.6 they could see the micrometric polystyrene beads during all the phase of self assembly, from the beginning while they are in the dispersion until the end when the self assembled monolayer is formed. In the cell, a drop of a latex suspension with a given volume and composition is placed upon the glass plate (2). The drop spreads over the accessible glass area encircled by a teflon ring. The system is mounted on the table (6) of a metallographic microscope. A $20\mu L$ drop of PS beads ($1.7\mu m$ in diameter) dispersion is spread over the bottom of the experimental cell. Volume and concentration of the cell were chosen to provide a dense monolayer after complete evaporation of the water. During the first phase the drop spread all over the stage and forms a slightly concave layer whose thickness is about $100\mu m$ at the center. Latex particles are involved in intense brownian motion and their concentration above the glass substrate is low. After several minutes, sedimentation of the beads occurs and the concentration of the particles near the glass surface become higher. When the water layer thickness becomes about $10\mu m$ fringe caused by interference between the light reflected at the two interfaces (glass-water and water air) can be observed in monochromatic light. The nanoparticles come closer and closer and often collide with each other, but no aggregation or irreversible attachment to the glass surface is noticed. At a given moment a ring shaped narrow zone of tightly packed is formed over the middle of the glass substrate. This is the onset of the growth of a well ordered array. The mean particle volume fraction in the water layer is now lower than 10% . The ordered zone is enclosed by a thicker concave meniscus. The particles located in the meniscus region begin to move toward the ordered zone, and upon reaching

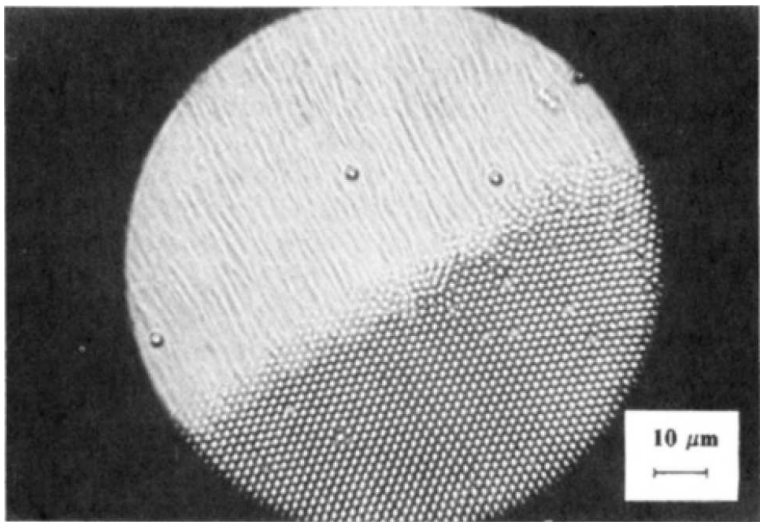


**Figure 1.7:** *Optical image of PS beads selfassemblying together, from [20].*

the boundary of the array they are incorporated into the ordered phase (Figure 1.7).

Usually, the particles are ordered in domains with hexagonal packing. Thus, the front of the ordered domain advances with time in a radial direction. Some of the particles firmly stick to the glass surface before reaching the ordered region after a certain time they are incorporated into the growing ordered monolayer but cause defects in the two-dimensional crystal. From the interference fringes it is possible to estimate the water layer thickness at the boundary of the ordered array to be slightly lower than $1.7\mu m$.

### 1.2.1 Factors affecting the array formation

Denkov et al. [20] studied the influence on self assembly of many different parameters:

- PS nanospheres size;
- Nanospheres concentration;
- Presence of electrolytes;
- Presence of surfactants;
- Water evaporation rate

*PS nanoparticles size.* Experiments were performed with latex particles of smaller diameter ($0.81\mu m$). The only difference is that the smaller particles moved faster during the stage of 2D crystal growth, but the observed phenomena seems to be very similar and the

final results seem to be qualitatively the same.
Varying the particles concentration from 0.25 to 2.5 wt % shows no substantial difference in the occurrence of the processes. When the particle concentration is higher, the area occupied by bilayers is larger; oppositely, when the particle concentration is lower, large areas free of particles are formed between the parcels covered with a particle monolayer.
*Concentration of electrolyte in water.* The polystyrene latex particles in aqueous solution bear a negative surface electrical charge due to dissociation of surface ionizable groups. To study the role of the electrostatic interactions, they added $BaCl_2$ (concentration $5 \times 10^{-4} M$) to the latex suspension. Since the $Ba^{2+}$ ions partially adsorb at the particle surface, the magnitude of the surface potential decreases. As a result, at the stage of Brownian motion a pronounced tendency for formation of transient aggregates (2-5 particles) is observed. This is certainly due to the screened electrostatic repulsion that allows the attractive van der Waals interaction to becomes operative. The aggregation is reversible, and the only difference in the resulting monolayer is that the process is slightly slower. At concentration of $BaCl_2$ higher than $2 \times 10^{-3} M$ particle coagulation in the bulk of the suspension is observed and futher water evaporation does not lead to crystal formation. Also the addition of $NaCl$ leads to suppression of electrostatic repulsion and reversible formation of aggregates, however during the stage of ordering irreversible deposition of latex particles is observed and array consisting of smaller domains are obtained. The fact that the addition of moderate concentrations of electrolyte changed significantly the $\zeta$ potential without affecting the general occurrence of the phenomenon suggests that neither electrostatic repulsion nor Van der Waals attraction between the particles is the driving force of the two-dimensional crystallization.
*The influence of surfactants*, which are known to slower the evaporation rate of water, has been also studied. Two different surfactants were tested: CTAB (Cetyl trimethylammonium bromide) and SDS (sodium dodecyl sulfate). CTAB in a concentration of $10^{-4} M$ (which is 9 time below the critical micelle concentration) reduced the speed of the directional particle motion and the rate of the 2D crystal growth. The increase in concentration leads to deposition of many particles on the glass surface which causes dislocations and other defects in the 2D crystal. At even higher surfactant concentrations ($\approx 10^{-3} M$), the particles coagulate in the bulk suspension and further water evaporation does not lead to 2D crystallization. The addition of $8 \times 10^{-3} M$ SDS to the latex suspension also slowed the dynamics of ordering. Neither particle deposition on the substrate nor coagulation was observed, and well-ordered arrays were obtained in this case.
*Water evaporation rate* was controlled by reducing the volume of the air above the suspension from 250 $cm^3$ to $\approx 1$ $cm^3$. This resulted in a strong decrease (about 1 order of

magnitude) of the rate of all process, including the speed of directional motion and the array growth. Very large and well-ordered domains were obtained, and also a large parts of the substrates were covered with bilayers and even trilayer.

### 1.2.2 Self assembly mechanism

The results reported in their paper [20] indicate that the repulsive electrostatic forces are not the principal driving forces but some other type of interactions should be considered as responsible for the 2D array formation. Indeed, the addition of electrolytes ($BaCl_2$ or $NaCl$) strongly suppresses the electrostatic repulsion without substantial changing of the ordering processes. Similarly, the change of the concentration of the latex particles does not affect the onset of the ordering. In all cases the array formation starts when the thickness of the water layer becomes approximately equal to the particle diameter and the crystal growth takes place through a directional motion of particles toward the ordered regions. A two-stage mechanism of the array formation is proposed. At the first stage a "nucleus" of ordered phase appears when the upper surface of the thinning aqueous layer in the wetting film presses the latex particles toward the water-glass interface. When spherical particles are partially immersed in a liquid layer on a horizontal solid substrate, the deformations of the liquid-gas interface give rise to strong and long-range interparticle capillary forces [21].

Let us consider two particles of radius $R$, partially immersed in a liquid layer, whose thickness tends to a constant value $l_0$ at a large distance from the two particles (see Figure 1.8). The shape of the meniscus obeys the Laplace equation of capillarity and is determined by the distance $L = 2s$ between the particles, the layer thickness $l_0$, and the value of the contact angle $\alpha$, which characterizes the particle wettability. The water level in the inner

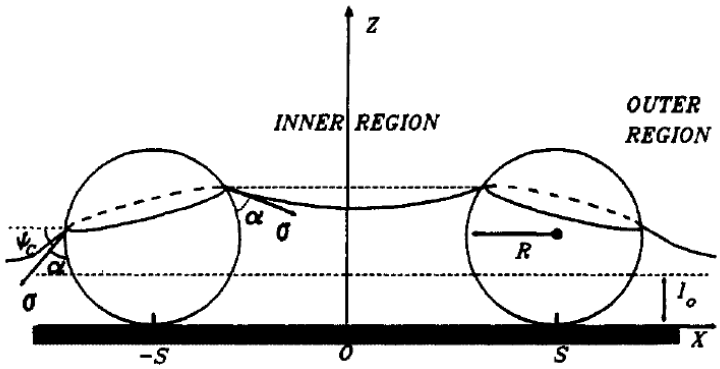


**Figure 1.8:** *Capillary Forces*

region (between the particles) is higher than in the outer region. The ensuing inclination of the three-phase contact lines at the particle surfaces gives rise to two capillary effects, both leading to attraction: *(i) pressure effect*, caused by the hydrostatic pressure higher in the gas phase than the pressure in the liquid at $z > l_0$ (especially in the inner region), this pressure difference pushes the particles toward each other; *(ii) surface force effect* due to the fact that the slope (with respect to the horizontal) of the liquid surface, and hence the $x$ component $\sigma_x$ of the surface tension force $\vec{\sigma}$, varies along the contact line. For micrometer-size and smaller particles the surface tension effect exceeds the pressure effect by many orders of magnitude [21]. The horizontal projection $F_x$ of the resulting attracting capillary force can be expressed as:

$$F_x \approx 2\pi\sigma r_c^2 (sin^2\Psi_c)(1/L) \; ; \; r_c << L << (\sigma/(\Delta\rho)g)^{1/2} \tag{1.1}$$

where $\sigma$ is the surface tension of the liquid, $r_c$ is the radius of the three-phase contact line at the particle surface, $\Psi_c$, is the mean meniscus slope angle at the contact line, $g$ is the gravitational acceleration, and $\Delta\rho$ is the difference between the mass densities of the liquid and gas phases. Capillary forces between particles partially immersed in a liquid layer on a solid substrate are so strong that the respective energy of capillary attraction can be much larger than the thermal energy, $K_BT$, even with submicrometer particles. Capillary interaction is also a long range force that extend its effect even at distances greater than 1000 particles radii distance, as plotted in 1.9.
Once the nucleus is formed, the second stage of crystal growth start through directional motion of particles toward the ordered array. The directional particle motion is caused by a convective water flux which carries along the particles toward the ordered phase (Figure 1.10). The evaporation of water leads to a gradual decrease of the liquid layer thickness with time. Until the thickness is larger than the particle diameter, it decreases uniformly. Once ordered regions are formed, the thinning of the water layer inside them is slowed due to the hydrophilicity of the particles. Indeed, the evaporation from the concave menisci between the particles, clustered in a nucleus, must increase the local curvature and hence the local sucking capillary pressure. The convective influx carries along the suspended particles toward the clusters where they remain attached to the domains, pressed by the hydrodynamic pressure of the water and captured by the capillary attraction.

By decreasing or increasing the water evaporation rate it is possible to speed up or slow down the convective transport of the small particles respectively. In agreement with the proposed mechanism, this effect can be explained by the change of curvature of the liquid menisci between the particles in the ordered nucleus. For instance, the increased evaporation decreases the level of the water between the particles and increases the curva-

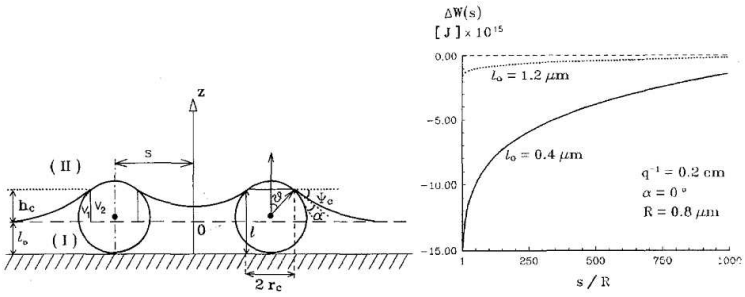


**Figure 1.9:** *Dependence of the capillary meniscus interaction energy W on the distance 2s between the centers of two similar spheres of radius R for two values of the liquid layer thickness $l_0$. When the liquid layer is thinner than the particle dimension, interaction energy is still attractive even at 1000 particles radii.*

ture of the menisci, thus rising the local sucking capillary pressure which drives the water influx toward the nucleus. In the opposite case when the level of the water between the particles is increased because of water condensation (due to some increase of the humidity of the gas inside the cell), the sucking pressure is decreased and one observes a decrease of the particle convective influx. A further increase of the humidity leads to complete stopping of the process of ordering and even to disintegration of the ordered clusters and restoration of the chaotic particle motion.

## 1.3 Nanosphere Lithography

An very interesting and powerful method for the large-scale production of surface-bound nanoparticle arrays, based on the self assembly of nanospheres, is nanosphere lithography (NSL) [23]. It is now being employed in laboratories around the world as an inexpensive, inherently parallel, high-throughput, and materials general nanofabrication technique. NSL has also been demonstrated to be well suited to the synthesis of size-tunable noble metal

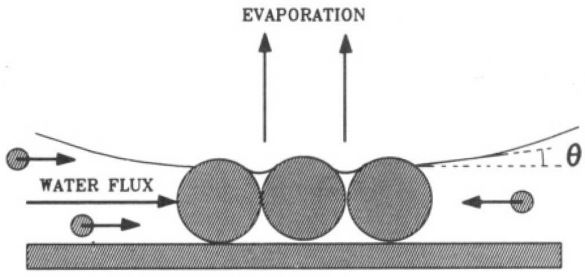


**Figure 1.10:** *Convective flux toward the ordered phase due to the water evaporation from the menisci between the particles in the 2D array*

nanoparticles in the 20 - 1000 nm range. The conventional NSL process begins with self-assembly of a nanosphere mask onto a substrate, followed by deposition of a material through the mask. The nanosphere diameters determine the size and interspacing distance of the NSL produced nanoparticles. The nanosphere used as deposition masks are usually polystyrene or silica, available in a variety of sizes (100 - 2000 nm). In general, the substrate to be patterned is positioned normal to the direction of material deposition. The resultant nanoparticles have an inplane shape and interparticle spacing determined by the projection of the nanosphere mask interstices onto the substrate. A monolayer mask produces nanoparticles having a triangular inplane shape arranged on the surface with $P_{6mm}$ honeycomb symmetry. The ratio of the interparticle spacing to the in-plane perpendicular bisector is a fixed value, ca. 2.5 .

Angle-resolved nanosphere lithography (AR NSL [24]), a simple variant on conventional NSL, produces vastly different and increasingly flexible nanostructures by controlling the angle between the surface normal of the sample assembly and the propagation vector of the material deposition beam. The nanosphere mask registry also affects the resultant nanostructure.The range of accessible structural motifs can be further expanded by performing a series of material depositions on the same sample under AR NSL conditions. Another similar fabrication method, namely, shadow nanosphere lithography, [25, 26] makes morphologies such as cups, rods, and wires by rotating the tilted nanosphere masks during deposition. Nanosphere lithography is a materials-general nanofabrication technique. A variety of materials, such as noble metal [23], magnetic materials [27], semiconductor materials [28], polymers [29], and protein [30] can be used as deposition materials in NSL.The magnetic nanostructures are currently the subject of much interest due to their enormous potential applications in high density storage. Periodic magnetic nanoparticle arrays have been successfully produced using the electrodeposition or electron beam evaporation of nickel and cobalt.

Recently, [31] NSL has been explored to fabricate metal oxide catalyst nanostructures. At present, conventional methods, such as salt precipitation, calcinations, and solid phase reactions, are the most widely used processes for fabrication of the metal oxide catalysts.The particles produced by solution methodologies, however, tend to agglomerate, are nonuniform in size and shape, and are not amenable to surface characterization by experimental techniques such as electron spectroscopy or scanning probe microscopy. To overcome those disadvantages, Lenzmann and coworkers initiated the fabrication of uniform and well ordered metal oxide nanoparticles ($Y_2O_3$) using NSL. Bullen and coworkers [28] have been able to directly grow $TiO_2$ nanoparticles on NSL masks by back-filling the vacuum chamber with $O_2$ during the evaporation of Ti. They also demonstrated that NSL

is quite general and should be applicable to growing many oxide nanoparticles on a variety of substrates including single crystals.

## 1.4 Experimental and Results

Our first attempt to produce self assembled monolayer of nanoparticles were based on the self-assembly of silica nanospheres by spin coating. To obtain good monolayers, nanoparticles must have the same size. A size dispersion less than 5% could be tolerated, while larger values cause the appearence of defects like dislocations or point defects. Monolayers have always polycrystalline domains, but self assembly of nanoparticles with different dimensions produce defective domains, smaller in size and greatly reduce the quality of the monolayer and consequently the possibility of developing applications.

We use the Stöber method for the synthesis of monodisperse silica nanospheres. [32] [33].

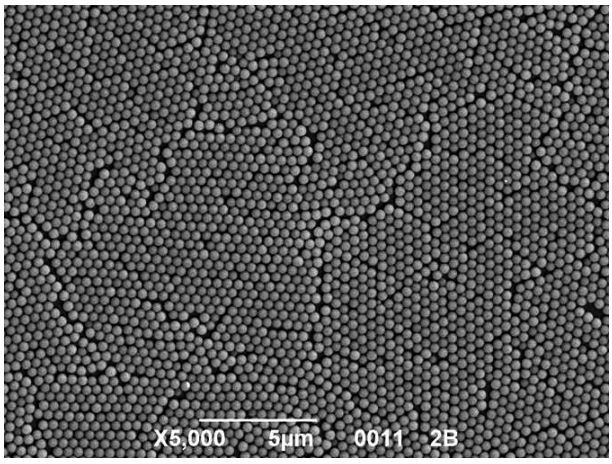


**Figure 1.11:** *600nm Silica Self assembled monolayer obtained via spin coating.*

This well known synthesis technique relies on the hydrolysis and condensation in a basic environment of a $SiO_2$ precursor: Tetraethyl orthosilicate (TEOS). Nanoparticles with a uniform and controlled size between $100nm$ and $1\mu m$ are easily obtained. Once synthesized, silica nanospheres were purified from unreacted reagents by repeated centrifugation and redispersion in clean solvent (absolute ethanol was always used as solvent) for at least four times. Aggregates of nanospheres that are possibly produced during the synthesis or caused by the centrifugation were separated by gently centrifuging the solution or letting it rest overnight. Purified nanospheres were separated as a powder and then a concentrated (20 % v/v) dispersion was prepared for spin coating. Many solvents were tested: alcohols ($CH_3-(CH_2)_n-OH$ with $n=0,1,2,3$), water, ethylene glycole, organic solvent (toluene, THF). The best results in terms of reproducibility in the spin coating and quality

of the self assembled monolayer were obtained using a mixture of 50:50 ethanol - ethylene glycole.
Typical results are presented in 1.11. The SEM image shows that a good assembly among the nanoparticles was obtained. Samples are polycrystalline with iso-oriented domains of $20 \times 20 \mu m^2$. Inside the single domain cracks among the nanospheres are present, showing just a partial packing of the nanospheres. Defects caused by impurities or dirt coming from the environment are also a significant cause of the poor quality of the monolayer. Dust, with size comparable with the silica nanoparticles, provide a preferential site for irreversible sedimentation of silica spheres producing a starting point for the growth of a domain thus leading to a more polycrystalline monolayer with smaller domains. To obtain really good results via the spin coating method it is mandatory to operate in a very clean environment (i.e. clean room) for both the synthesis and the self assembly step.
To overcome these limitations a completely different approach for self assembly was tested. We choose a method based on assembly driven by capillary forces at the meniscus between two liquid phases [27]. This method combines the capability of obtaining good quality monolayers with the ease and the speed of the self assembly creation and deposition.
The monolayers were prepared using polystyrene nanospheres with diameter from $1 \mu m$ to $100 nm$. All particles were purchased from Microparticles GmbH as a 10 % water solution. Nanospheres were dispersed as in a 50:50 water - alcohol solution to obtain a final concentration of about 5 wt. %. Various alcohols ($CH_3 - (CH_2)_n - OH$ with $n = 0, 1, 2, 3$) were tested and the best results were obtained with isopropanol. Silicon, silica and sodalime glass were used as substrate, usually cutted in $2.5 \times 2.5 cm^2$ square samples. Each substrate was cleaned in a "Piranha" solution (a 3:1 mixture of concentrated sulfuric acid with 30% hydrogen peroxide) for half an hour, rinsed with Milli-Q water ($18.2 M\Omega cm^{-1}$), and dried in a stream of nitrogen, cleaned substrate were kept in a MilliQ bath and used during the subsequent week.
To create a self assembled monolayer, $20 \mu L$ of prepared solution was applied and spread all over the cleaned substrate and then it was slowly immersed in a large glass vessel filled with Milli-Q water. PS particles self assembled at the meniscus between the alcolic dispersion and the water bath, the resulting compact monolayer floats on the water surface. This monolayer was then collected with the same substrate used to make the particles assemble together. Samples were dried at ambient temperature.
Figure 1.12 present a typical structure of such prepared mask. Self assembled layer present always polycrystalline domains, with large domains size. From SEM images at low magnification it is possible to determine the domain size by the Moir pattern formed between the mask and the image resolution (Figure 1.12).

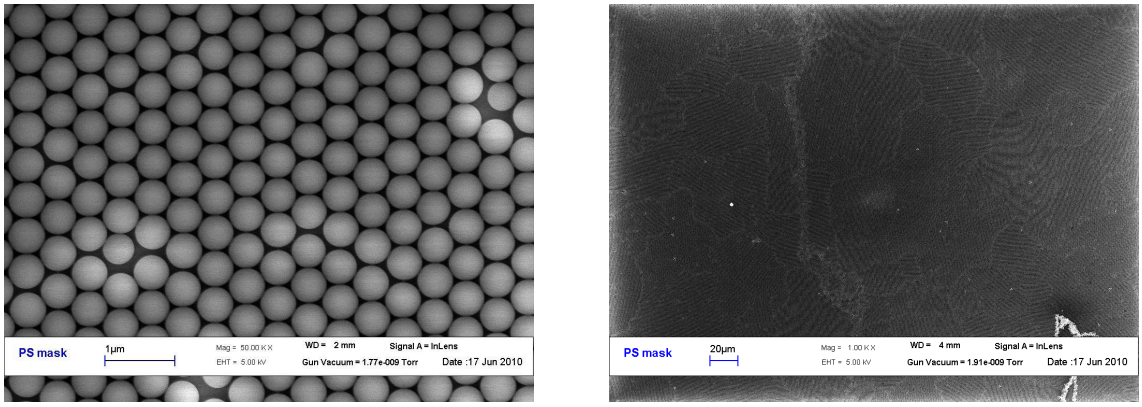


**Figure 1.12:** Left*: SEM images of a self assembled PS mask show a good assembly of the nanoparticles;* Right*: low magnification SEM image of a 900 nm PS mask, Moir pattern are visible and can be used for determining the size of domains (up to* $100 \times 100\ \mu m^2$*.*

Better results with respect to the previous self assembly method based on spin coating are obtained: PS nanospheres in the monolayer are well packed without any crack inside the single domain and the domains obtained are about $100 \times 100 \mu m^2$ large. This method relies on strong capillary forces to assure a good packing among the nanoparticles. The interaction is stronger for smaller nanoparticles ($100nm$) than for bigger nanoparticles ($1\mu m$). This reflects on the fact that monolayers produced by self assembling bigger PS spheres are slightly more difficult to obtain and are more prone to crack formation if there are any turbulences in the water bath. The main disadvantages of this method is that it has a low reproducibility. It requires the operator to manually immerse the sample. To have better and more reproducible results and a better control on the parameters like speed or angle of immersion, we used a modified version of a dip coater that can perform the self assembly of nanoparticles automatically. It consists in a slow motor at which substrate are connected through a cantilever. This is a T shaped aluminum bar on which the sample is fixed by two screws. The motor can move up and down and so we can dip and extract the substrate from the water bath. We took care to insulate the whole system from the vibration, using an heavy metal base and soft rubber feet. This system works well for the immersion of the substrate and the creation of the monolayer, but it is less effective when collecting the monolayer and extracting the substrate. When the monolayer is formed, it tends to expand on the entire free water surface, even far from the substrate, often at the end of the self assembly the floating monolayer moves from the substrate and this consequently make difficult its collection with a single axis system(up-down) like one that we use. Secondly after the monolayer is formed, residual particles remain on the clips that fix the substrate and when we use it collect the monolayer during the drying these residual

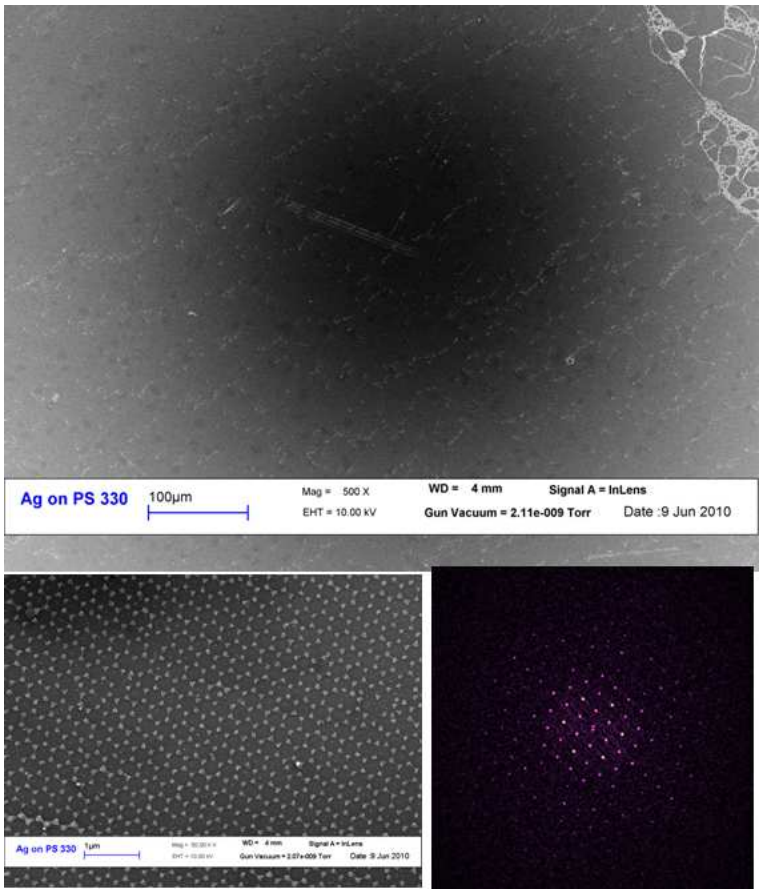


**Figure 1.13:** *SEM image of a single domain obtained from 330nm PS nanoparticles assembled with the motorized sample holder. Domain bigger than* $750 \times 750\ \mu m^2$ *are visible.*

nanoparticles can sediment over the monolayer creating a second layer. For this reason we can call this system a semi-automatic system: in fact, the creation of the monolayer is done with the use of the motor, while the collection is done manually, with another cleaned substrate. This method combine the reproducibility of the automatic dipping system with the cleanliness requirements for the applications. Better self assembled monolayer, with bigger domains and with more reproducible results could be obtained, as seen in figure 1.13. Large area ($2.5 \times 2.5 cm^2$) sample with polycrystalline monolayer and domains as big as $750 \times 750 \mu m^2$ have been synthesized using PS nanoparticles with dimension from $153nm$ to $920nm$.

# Chapter 2

# Plasmonics 2D arrays

Submicron device fabrication technologies based on optical lithography are reaching fundamental, diffraction limits as feature sizes approach $\lambda/2$. The leading nanotechnologies for suboptical (viz., 10 - 200 nm) fabrication are electron-beam lithography (EBL) and x-ray lithography (XRL). Although EBL has outstanding resolution yielding features of 1 - 2 nm in the most favorable cases, its serial processing format is a limitation to achieving commercially acceptable throughputs of $1cm^2s^{-1}$. XRL resolution is limited by photoelectron range and diffraction effects to 20 - 50 nm. However, its parallel processing capabilities that permits simultaneous fabrication of large numbers of nanostructures is an extremely advantageous feature. Deckman's "natural lithography" work [14] attracted a lot attention because of its potential as an inexpensive, parallel, "bench-top" technique capable of fabricating Ag nanostructures. Nanosphere lithography (NSL), the extension of natural lithography made by Van Duyne [23] is a simple method for the synthesis of monodisperse nanoparticles in a broad range of dimension. In this chapter we will discuss the synthesis of periodic particles arrays of metal (Au, Ag) nanoparticles for application in plasmonics.

## 2.1 Size dependent properties

NSL enables a fabrication of defect-free nanoparticle arrays with areas of ¿ 100 $\mu m^2$ that are large enough to permit microprobe studies of nanoparticle optical properties. We focus on the fabrication of noble metal nanoparticles by NSL and explore the optical properties, especially, surface plasmons of these nanoparticles. Surface plasmons are collective oscillations of free electrons coupled to the external electromagnetic field that could come in two basic forms, propagating [34] and localized [35]. In a flat smooth film, the surface plasmon polaritons (SPPs) are propagating evanescent electromagnetic waves at the

metal-dielectric interface as a result of collective oscillations of the conduction electrons in the metal. Localized surface plasmon resonances (LSPRs) are observed in isolated nanoparticle systems. These optical modes lead to enhanced electromagnetic fields outside the particle surfaces, which are important in the interaction of the particles with their external environment. NSL has been utilized to fabricate highly uniform arrays of noble metal nanoparticles with LSPR extinction wavelength maxima ($\lambda_{max}$) that can be tuned by changing the size, shape, and environment of the nanoparticle.

Plasmonic nanoparticles are used in a wide range of fields, from labeling [36], cancer therapy [37], sensing [38], spectroscopy [39], fundamental study on the interaction with fluorophores [40]. In all these applications the localized surface plasmon resonance are the key for their application: rise in temperature for cancer, shift of the resonance for sensing, enhancement of signal for spectroscopy, coupling between the fluorophore wavelength of interest (excitation, emission) and the SPR. Having the possibility to tune the LSPR will increase the flexibility in the use of the nanoparticles because it will be possible to use different laser (for cancer therapy, spectroscopy, fluorescence) or it will be possible to couple the LSPR with different fluorophores of technological interest (from visible for labeling to NIR for the rare earth used in telecomunications). This is why having a technique able to produce nanoparticles easily, in a cheap way, in a wide range of size, with an high throughput is of great interest.

Monolayers of PS nanoparticles are formed according to the procedure described in section 1.4. Once the monolayer is formed, the substrate is pulled out to collect the self assembled monolayer: the speed with which one dip and extract the substrate determines the quality of the resulting monolayer: polycrystalline monolayer are always produced, but while high speed give small domains and usually crack between them, low speed could give domains even $750 \times 750$ $\mu m^2$ large. The liquid at the water/alcohol interface exerts capillary forces, which pulls the nanospheres together and compacts them to a densely packed monolayer. These well-ordered monolayers are our starting point for the production of nanostructures, by using them as a template or mask for film deposition. During the deposition the nanospheres mask the substrate, so metal can reaches it only through the holes among the spheres and after the removal of them we obtain a periodic array of triangular islands with $P_{6mm}$ honeycomb symmetry. The interparticle spacing $d$ (Figure 2.1) between two triangular nanoparticles from a mask made of nanoparticles with radius $R$ is given by:

$$d = \frac{2}{3}\sqrt{3}R \tag{2.1}$$

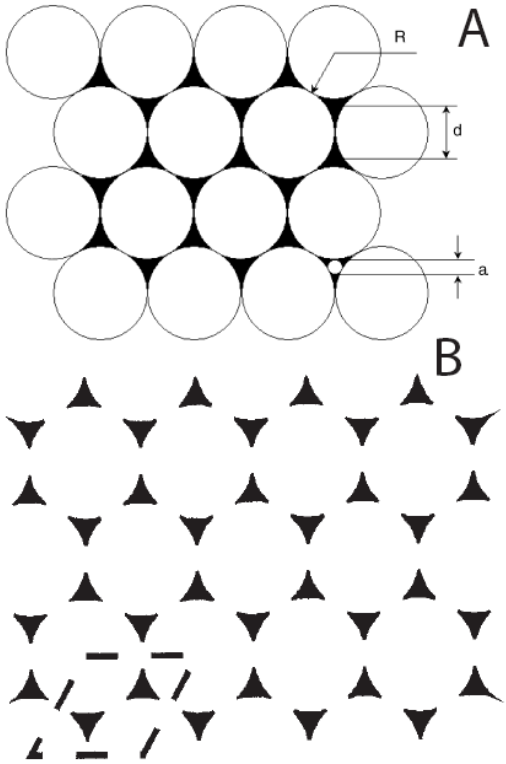


**Figure 2.1:** (A) *Schematic picture of single-layer nanosphere masks with chosen radius R on substrate;* (B) *single-layer periodic particle array (dashed line evidence the $P_{6mm}$ unit cell.*

and the in-plane particle dimension, defined as the perpendicular bisector of the largest inscribed equilateral triangle that fills the threefold hole, is given by

$$a = \frac{3}{2}\left(\sqrt{3} - 1 - \frac{1}{\sqrt{3}}\right) 2R = 0.466R \tag{2.2}$$

The out-of plane height is not governed by the properties of the mask, but should equal to the thickness of the deposited film $d_m$.
Au or Ag were deposited through the nanostructures by DC magnetron sputtering. Argon was used to create the plasma for target erosion, because this gas is inert and doesn't react with the target or the growing nanostructure. The sputter coater system was pumped until a base pressure lower than $3 \cdot 10^{-6}$ $mbar$, to avoid impurities or different gas that will react with the metal during the process. $Ar$ was then let fill the chamber to reach a working pressure of $5 \cdot 10^{-3}$ $mbar$. All the depositions were performed using these parameters. The plasma was lit by application of an high voltage between the target and the sample

holder, adjusting the power to the desired deposition condition.
Sputtering sources are usually large area, and the sputtered atoms are emitted spatially in a cosine-like distribution. For this reason, a large fraction of the sputtered atoms have directions not perpendicular to the sample-surface. To overcome this problem, it's necessary to put the sample near the target. In particular for NSL technique, it must be perpendicular, to allow metal to reach the substrate through the holes of the mask. Our aim was to study and to optimize the control on nanoparticles plasmonic proprieties (e.g. LSPR peak position), tailoring them on the desired application.

## 2.2 Parameters affecting nanoparticles properties

The most important propriety of plasmonic nanoparticles is the strongly amplified local field generated at the sample surface when the conduction electrons and the photons meet the resonance condition. Under this condition there is a collective oscillation of the electron at the metal surface that is coupled with the photon's electric field oscillation and is strongly interacting with it, causing a great absorption and scattering cross section. The absorbed and scattered light from nanoparticle surfaces can be monitored by optical extinction spectroscopy in either transmission or reflection geometry. In the case of the Ag nanoparticles, the relevant wavelength range of these extinction spectroscopy experiments can extend from the near-ultraviolet ($\approx 350nm$) for Ag nanospheres of 10 nm in diameter to the midinfrared ($\approx 10000nm$) for Ag nanotriangles with large aspect ratios. Extinction spectroscopy conveniently correlates nanoparticle structure with the readily measured LSPR observables. The simplest theoretical approach available for modeling the extinction properties of spherical nanoparticles is the Mie theory in the dipole limit [41] (i.e. when nanoparticle size is $<< \lambda$) the following equation

$$E = \frac{24\pi^2 N_A a^3 \epsilon_m^{3/2}}{\lambda ln(10)} \left[ \frac{\epsilon_i}{(\epsilon_r + 2\epsilon_m)^2 + \epsilon_i^2} \right] \tag{2.3}$$

$E$ is the extinction which is, in turn, equal to the sum of absorption and Rayleigh scattering, $N_A$ is the areal density of nanoparticles, $a$ is the radius of the metallic nanosphere, $\epsilon_m$ is the dielectric constant of the medium surrounding the metallic nanosphere (assumed to be non absorbitive), $\lambda$ is the wavelength of the light in vacuum, $\epsilon_i$ is the imaginary part of the metallic nanosphere's dielectric function, and $\epsilon_r$ is the real part of the metallic nanosphere's dielectric function. Even in this dipolar model, it is clear that the experimental extinction spectrum of an isolated metallic nanosphere embedded in an external dielectric medium will depend on nanoparticle radius $a$, nanoparticle material ($\epsilon_i$ and

$\epsilon_r$), and the environment's dielectric function ($\epsilon_m$). Furthermore, when the nanoparticles are not spherical, as is always the case in real samples, the extinction spectrum will depend on the nanoparticle's in-plane diameter, out-of-plane height, shape and relative polarization of light. The dependence of the extinction spectrum on these nanoparticle structural characteristics has also been recognized in the form of simplified model calculations such as those for ellipsoidal nanoparticle geometries. In addition, the samples considered here contain an ensemble of nanoparticles that are supported on a substrate. Thus, the extinction spectrum will also depend on interparticle spacing and substrate dielectric function. Finally, the nanoparticles under study may also possess an intentionally deposited thin dielectric or molecular adsorbate overlayer (2.7.2). Molecular adsorbates may be physisorbed or chemisorbed and, in the case of surface-enhanced Raman spectroscopic experiments, are the target of study (as we will see in section 2.7.1). Consequently, the extinction spectrum will depend on a variety of parameters such as dielectric overlayer thickness and dielectric constant and molecular adsorbate dielectric constant, thickness, and coverage which will be referred to, collectively, as the nanoenvironment. NSL is the enabling tool that now makes it possible to independently investigate the dependence of the LSPR on nanostructure and nano environment. Size and shape of the metallic NPs are known to be major parameters in determining the position of the LSPR extinction peak, so our aim was at gaining control on the process, in order to tailor the LSPR of the nanoparticles according to the desired application. We studied also the influence of synthesis parameters and of possible modification of the sample that could change the morphology of the resulting triangular nanoparticles. It is important to understand how all these parameters can modify the proprieties and performances of the nanoparticles for possible applications. In this chapter, we will study the following parameters:

- PS nanoparticles size
- Synthesis parameter
- Metal deposited
- Modification of the mask
- Modification of the metallic nanoparticles shape

## 2.3 Metallic nanostructures made by NSL

Metallic nanoparticles are easy to synthesize using NSL. A self assembled monolayer of monodisperse polystyrene nanospheres has to be deposited on a substrate, then metal has to be deposited through the self assembled mask, finally the mask needs to be removed. The self assembled monolayer of polystyrene nanoparticles was deposited on various substrates (sodalime glass, silica slides, silicon wafer) with the method described in section 1.4. Metal (Ag, Au) was deposited via magnetron sputtering. PS nanospheres were removed either by scotch tape peeling or by dissolving polymer nanoparticles in an organic solvent (toluene, hexane, THF) with the aid of ultrasonic bath. Scotch tape does not remove completely the nanoparticles but surface free area $> 500\mu m^2$ could be easy fabricated by this procedure. Liftoff done by solvent dissolution and sonication work better in our case. In table 2.1 are summarized the parameters for the synthesis of the metallic nanoparticles. All the nanoparticles presented here are synthesized using that parameters, except when reported elsewhere.

| PS size (nm) | Metal | Sputtering power | Sputtering time | NP thickness |
|---|---|---|---|---|
| 722 | Ag | 10 W | 800 s | 25 ± 5 nm |
| 330 | Ag | 10 W | 800 s | 13 ± 3 nm |
| 722 | Au | 20 W | 240 s | 24 ± 5 nm |
| 330 | Ag | 20 W | 240 s | 12 ± 3 nm |

**Table 2.1:** *Parameters used for the synthesis of the metallic nanoparticles presented in this thesis work. NP thickness is measured via AFM.*

### 2.3.1 Size of the PS nanospheres

The first parameter analyzed is the size of PS NS used to create the monolayer that serves as mask for metal deposition and so the dimension of the metal nanoparticles (NP). As described in equation 2.2 the bigger the PS NS the bigger the metal NP. The PS nanoparticles size used to study the size effect are listed in table 2.2. Figure 2.2 shows a comparison between silver nanostructures obtained from PS NS of 330 $nm$ and 722 $nm$. Our nanoparticles are slightly different from the nanoparticles previously observed in literature, normally produced by thermal evaporation instead of sputtering. The particles have bigger in plane dimension and grow with a pyramidal like structure instead of a triangular prism. The expected coverage from a geometrical projection of the holes in the masks could be calculated using the unit cell shown in Figure 2.1: $\Sigma_{cell} = 2\sqrt{3}R^2$. It contains one sphere with an area of $\pi R^2$ and two triangular nanoparticles. The percentage of area occupied by the nanosphere respect to the total area is:

| NP mean diameter | Standard Deviation |
|---|---|
| 920 | 2.5 % |
| 722 | 3.1 % |
| 535 | 3.0 % |
| 330 | 2.7 % |
| 234 | 3.4 % |
| 153 | 4.5 % |

**Table 2.2:** *PS nanoparticles size and size dispersion used in the present work. Mean diameter measured by Differential Centrifugal Sedimentation.*

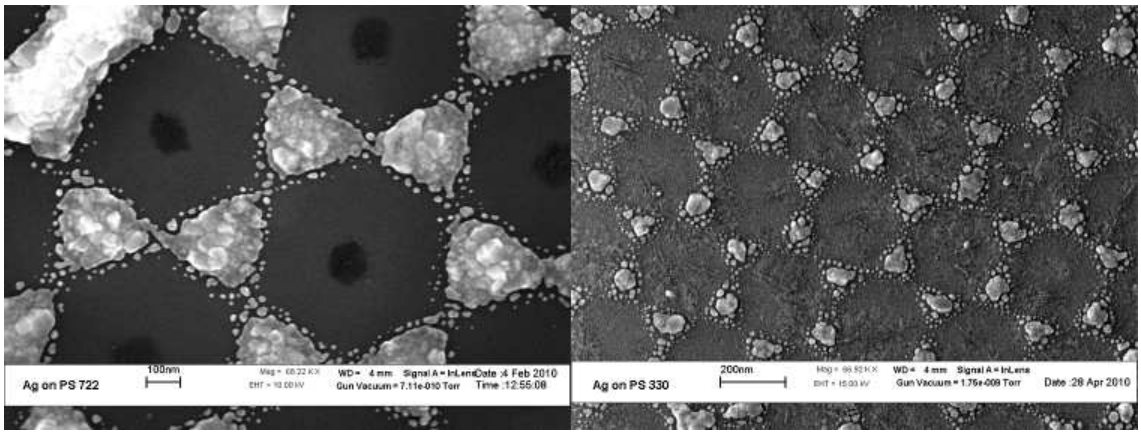


**Figure 2.2:** *Silver Nanoparticles made by NSL using two different mask made with two different PS NP dimension.* Left: *Ag NP made using 722 nm PS mask;* Right: *Ag NP made using 330 nm PS mask.*

$$\eta_{spere} = \frac{\Sigma_{sphere}}{\Sigma_{cell}} = \frac{\pi R^2}{2\sqrt{3}R^2} = 90.6\% \;\Rightarrow\; \eta_{NP} = 9.4\% \tag{2.4}$$

Experimentally we find values of about $\eta_{NP} = 25\%$ which is bigger than the nominal one. The difference respect to the nominal value means that the sputtering process deposits metal even under the shadowed region. This could be caused by the sputtering process itself, as a large fraction of the sputtered atoms have directions not perpendicular to the sample-surface. If we look at the mask just after the deposition, before the peeling (Figure 2.3) we can see that the holes are smaller that the ones at the beginning of the deposition, this also support the hypotesis of divergent flux of materials that slips under the mask to create larger particles in the in-plane dimension and deposit also on the PS nanosphere side, gradually closing the pores as the deposition goes on. This can also explain the pyramidal shape of the particles: as the deposition proceeds the pores become smaller and so their geometrical projection. Diffusion phenomena can also be a

cause for enlargement of the triangles on the plane and for the fact that we don't have a perfect triangle, but a structure that grows pyramidal-like with a lot of satellites all around. To test this hypothesis we functionalized the surface of two silicon wafers with two different silanes, in order to make the substrate more "sticky" for the incoming metal ions: an amino-terminated silane (3-Aminopropyl triethoxysilane APTES) and a thiol-terminated silane (3-mercaptopropyl trimethoxysilane MPTMS) were used to functionalize a silicon substrate. Silicon wafer were rinsed with a 3:1 mixture of $NH_4OH$ and $H_2O_2$ to break the $Si-O-Si$ bonds on the surface producing several $Si-OH$ function. To functionalize the silicon surface, we prepared a 1% solution of the silane in toluene (*puriss*) and put the silicon pieces in the warm ($70°C$) solution for 3 $min$. With this procedure a very thin layer ($<$ 1 $nm$) of the silane is formed on the silicon surface. It is possible to confirm the deposition of the silane layer by a contact angle measurement. With respect to the hydrolized surface (which is very hydrophilic), the thiol terminated and the amino terminated surface are slighlty hydrophobic. Toluene was choosed as solvent because it is hydrophobic and it is not miscible with water. Silane can condense in the homogeneus phase in presence of water, the use of an hydrophobic solvent without any trace of water implies that in our experimental conditions only the reaction between the silicon surface and the silane is possible, the condensation produce ethanol (for APTES) or methanol (for MPTMS) which are soluble in the toluene phase. In Figure 2.4 SEM images of silver nanoparticles deposited on bare silicon, an $-NH_2$ terminated silicon and an $-SH$ terminated silicon are shown. It is possible to see that the different surface on which sputtering is being done does not change significantly the microstructure of the nanoparticles. So the major effect driving the growth of the nanotriangle during the sputtering process could be the non perpendicular trajectories of the incoming metal ions.

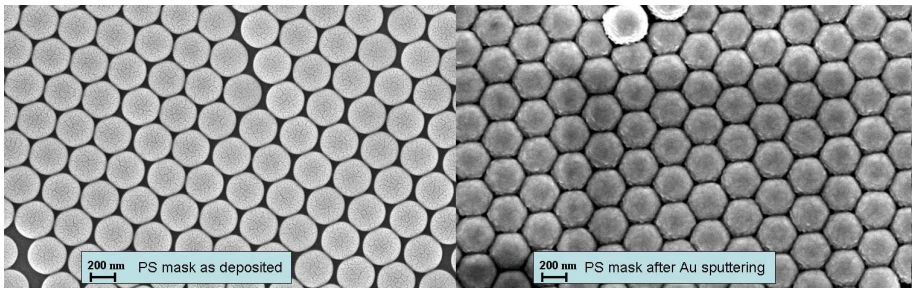


**Figure 2.3:** *PS mask after the deposition of silver and prior to the liftoff.*

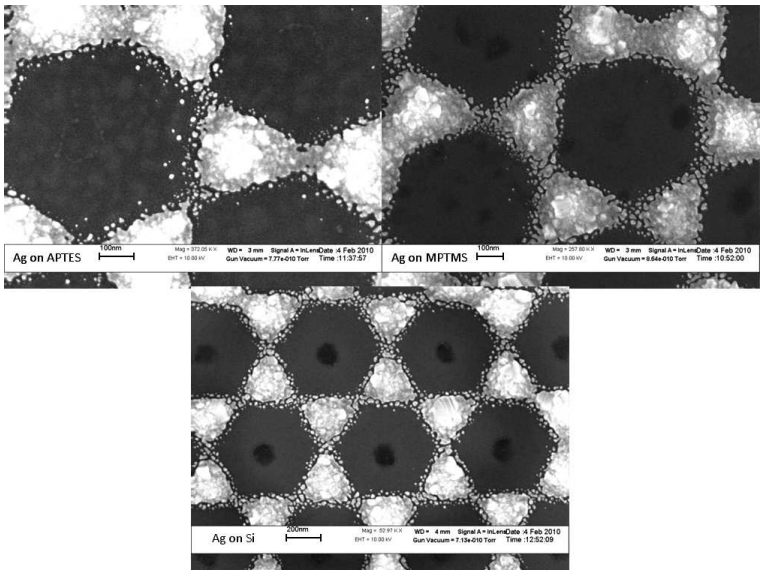


**Figure 2.4:** *Silver nanostructures deposited through a 722nm PS mask on APTES primed silicon* (Top Left)*; MPTMS primed silicon* (Top Right)*; bare silicon surface* (Bottom)

## 2.4 Effect of sputtering power

We have realized Ag NPs arrays working at different sputtering powers P=2, 5, 10, 20, 30, 60, 80 W, scaling the sputtering time (t), so that the product $P \cdot t$ remains constant, to obtain samples with the same nominal thickness. The aim of this experiment is to see if changing the sputtering power modifies the microstructures of the nanotriangles. We measure by AFM the thickness for both the metal nanostructure and a substrate without the mask used as reference. For the different powers we obtained an average values of $15 \pm 3$ $nm$ for the height of Ag NPs and $140 \pm 15$ $nm$ for the reference film. Figure 2.5 shows silver nanostructures obtained from PS NSs of 330 $nm$ at three different powers: 10, 60, 80 W. Figure 2.6 shows silver nanostructures obtained from PS NSs of 722 $nm$ at three different powers: 2, 10, 60, W. The two major differences in the nanoparticles morphology is the reduction of the number of satellite clusters that decorate the triangle boundaries and the increase in size of the triangle dimensions, when increasing the sputtering power. For high power synthesis nanoparticles almost touch or merge with their neighbours. This reflects in the variation of the optical spectra as is shown in Figure 2.7.

The optical spectra presented are relative to the Ag nanoparticles produced with a 330 $nm$ PS mask. For all the samples the extinction peak are composed of a peak in the 600 - 700 nm region with a side shoulder at lower wavelength. The shoulder in the spectra appears only in the sample synthesized with a low sputtering power, and we can suppose

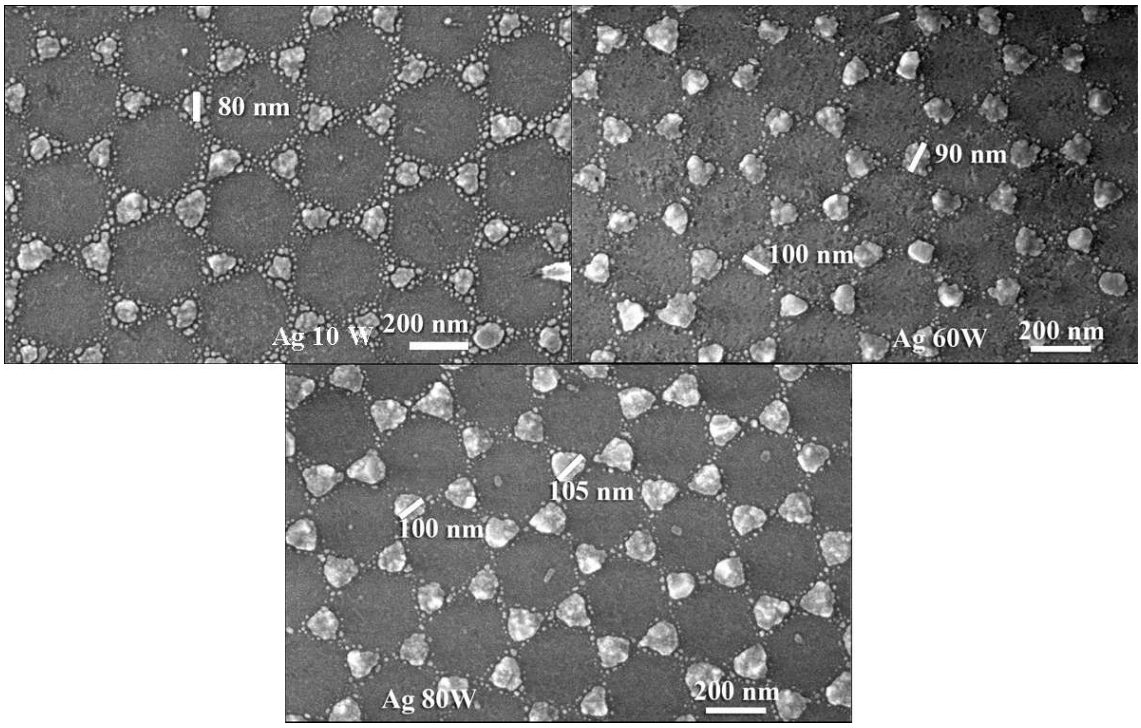


**Figure 2.5:** *SEM images of silver nanostructures obtained from PS NSs of* 330 *nm at three different powers: a)* 10 *W; b)* 60 *W; c)* 80 *W*

that it may be caused by the small satellite clusters, whose influence becomes smaller as the sputtering power increases. A complete understanding of the optical behavior of these sample is not easy at all. The nanoparticles are non spherical, in a asymmetric environment and are strongly interacting with the small clusters. Numerical solution of the Maxwell equation using method such as Discrete Dipole Approximation (DDA) or Finite Elements Methods (FEM) and in particular Finite Difference Frequency Domain (FDFD) should provide enough information to better understand the physic of our system. In section 2.5 we will show some preliminary data.
Another important feature of the nanotriangle's morphology is the roughness of the particle. SEM images suggest that high power synthesis produce smoother nanoparticles. AFM measurement on the single triangle are difficult and would provide uncertain results, so we characterize the surface roughness of the reference film, as shown in Figure 2.8 for different deposition powers.

As the SEM images were suggesting we can see a trend in the roughness even from the AFM images. The analysis of the AFM images support this hypothesis: monotonic decreasing trend versus the sputtering power is found as shown in Figure 2.9. It is possible that increasing power, also the temperature of the substrate increases, because of the

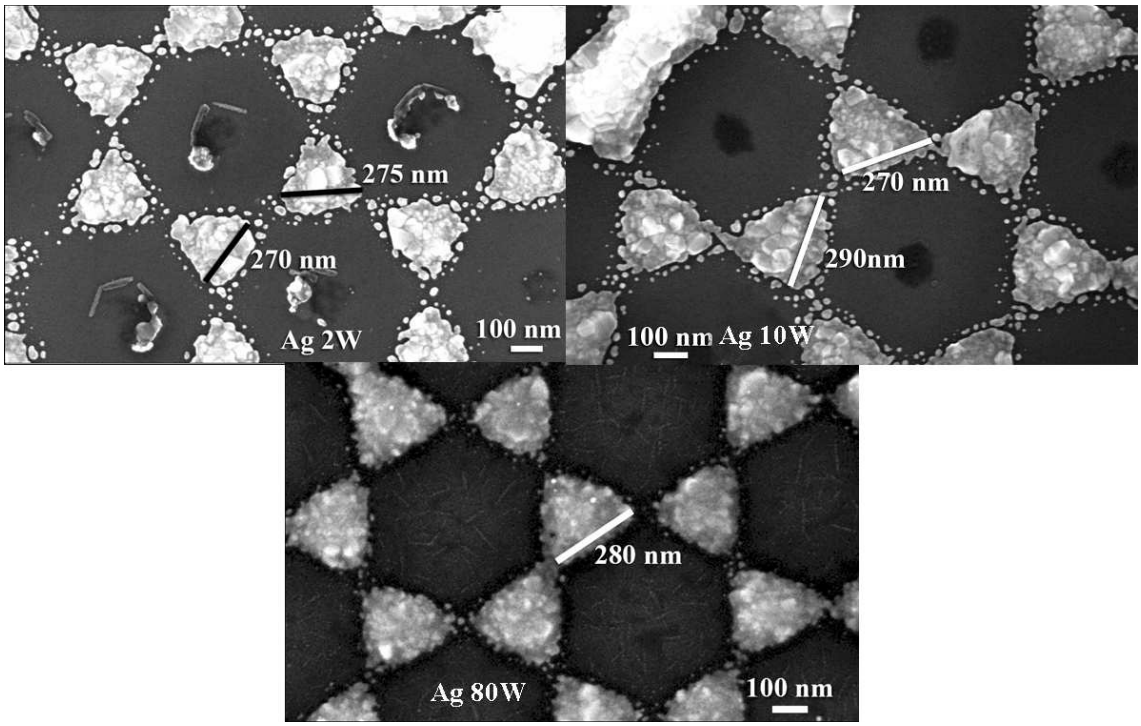


**Figure 2.6:** *SEM images of silver nanostructures obtained from PS NSs of* 722 *nm at three different powers: a)* 2 *W ; b)* 10 *W ; c)* 60 *W*

current that flows in the system. An increased temperature can promote the diffusion of the metal atoms on the surface creating a more uniform structure with a reduced roughness.

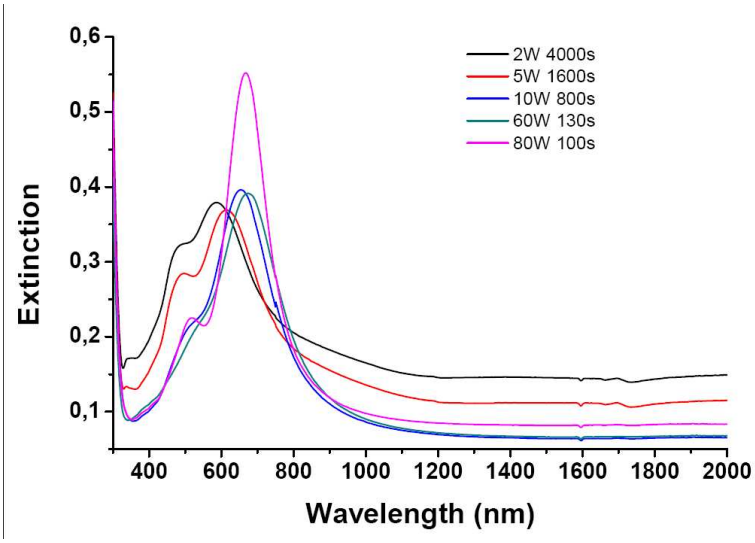


**Figure 2.7:** *Optical spectra of silver nanostructures made using a 330 nm PS mask and different sputtering power*

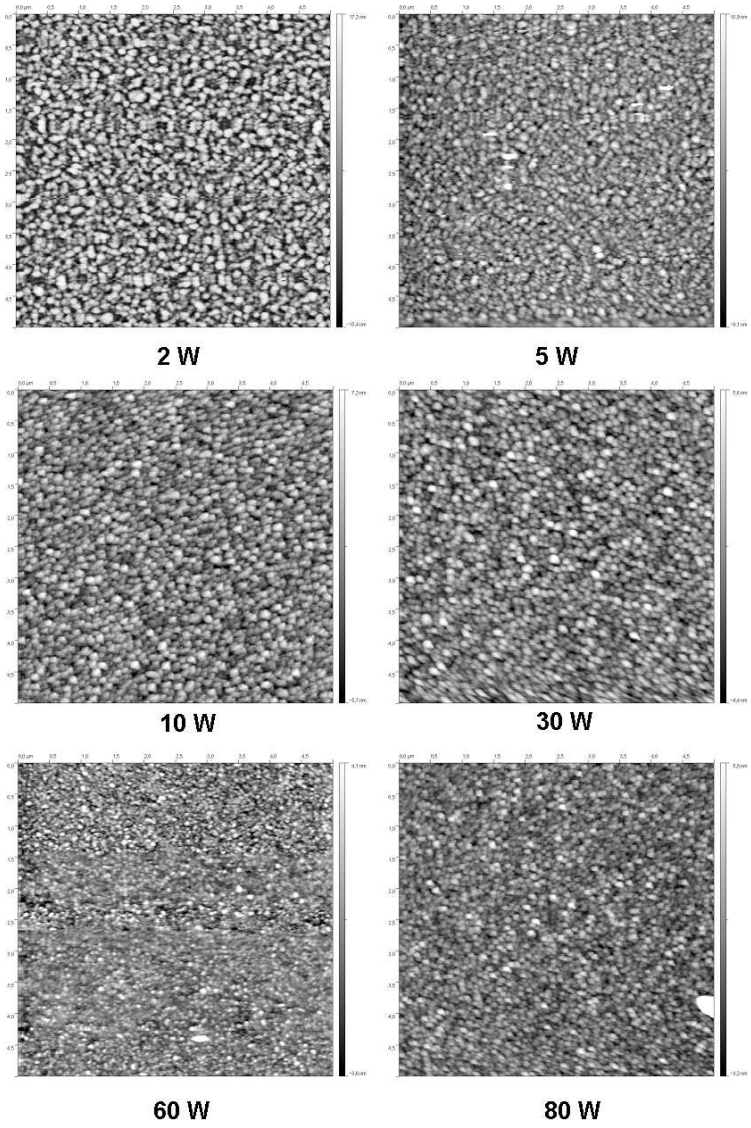


**Figure 2.8:** *AFM images of the Ag sample surface roughness at different deposition power. Images are* $5 \times 5$ $\mu m^2$ *large.*

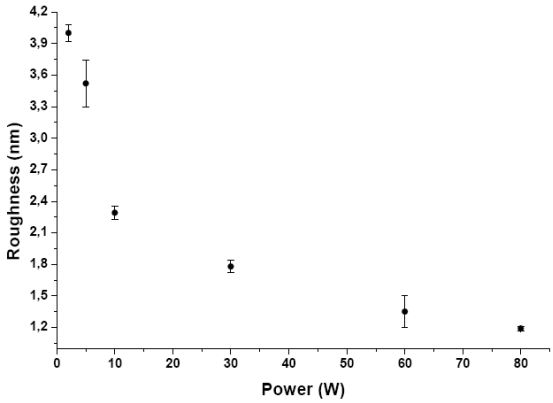


**Figure 2.9:** *Determination of the roughness of Ag reference samples as function of the sputtering power.*

## 2.5 Optical properties

Optical proprieties were characterized with a UV-Visible-NIR JASCO 670 spectrophotometer. We first checked the reproducibility on the LSPR peak position of the nanostructures. Since nanoparticles produced with mask made of bigger PS nanoparticles have a very complex optical extinction spectra with lots of resonances, extensive study were made for 330 $nm$ PS self assembled monolayers. For silver nanoparticles we found that there is an effect on the LSPR $\lambda_{max}$ position caused by a misalignment between the sputtering target and the sample. Once optimized the synthesis the peak is located always in the same position with a very low variation. For silver the $\lambda_{max}$ is located at $670 \pm 20$ $nm$ and for gold $\lambda_{max} = 925 \pm 30$ $nm$. This means a variation of $\approx 3\%$ on the position which has the same value of the variation of the PS nanospheres's size. Noble metallic nanoparticles are known to have both a great absorption caused by the surface plasmon resonance and also a great scattering coefficient. When performing a standard extinction measurement, the obtained extinction spectra reflect total losses due to both absorption and scattering. To separate the two contribution we measured the scattered light with an integrating sphere detector. Extinction coefficient is related to the Lambert Beer Law (eq. 2.5):

$$I(\lambda) = I_0 e^{-[\alpha_{ext}(\lambda) \cdot l]} \tag{2.5}$$

where $I_0$ is the incident light intensity, $I(\lambda)$ is the measured intesity after the sample, $\alpha_{ext}(\lambda)$ is the extinction coefficient and $l$ is the sample thickness. The scattering coefficient $\alpha_{scatt}(\lambda)$ is defined as:

$$\alpha_{scatt}(\lambda) = \frac{I_{Scatt}}{I_0} \tag{2.6}$$

where $I_{Scatt}$ is the measured scattered light integrated over the entire solid angle (measured with and integrating sphere detector) and $I_0$ is the incident light. The absorption coefficient can be easily calculated subtracting the scattering coefficient from the extinction:

$$\alpha_{ext}(\lambda) = \alpha_{abs}(\lambda) + \alpha_{scatt}(\lambda) \Rightarrow \alpha_{abs}(\lambda) = \alpha_{ext}(\lambda) - \alpha_{scatt}(\lambda) \tag{2.7}$$

The absolute value of the coefficient is function of the numerical density N of particles in the sample: $\alpha = \sigma \cdot N$ and $\sigma$ is the extinction cross section. To obtain a more general parameter, we have to normalize by the surface density of particles, that can be estimated from a SEM image. In Figure 2.10 we plotted the measured cross section for

silver and gold nanostructures. It is evident how both phenomena give an important contribution to the extinction. Absorption is dominant in the $400nm - 600nm$ region for silver nanostructures, where there is the quadrupolar resonance, while the scattering is the major contribution for wavelengths greater than $600nm$, where there is the dipolar resonance. Gold nanostructures have a more complicated optical spectra, but also in this case the absorption contribution is more relevant for lower wavelengths and the scattering contribution for higher wavelengths.

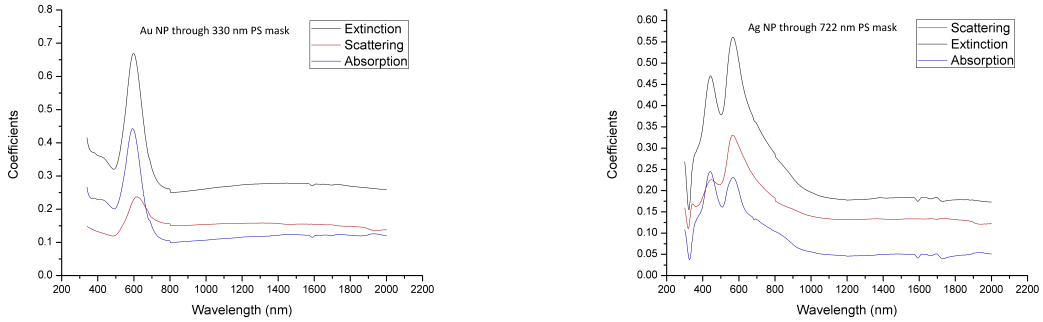


**Figure 2.10:** Left*: deconvolution of the extinction peak for gold nanoparticles synthesized using a 330 nm PS mask.* Right*: deconvolution of the extinction peak for silver nanoparticles synthesized using a 722 nm PS mask*

To achieve a better comprehension on the optical proprieties of nanotriangles in our group we modeled the NP optical proprieties using a DDA approach. The discrete dipole approximation (DDA) is a numerical method to solve the scattering from nanoparticles with arbitrary shapes. Lorentz, in 1909, found a relation between the polarizabilities of the individual atoms composing a material and its dielectric properties [42]. The DDA takes an object and approximates it by a 3D grid of interacting dipoles and then solves the scattering problem in a self-consistent way; with each dipole feeling the external field plus the sum of the scattered field from all of the other dipoles in the target. The calculations are speeded by the use of Fast Fourier Transform (FFT) methods, which requires the use of a periodic lattice. The first step towards simulating the triangles made in laboratory is to model the nanoparticles the following called the "targets". As is possible to see from the SEM analysis, the nanotriangles synthesized are not perfect prisms, and so the targets simulated have been created with rounded edges, defined by a parameter R, the roundness, with the sides sloping up to a collective point or plane. Using the diagram in Figure 2.11, we can express the parameter R as $d1 = a(1 - R)$, where, $a = \frac{\sqrt{3}}{3}L$. If $R$ is equal 0 the triangle would remain an equilateral triangle of side length $L$, if it were equal

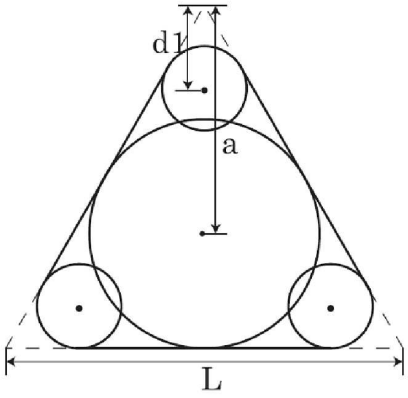


**Figure 2.11:** *The base of the equilateral triangular tetrahedra targets upon which layers of slightly smaller dimension get stacked upon until the top is reached*

to 1, the initial equilateral triangle would be reduced to the central circle, in the middle of Figure 2.11. To build a truncated tetrahedron an upper layer is added with a slightly smaller $L$, until the height wanted is reached - hence it usually does not finish in a point, as the samples made in laboratory are generally quite flat. The calculations were carried out with DDSCAT for silver tetrahedra and prism, with $R = 0.0, 0.3, 0.6$. The dimensions of the nanoparticles were $L = 100\ nm$ and $L = 150\ nm$ and the height was 20 $nm$, leaving a flattened top for the trucated tetrahedra.

Our target model is still much simpler with respect to the experimental sample: the model consist in a single triangular based prism or a tetrahedron in a uniform environment (vacuum or an effective medium which has an effective refraction index $n_{eff} = \frac{n_{vacuum}+n_{glass}}{2} \approx 1.3$). On the contrary the real sample is in a non symmetrical environment (glass at the bottom, air at the top) and is interacting with the nearest nanotriangles and also with the small nanoparticles decorating the border. We do not expect that such a simple model will describe quantitatively the measured optical proprieties, but it should give a first guess on the behaviour of the sample and provide some indication on the trends when changing parameters. In Figure 2.12 DDA data are presented for two silver nanoparticles of 100 nm and 150 nm large in vacuum, which correspond to triangles deposited using 330 nm and 535 nm PS self assembled monolayer. Two different shapes have been studied: a prism like and a tetrahedron like nanoparticles. The first shape is the expected shape when metals arrives on the substrate perfectly perpendicular, so the growth of the particles follows in every moment the projection of the mask; the latter shape is in agreement with SEM and AFM measurement. From the calculation it appears that the tetrahedral structures better match the experimental data, having the LSPR extinction peak position in good

agreement with measured samples. This could means that even such a simplified model could give some useful information on the nanoparticles. On the other hand the prism like nanoparticles has the peak blue shifted compared to the experimental data, while it has the ratio between scattering and absorption cross section which is similar to the experimental measurement on the samples. The estimation of the absorption to scattering ratio could be influenced by the shape of the triangle's model: these first calculations have been done using a thinner tetrahedron which should have a more absorbing rather than scattering behaviour, moreover in the experimental sample the defect in the mask such as vacation of spheres or dislocations, produce continuous ribbons of metal which have a huge scattering cross section, so the experimental measure could have overestimated the scattering contribution.

We expect that the introduction of the asymmetrical environment will cause a little red shift of the LSPR peak because the electromagnetic field will reach an intermediate configuration between the nanoparticle in vacuum and the particle into the glass, while the interaction between the nanoparticle and its neighborhood (other tetrahedral particles and the small spheric nanoparticles) will cause a red shift and possibly a modification in the peak features [43].

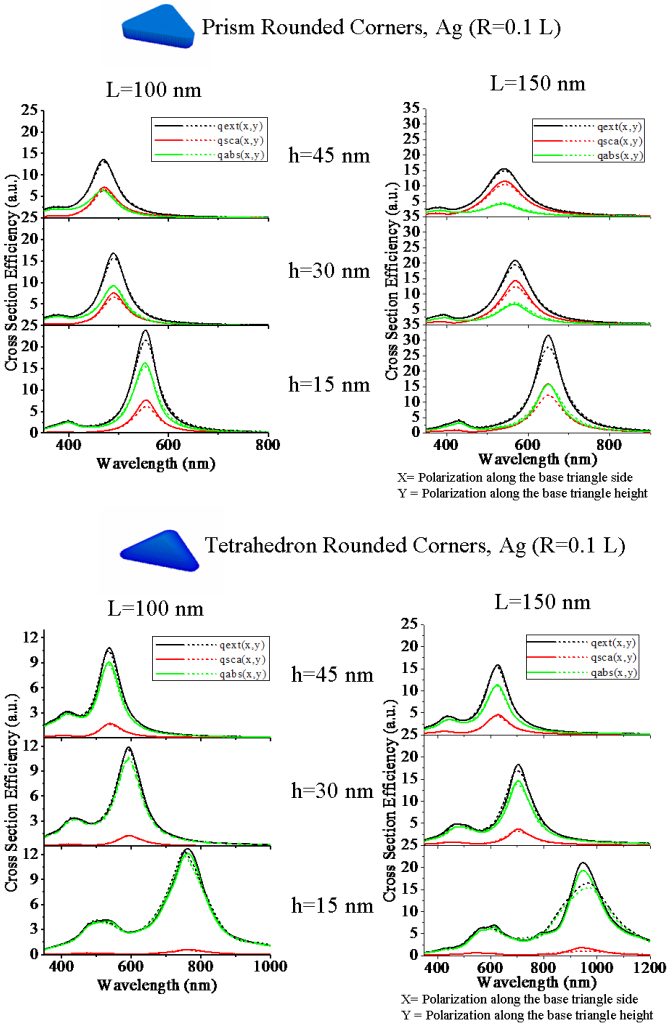


**Figure 2.12:** *DDA calculation for the scattering efficiency of silver nanoparticles in vacuum. Two differet size and shape of nanostructures were simulated: a prism like structure (*Left*) and a tetrahedron like structure (*Right*).*

## 2.6 LSPR peak tuning

Optical proprieties of the metallic nanoparticles are the fingerprint of the nanostructure's behaviour, because the most interesting applications rely on the local field enhancement caused by the LSPR ([44, 45, 46]) or the dependency of the position of the LSPR peak (LSPR nanosensors). The modeling of the optical proprieties is the key to the comprehension of the phenomenon. From the nanofabrication point of view, achieving a good control on the synthesis of NP with a tunable and well defined LSPR is of paramount importance for applications.

For NSL the main parameter determining the position of LSPR extinction peak is the size of PS nanospheres used to create the mask. Using the PS nanospheres with size from $920nm$ to $153nm$, with equation 2.2 we expect to obtain metallic nanoparticles with in plane size from $215nm$ to $36nm$. As an example, two SEM images of silver nanotriangle deposited using two different PS nanoparticles size are presented in figure 2.13. The op-

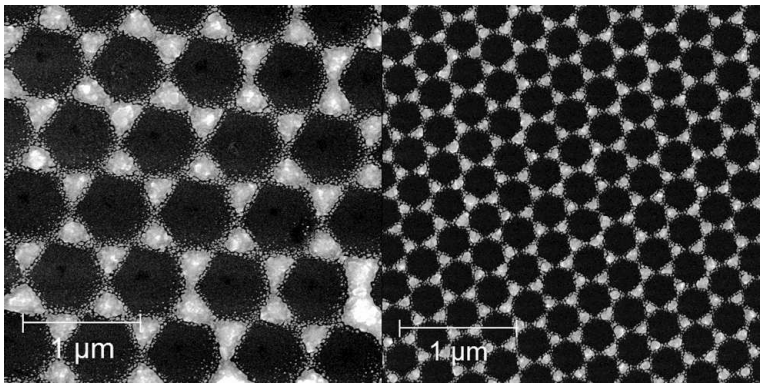


**Figure 2.13:** *SEM image nano triangles synthesized via sputtering of Ag on a 720 nm PS self assembled mask* (Left) *and on a 330 nm PS self assembled mask* (Right).

tical extinction spectra change a lot by changing the NP dimension from a single peak at 460 $nm$ for nanotriangles made with 153 nm PS mask to a more complex spectrum with more resonances for bigger nanoparticles. In Figure 2.14 and Figure 2.18 spectra for nanoparticles deposited using masks made with different size of PS nanospheres are shown. Metal also is another major factor in the determination of the position of the LSRP peak: nanostructures deposited through the same mask have the LSPR peak position at different wavelength. Normally silver nanoparticles have the extinction spectra blue-shifted with respect to the gold ones: Figure 2.15 give an example for nanostructures made by sputtering gold or silver using a 330 nm PS mask. The resulting LSPR are $\lambda_{max,Au} = 920\ nm$ and $\lambda_{max,Ag} = 690\ nm$ for gold and silver respectively. There is a $\approx 200\ nm$ of difference between the two arrays of nanoparticles. When looking at the other samples, LSPR peaks

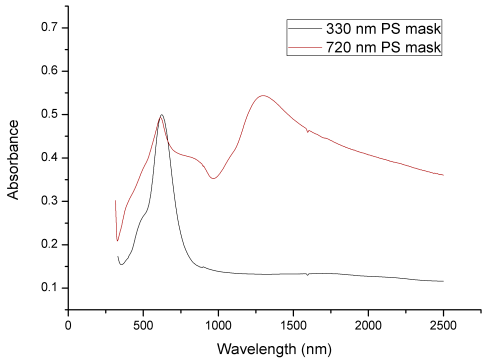


**Figure 2.14:** *Silver nanostructures made self assembling two different size of PS nanoparticles: 722 nm and 330 nm*

are in the 460 to 1600 nm for silver nanostructures and from 550 to 1800 nm for gold ones. There is a region of overlap where it is possible to obtain a LSPR peak both with silver and gold nanostructures, using gold with smaller PS nanospheres and silver with bigger.

Plasmon resonance greatly changes changing the size of the PS nanoparticles or the metal deposited and this propriety is used to fabricate structures with prescribed position of the surface plasmon resonance absorption peak. We explored two additional strategies to finely tune the peak position: (1) through the modification of the PS mask before sputtering metal and (2) reshaping the metallic nanostructures after deposition. PS nanospheres have a glass transition temperature ($T_g$) at about $80 - 90°C$ (as given by the manufacturer), which means that if heated in this temperature range the self assembled

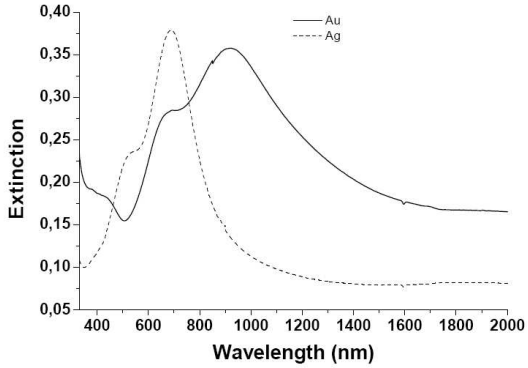


**Figure 2.15:** *Optical extinction spectra for gold and silver nanostructures synthesized by sputtering through a 330 nm PS mask.*

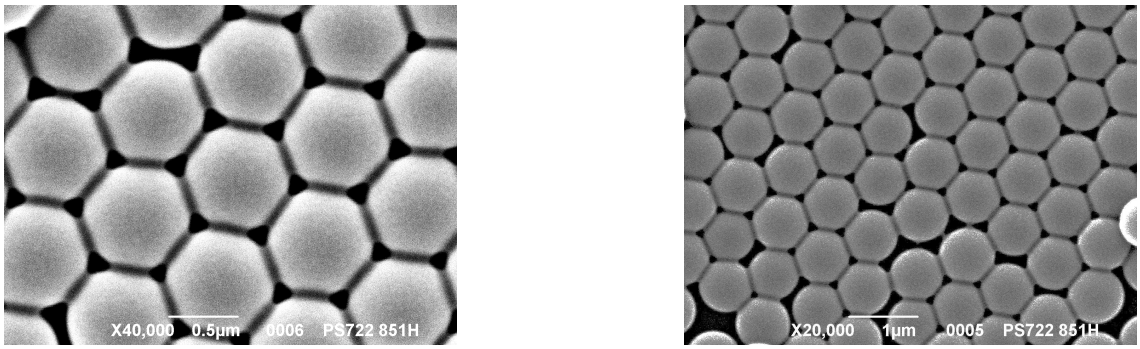


**Figure 2.16:** *Self assembled mask made of 720 nm PS nanoparticles and annealed in air at 85° C for one hour. Necks are formed between the particles and so the pore size is reduced.*

mask will soften or slightly melt, leading to the formation of necks between the particles and reducing the size of the pores (Figure 2.16). Nanoparticles produced with this kind of mask will be smaller and more separated, so the plasmon peak will blue-shift with respect to the particles produced with the standard mask.
Giersig proposed [25] a thermal modification of the PS mask in a liquid environment. The monolayer of latex nanospheres immersed in a mixture (25 mL) of water/ethanol/acetone (3:1:1) is heated by microwave heating up to the boiling temperature of the mixture, then additional microwave pulses are applied with a duration of 3 s and period of 28 s. With the 540-nm PS latex monolayer they could adjust the aperture size from an initial 200 nm to 25 nm. The annealed masks have different thicknesses the more the sample is annealed i.e. they became flatter and thinner. This effect appears as a color change of the mask. Annealing shifts the color of the 540-nm nanosphere monolayer from red to blue; however the color change is very rapid as the mask reaches the melting temperature which makes precise control more difficult. The annealing process performed on a heating plate can also be inhomogeneous as a result of a temperature gradient on the sample (imperfect contact between heating plate and substrate).

We found that placing the monolayer into a oven on a small support made in refractive material can give excellent results too. Oven can have a precise control on the temperature and a good stability which let us change the size of the pores with a good control on the resulting dimension.
Figure **??** shows the change in the optical proprieties for nanostructures produced from a pristine 330 nm PS mask and a sample produced via the same mask which was annealed in air in a oven for 60 $min$ a $85°C$. LSPR peak blue-shifts because of the reduced size of the pores, and the extinction peak is a little lower (0.25 instead of 0.35 absorbance unit at $\lambda_{max}$) because smaller triangles have less volume and so a lower absorption. Another

way to modify the plasmon resonance of the metallic nanoparticles is an annealing of the metallic particles after the deposition. The nanoparticles would change their shape, the satellite clusters disappear merging themselves into the thermodynamically more stable big particles. The resonance peak shifts towards lower wavelength, and for bigger particles (made with 720 nm or 920 nm PS nanoparticles) the absorption peak changes significantly (Figure **??**).

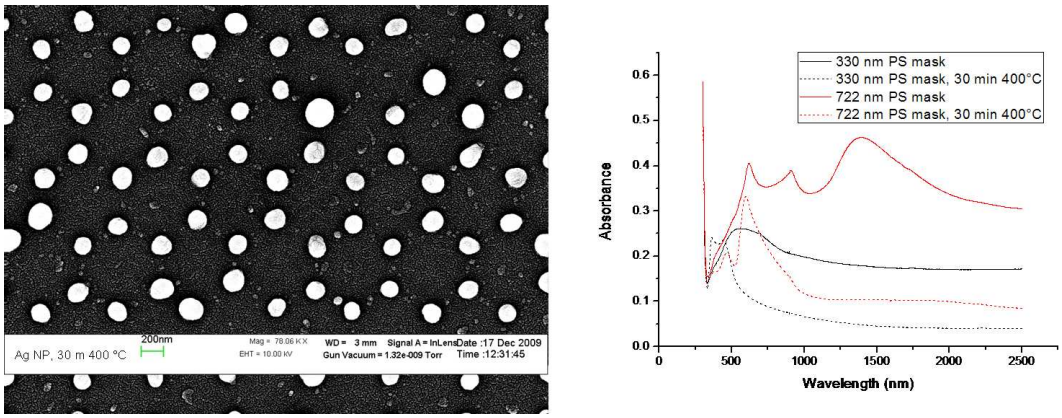


**Figure 2.17:** *SEM image of the annealed silver nanostructure made through a 720 nm PS mask: the silver nanoparticles change their shape from triangular to circular, consequently the plasmon peak blue shift*

With NSL it is possible to synthesize plasmonic nanostructures with a good control on NP plasmonic proprieties. In addition, there are a couple of easy method to change the synthesis condition (modification of the mask) or the resulting particles making us able to finely tune the LSRP peak position on a wide range of wavelength from visible to infrared. This high throughput, parallel and cheap method of nanofabrication appear to be also flexible an so a good candidate to the production of nanostructured materials.

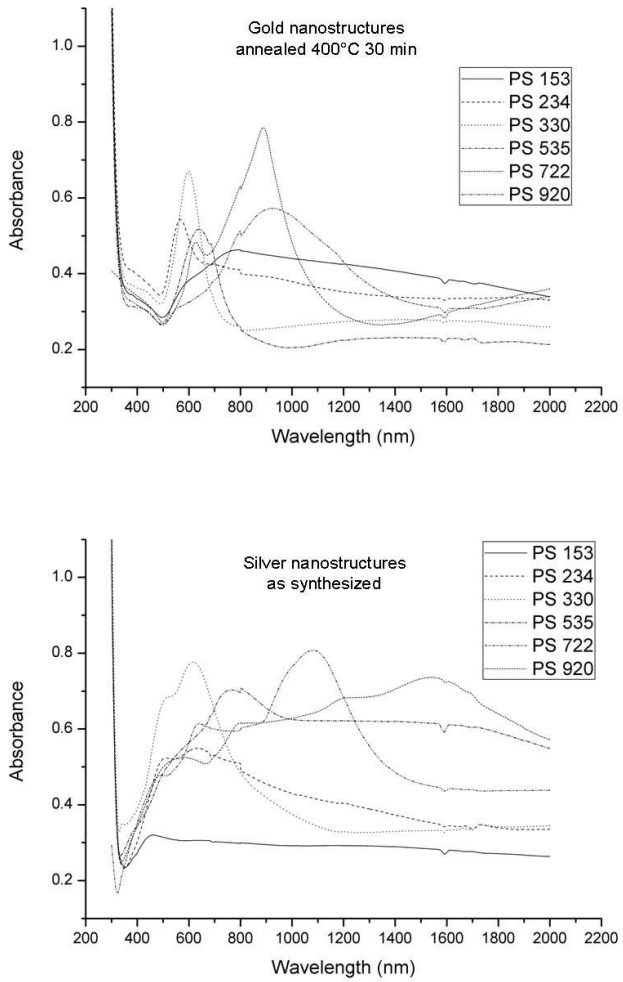


**Figure 2.18:** *Optical properties of metallic nanostructure made sputtering silver with masks made with different PS NP size, and of gold nanostructures made by sputtering on different PS NP size and after a thermal annealing in air at 400° C for 30 min.*

## 2.7 Application

In this section we will discuss some applications of the gold and silver arrays of nanoparticles.

### 2.7.1 SERS measurements

Silver nanostructures were functionalized with Benzenthiol (BT), in order to test the Surface Enhanced Raman Spectroscopy (SERS) response of the nano-objects, referring to the work of Haynes and Van Duyne [44]. SERS measurements were performed in the Department of Chemistry at University of Padova. BT has been selected since the thiol produces good chemical bounding to the metal and has a high SERS cross section. We dipped each sample in a solution of $25\mu L$ of BT, which is a great excess, in $25\,mL$ of methanol for about $20\,h$. Then we rinsed samples repeatedly in methanol. SERS measurements are performed with a Ranishaw micro-Raman instrument, employing a $50\times$ microscope objective (NA $= 0.75$). Samples are excited with $633\,nm$ wavelength line of a He-Ne gas laser. In our derivation we have considered that the SERS signal originates only from molecules directly adsorbed on the metal surface. It is important that the surface coverage remains equal (or lower) to one monolayer, in order to use the subsequent equation. This is because the SERS effect is distance-dependent and the SERS signal from molecules on the second monolayer is usually reduced and it is not included in the used equation To evaluate the Enhancement Factor (EF) we employed the SERS substrate enhancement factors (SSEFs):

$$SSEFs = \frac{I^{Raman,\,monolayer}}{I^{Raman,\,liquid}} \frac{C_V H_{eff}}{C_S} \frac{\sigma_{toluene}}{\sigma_{BT}} \tag{2.8}$$

where $\sigma_{toluene}$ is the toluene differential cross section ($3.53 \cdot 10^{-30}\,cm^2\ sr^{-1}\ molecules^{-1}$) , $\sigma_{BT}$ is the BT differential cross section ($4.9 \cdot 10^{-30}\,cm^2\ sr^{-1}\ molecules^{-1}$), $C_V$ is the toluene volumetric density ($5.69 \cdot 10^{21}\,molecules/cm^3$), $C_S$ is the BT packing density on the surface ($6.8 \cdot 10^{14}\,molecules/cm^2$) and $H_{eff}$ is the collection efficiency dependent on the collection apparatus and on the effective scattering volume of the sample. $H_{eff}$ resulted $= 12.22\,\mu m$, using as probe Ag NPs obtained from PS NSs of $330\,nm$.

The mechanism proposed by Van Duyne for the SERS effect relies on the local field enhancement of the light used to probe the Raman effect mediated by the LSPR. On their work, [44], Haynes and Van Duyne define an experimental window in which the $\lambda_{LSPR,max}$ have to be located for being able to see a surface enhancement effect. LSPR $\lambda_{max}$ have to

fall within a $\approx 120\ nm$ window that encompasses both the excitation wavelength and the scattered wavelength. Best value of enhancement factors are obtained when $\lambda_{LSPR,max}$ lies between $\lambda_{excitation}$ and $\lambda_{scattering}$. For our measurements $\lambda_{excitation} = 633\ nm$, we are interested in the aromatic ring breath mode, which has a frequency shift of 998 $cm^{-1}$, so that $\lambda_{scattering} = 675.69\ nm$.

Two samples were measured:

1. Ag NPs as deposited (from PS NSs of $330\,nm$)
2. Ag NPs as deposited (from PS NSs of $722\,nm$)

The sample made using 330 nm PS beads, has a LSPR (measured after the functionalization with BT) at the borderline of the "120 nm window" suggested by Van Duyne, because the $\lambda_{LSPR,max} = 740\ nm$. The sample made using 722 nm PS nanospheres has a feature at $\lambda_{LSPR} = 620\ nm$ so it could be interesting. For each sample we have calculated the enhancement factor (EF) in three different points using the Raman peak associated to the aromatic ring breath at $998\,cm^{-1}$ for the BT monolayer and $1002\,cm^{-1}$ for the liquid toluene. All measurements are collected in the same conditions: 3 accumulations of $30\,s$ each. Only for the $H_{eff}$ evaluation we used only 1 accumulation of $30\,s$. The percentage of Ag coverage in all samples are evaluated to be the 20% of the total surface, so the calculated EF should be divided for a factor 0.2, giving the correct EFs called $EF^*$. We used toluene as the reference sample, for this we collect the Raman spectra and the signal for the $1002cm^{-1}$ peak has 4192 counts (Figure 2.19).

Then we started with the measurements on Ag NPs obtained from PS NSs of $330\,nm$ and at the end we analysed also Ag NPs from PS NSs of $722\,nm$. We show, as example, the Raman spectra of Ag NPs arrays from PS NSs of $330\,nm$ (Figure 2.20-a) and $722\,nm$ (Figure 2.20-b) before any thermal treatments.

We calculate the mean value for the EF* of the samples and the results are listed in Table 2.3.

| Dimension of starting PS NSs | Sample | $EF^*$ |
|---|---|---|
| $330\,nm$ | Ag NPs as deposited | $(1.2 \pm 0.3) \cdot 10^5$ |
| $722\,nm$ | Ag NPs as deposited | $(7.5 \pm 2.2) \cdot 10^3$ |

**Table 2.3:** *Enhancement Factor $EF^*$ for different Ag NPs array functionalized with BT*

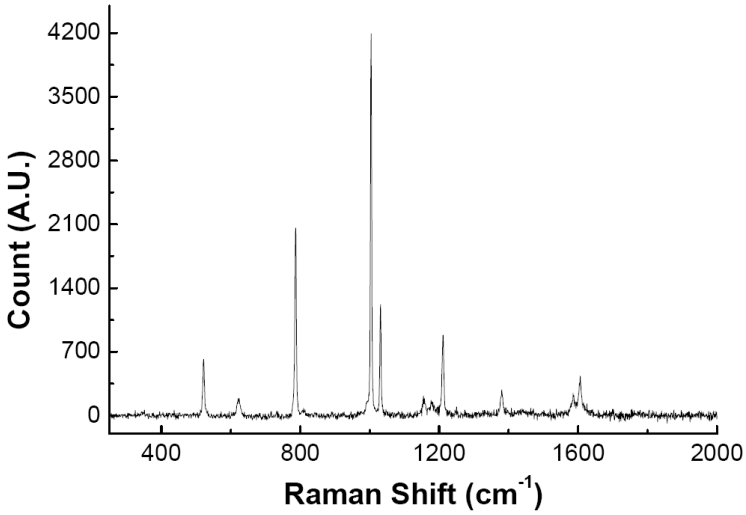


**Figure 2.19:** *Raman spectrum of toluene*

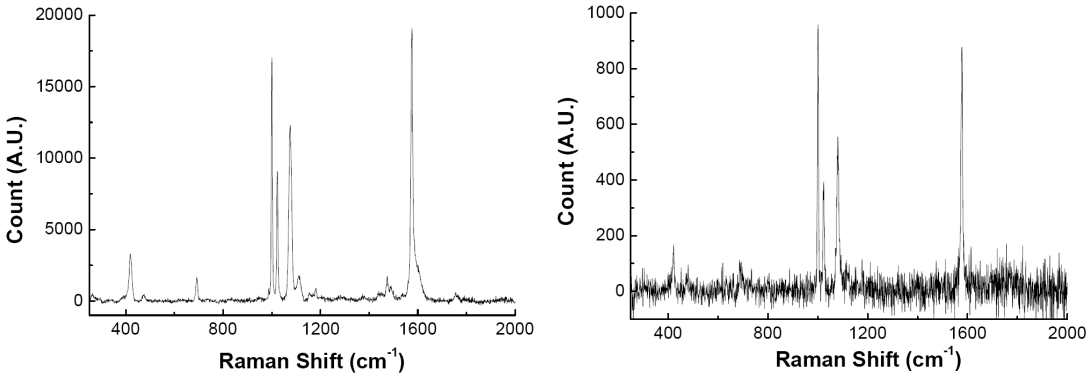


**Figure 2.20:** *Raman spectra of Ag NPs arrays of two different dimensions, functionalized with BT*

To ensure that the detected signal originates from the field enhancement, due to the plasmonic nature of the substrate, we have functionalized a flat film of Ag grown in the same conditions of the nanostructured ones (Figure 2.21).

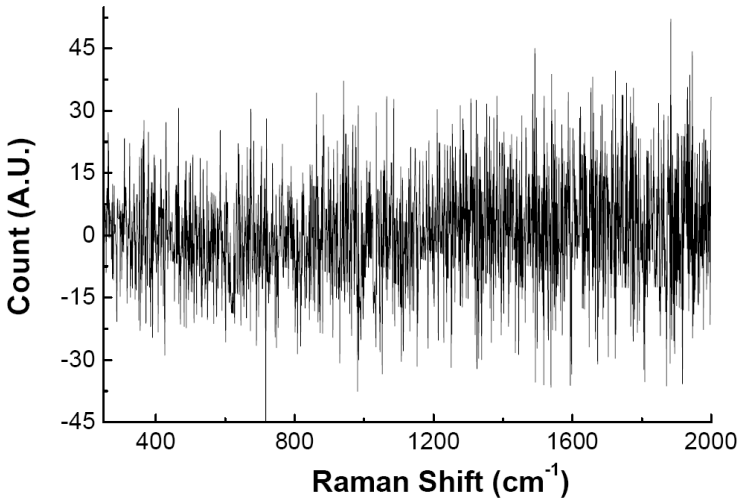


**Figure 2.21:** *Raman spectrum of a flat silver film functionalized with BT*

As expected, no Raman signal from BT is observed. Indeed, without the enhancement of the local field, because of the detection limit of the Raman technique, a single monolayer of material is not detectable.
The results of the above measurements indicate that our Ag NPs arrays can be efficiently used as SERS platforms. Even without a careful optimization of the LSPR peak position a good value of enhancement factor could be achieved. The use of a sample with an optimized $\lambda_{LSPR,max}$ position could rise the EF even of a factor ten or more.

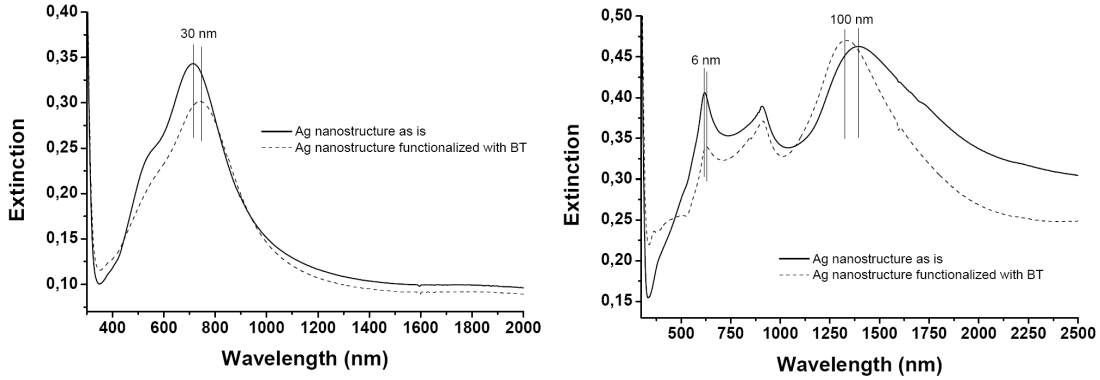


**Figure 2.22:** *Optical spectra of Ag NPs arrays before and after functionalization with BT*

### 2.7.2 LSPR Nanosensors

The localized surface plasmon resonance (LSPR) wavelength shift response, $\lambda_{max}$, of metallic nanoparticles fabricated by NSL has been used to develop another class of nanoscale optical biosensors. The LSPR wavelength shift response of these sensors can be understood, on the most straightforward level, using a model of the refractive-index response of propagating surface plasmons on a planar noble metal surface [47]:

$$\Delta\lambda_{max} = m\Delta n \left[1 - exp\left(\frac{-2d}{l_d}\right)\right] \tag{2.9}$$

Where $\Delta\lambda_{max}$ is the wavelength shift, $m$ is the refractive index sensitivity, $\Delta n$ is the change in refractive index induced by an adsorbate, $d$ is the effective adsorbate layer thickness, and $l_d$ is the characteristic electromagnetic field decay length. While this oversimplified model does not quantitatively capture all aspects of the LSPR nanosensor response, it does provide some guidance for sensor optimization. Particularly, equation 2.9 demonstrates the distance dependence as described by the electromagnetic field decay length, $l_d$. We can also use them as refractive index sensors. To do this, it is necessary to analyze the optical spectra and see if there is a shift of the plasmon resonance due to the binding between the thiol group and the metal, that changes the dielectric constant of the environment of the Ag NPs and so the refractive index. Figures 2.22a,b show the optical spectra, before and after functionalization with BT, of Ag NPs arrays from PS NSs of $330, nm$ and $722\, nm$ respectively.

For the sample from PS NSs of $330\, nm$ we have a red-shift of the principal peak of $30\, nm$, while for the sample from PS NSs of $722\, nm$ we have a red-shift of $6\, nm$ for the first peak and a blue-shift of $100\, nm$ for the band in the IR region.
In another experiment gold NPs arrays have been synthesized and functionalized with

a molecule formed by a Poly-ethylene glycol with a molecular weight of 5000 Dalton, which ends on one side with a methoxy group and the other with a cysteine (MetPEG-cys). The molecule is protected from oxidation by a trithyl group (Trt), which must be separated during the functionalization procedure. Figure 2.23 shows a representation of the used molecule. The use of this modified PEG is required when a "smart" bridge

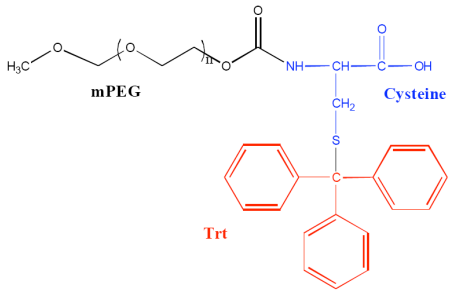


**Figure 2.23:** *Representation of the MetPEG-cys, the molecule used for the functionalization of gold nanostructure*

between the metal nanostructures and the biological environment is needed. By proper functionalization of the other termination it is possible to bond a molecule (e.g. a single strand of DNA) which can link to the target molecule (e.g. the complementary strand). The aim of the project is the development of a sensor based on the shift of the $\lambda_{LSPR,max}$ caused by the change in the local refractive index induced by the bond between the probe and target molecules, and a sensor able to exploit the SERS effect. Cys-PEG was chosen as linker because the Cysteine has a thiol group that can bond to the metal while the other termination can be functionalized with a molecule specific to the desired target. PEG has the function to prevent non-specific physisorption or chemisorption on the metal surface in order to increase the specificity of the sensor.
The steps for functionalization are:

1. cleaning the sample with repeated immersion in water
2. removal of the Trt group of the molecule with Trifluoro acetic acid (TFA)
3. separation of the Trt group by centrifugation at $15.000\,rpm$, at a temperature of $4°C$, for $10\,min$
4. immersion of the sample in the solution of water and TFA containing the molecule of interest and waiting for $24\,h$
5. drying of the system in vacuum

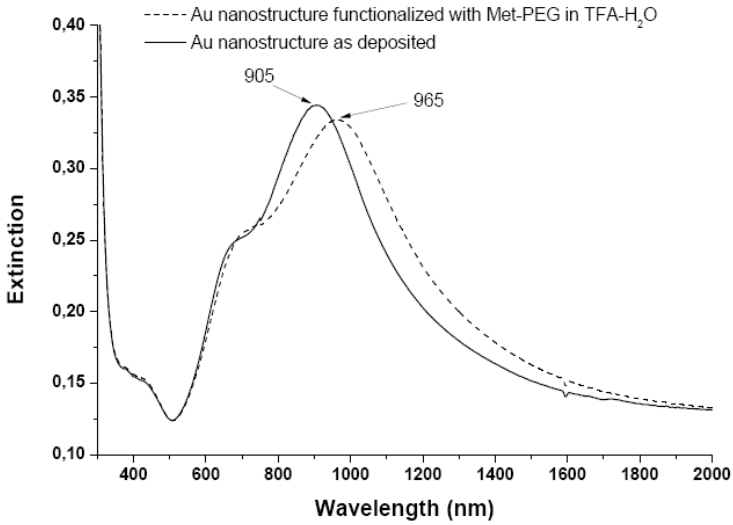


**Figure 2.24:** *Optical spectra of the Au NPs arrays before and after functionalization with MetPEG-cys*

Fig.2.24 shows the optical spectrum of gold nanostructure before and after functionalization.

Gold nanostructures work well are sensible at the variation of local refractive index caused by the PEG functionalization: in fact, we have a red-shift of the principal peak of 60 $nm$ after the bonding with the PEG. The shape of the spectrum is not changed: this means that the chemistry involved in the functionalization process doesn't modify the metal nanostructure as confirmed by the SEM images showed in Figure 2.25.

This procedure was also tested for Ag NPs arrays, but in this case the chemistry of the environment modifies the nanostructure (Figure 2.26). The same result was obtained using the first solution of water and TFA, which on the contrary worked for gold. To overcome the problem for silver NPs, which are more interesting than gold, because of the more intense local fields, we tried different solutions:

1. eliminate TFA
2. neutralize TFA with $Na_2CO_3$
3. substitute TFA with HCl:
   - 3-a. use an aqueous solution of HCl 0.2 $M$
   - 3-b. neutralize HCl with NaOH, to give an aqueous solution of NaCl 0.2 $M$
   - 3-c. neutralize HCl with $AgNO_3$

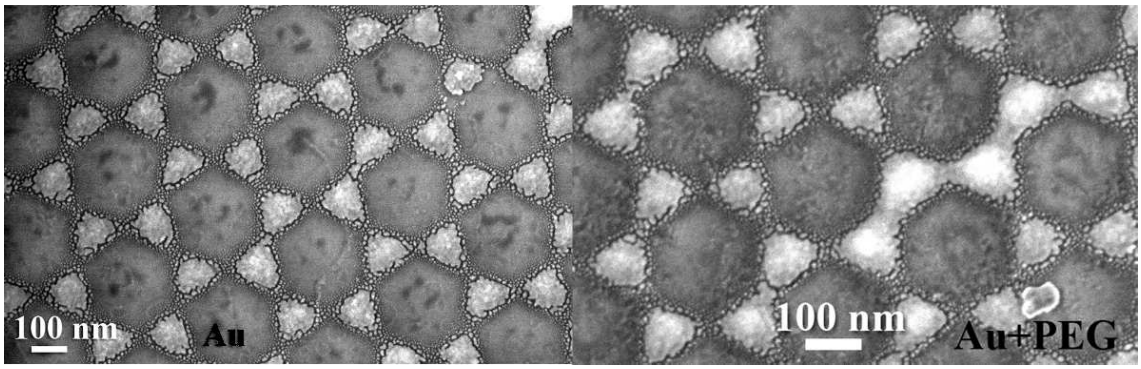


**Figure 2.25:** *SEM images of gold nanostructures before (*Left*) and after (*Right*) the functionalization with Cys-PEG. The* Right *image look a little bit blurred because of the presence of the polymer.*

Silver nanoparticles remain unaltered only when the reaction environment becomes basic or when the TFA is removed from the solution. This would means a further step in the procedure consisting in a chromatographic purification of the deprotected polymer. This step has a serious drawback of a 50% loss which made it unsuitable for the implementation of a cheap device. We didn't try to functionalize the silver nanostructures without TFA, because this means the use of a big quantity of MetPEG-cys, as consequence of the fact that more than 50% is lost when we separate it from TFA for chromatography.

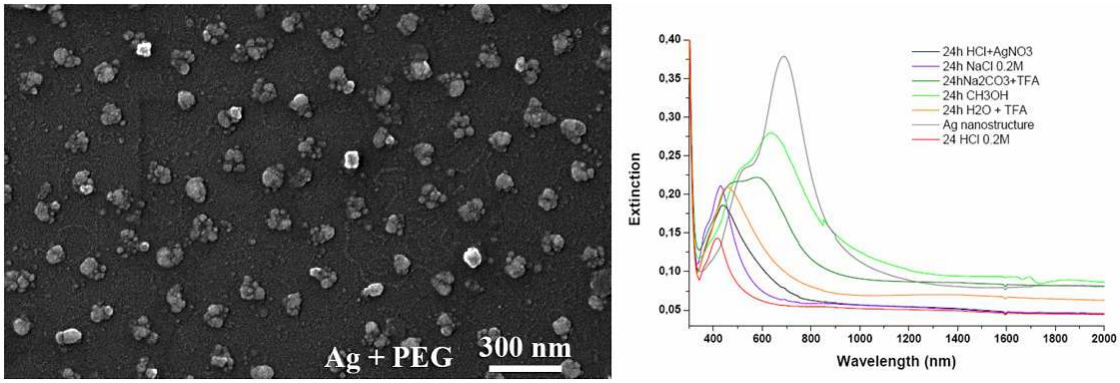


**Figure 2.26:** Left: *SEM image of a silver nanostructures after functionalization with Met-PEG-Cys with the standard procedure. Nanoparticles are strongly influenced by the environment.* Right: *absorption spectra of silver nanostructures in various environment*

From all these tests, we can derive an important information: NaCl in concentration similar to the physiological solution ($0.2\,M$), after $24\,h$ modifies the nanostructure. This means that measurements of biological molecules attached to silver NPs immersed in this environment have to be carried out in a shorter time.

### 2.7.3 Local Temperature Measurement

Recently a great interest has been drawn by the use of plasmonic nanoparticles for biolabelling, thermal ablation of cancer cells and drug tailored delivery. In this context a deep understanding of nanoparticle heat transfer and thermal properties is of paramount importance in order to optimize design parameters such as particles shape, composition, and surface configuration. Typical approches to probe the local temperature at the nanoscale include scanning thermal and thermoreflectance microscopy and Raman spectroscopy. The latter two are non invasive and non contact techniques, but are unsuitable for metallic surfaces (Raman) or require lenghty calibration procedures (reflectance). Very recently two different promising techniques to probe the local temperature in the vicinity of metallic nanosctructures emerged: (1) fluorescence anisotropy spectroscopy, which is able to probe the heat source function of plasmonic structures and (2) fluorescence thermometry which provides submicrometric temperature mapping with relative ease. Fluorescent thermometry, based on the measurement of the probe temperature dependent signal, has already found several applications, the most notable being integrated circuit temperature monitoring. We employ fluorescence thermometry to probe the local temperature of plasmonic nanostructures illuminated by a multiple line pump laser source. Eu thenoyltifluoroacetonate (EuTTA) PL intensity is known to be sensible to its environment temperature, so we use it to measure the temperature reached by silver nanostructures being illuminated by light under resonance condition with LSPR.
EuTTA was deposited over the nanostructures as a dopant in a thin PMMA film. Other two samples, which serve as references, were synthesized: a PMMA film on a bare sodalime glass substrate and a PMMA film on a $127nm$ silver film on sodalime glass. Silver thickness was measured by AFM, while PMMA was measured via ellipsometry, the data are summarized in table 2.4. For the synthesis of the silver nanostructures, a self assem-

| Sample name | PMMA layer | metallic layer |
|---|---|---|
| EuRef | $20 \pm 3$ nm | none |
| EuAgFilm | $22 \pm 3$ nm | $127 \pm 5$ nm Ag film |
| EuAgNP | $20 \pm 3$ nm | Ag nanotriangles |

**Table 2.4:** *Sample synthesized on the present work. PMMA layer was measured via ellipsometry.*

bled monolayer was deposited on sodalime glass according to the method described in section 1.4. Silver was deposited by magnetron sputtering at 20 W for 400s. The sample was then immersed in a beaker containing toluene (*puriss.*) for a couple of minutes and then sonicated for 1 minute to dissolve the PS nanospheres and remove them from the

substrate, leaving only the silver nanostructures. To tune the surface plasmon resonance peak, in order to overlap with the wavelength emitted by the Ar laser, nanostructures were heated for $30min$ at $350°C$.
EuTTA was deposited on the nanostructures as a dopant in a film of PMMA. A 10% PMMA (MW= 250.000) solution was prepared leaving PMMA in toluene in a oven at $70°C$ overnight. In the same way a solution of 50mM EuTTA in toluene was prepared; as the EuTTA in such a high concentration is not stable at room temperature, so the solution was used while warm. The PMMA and EuTTA solution were mixed together to obtain a concentration of 25mM in EuTTA and 0.5% wt of PMMA; toluene was always used as solvent. This fresh prepared solution was immediatly used for coating the nanostructures with a G3P Spin Coater (Specialty Coating Systems) at 4000rpm for 60s. An $N_2$ pulsed laser ($\lambda$= 337.1 nm) has been employed for the EuTTA photoluminescence excitation. Pulse width and energy are 0.5 ns and 2 J respectively, as provided by the manufacturer. Measurements are performed with 128 pulse burst at 2Hz frequency. A variable power multiple line Ar source was employed as pump laser. All the laser line have been employed at once in order to maximize the incident power. Even if the laser is a multiple line, the two wavelength at which 90% of the power is produced are $488nm$ and $515nm$. The overall emitted power is monitored by an on-board power meter We took particular care to align the two laser on the same spot, to make sure that we measure the Eu signal coming from the excited plasmonic zone. The sample was placed in a cryostat with quartz windows, under vacuum (lower than $0.5mbar$) and we use an external heater to maintain the temperature constant at 21°C. To measure the rise in temperature caused by the pump laser, we let it illuminate the sample for 5 minutes to thermalize before performing the "laser ON" measurement, then when we switch the Ar laser off, we let the sample cool down for 20 minutes before performing the "laser OFF" measurement.
EuTTA fluorescence signal at $\lambda = 613nm$ was collected with two 3" lenses which focalize the light into a monocromator. In front of the monocromator we put three high pass filter, to completely absorb the laser light scattered from the sample and prevent it from reaching the detector. Light intensity was measured with an Hamamatsu R928 Photomultiplier Tube coupled via a 50 kΩ resistance with a Tektronix TDS 7104 digital oscilloscope (bandwidth 1GHz), that we used for lifetime measurement.

Figure 2.27 shows the PL intensity of the three samples when Ar laser was used as a pump with different power. All the fluorescence intensity were corrected by normalization to $N_2$ laser power which was measured with *an external diode*. The luminescence intensity shows a significant decrease when the pump laser illuminate the nanostructures because of the heating induced by plasmonic coupling with the incident light. The effect is totally

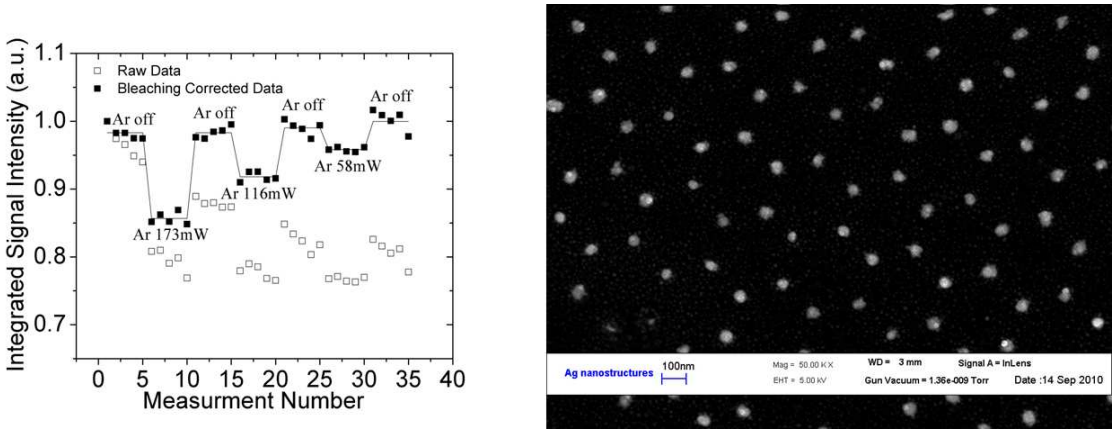


**Figure 2.27:** *EuTTA luminescence intensity when illuminated by Ar laser*

reversible: the EuTTA PL intensity is restored once the pump laser is shut down. The magnitude of the effec depend on the Ar laser power and greatly changes among the samples. It is almost negligible for the bare PMMA doped thin film (EuRef), it is very low for the silver thin film (EuAgFilm) while for the silver nanostructures it is very evident. The difference can be explained by the different absorption coefficient of the three samples (Figure 2.28). The PMMA film has an extinction of 11 % and a reflectance of 7.8 % so we can conclude that the absorption in the $450 - 550nm$ region is less than 3%. The silver film is completely opaque (trasmittance $\approx 0\%$ ) and its reflectance is 93% so the absorbed portion is $\approx 7\%$ of the Ar light. We synthesize silver nanostructures in order to obtain their SPR peak in the $600nm$ region. Deconvolving the extinction peak to separate the reflecting and the absorbing contributions we can see that the absorption peak (the blue line in Figure 2.28 overlaps the spectral region in which are located the Ar laser lines). For this sample 61.1% of the Ar laser ligth is being absorbed causing the heating of the nanostructures.

EuTTA, like all bidiketonate complexes, exhibit a narrow emission band that can be excited via an intramolecular energy transfer from ligands to the rare earth ion under UV excitation. The mechanism, as explained in [48], consists in 4 steps:

1- Uv light in the wavelength range of 300 - 400nm is absorbed by the ligands,

2- Excited ligands decay from the excited singlet to the lowest triplet state,

3- Energy is transferred from the triplet state of the ligands to the quasi resonant energy state of $Eu^{3+}$ via a Dexter process,

4- The excited $Eu^{3+}$ ion decays to the ground state emitting a photon at 515 nm

The third step is crucial in determining the quantum yield and so the temperature dependency of the fluorescence intensity.

Organic Eu complexes under UV irradiation in presence of oxygen are known to loose their fluorescence properties because of the presence of the singlet oxygen which causes the breaking of the complex [49]. To minimize this bleaching effect, which is unavoidable, we placed our sample under vacuum (lower than $0.5mbar$). Bleaching produces an exponential decay of EuTTA fluorescence, with a characteristic decay time $\tau_{bleaching} = 0.46min$. Each sample was let under exposure of $N_2$ laser light for 20 minutes ($t > 40 \times \tau_{bleaching}$), to let the bleaching reach a saturation state. Moreover a linear correction was applied to data, to compensate the loss of molecules caused by the residual bleaching during the actual measurements.

Fluorescence intensity or fluorescence lifetime are temperature dependent and in principle could be used to determine the sample temperature. Fluorescence intensity is more sensitive and easy to detect, but it depends on experimental parameters like intensity of the excitation light or other sources of systematic errors like straylight. Lifetime is independent from the experimental apparatus but it is less sensitive to temperature changes and require an accurate analysis. As plotted in the inset of Figure 2.29b the decay of the luminescence differs from a simple single exponential decay model for all the three samples and it is better described by a stretched exponential decay (equation 2.10):

$$I(t) = I(t=0) \cdot \exp -(t/\tau)^{\beta} \tag{2.10}$$

where $\tau$ is the decay time, and $\beta$ is the stretching parameter. Both are related to the effective relaxation time $\tau_{eff} = \frac{\tau}{\beta}\Gamma(\frac{1}{\beta})$ When $\beta = 1$ the standard exponential decay is recovered, while $0 < \beta < 1$ the exponential curve is characteristically stretched.

In all the measured sample the decay has the $\beta$ coefficient significantly different from 1.

In our case the determination of the lifetime is complicated because of its non single

| Sample | $\tau_{eff}(\mu s)$ | $\beta$ |
|---|---|---|
| Eu ref | 0.052 ± 0.015 | 0.70 ± 0.20 |
| Eu Ag film | 0.054 ± 0.016 | 0.53± 0.16 |
| Eu Ag NS | 0.0009 ± 0.0002 | 0.39 ± 0.12 |

**Table 2.5:** *Measured Lifetime Data*

exponential decay. That may cause a non univocal estimation of its value because of the correlation among the parameters, so different set of $\beta$ and $\tau$ could give indistinguishable results. This in addition to the low sensibility of the lifetime lead us to choose luminescence intensity as a parameter to measure the rise in temperature of the sample under laser irradiation. To use the luminescence intensity we measured the $N_2$ laser intensity and correct the data normalizing EuTTA intensity by the excitation laser intensity and

use three high pass filter to prevent straylight from the pump laser to enter in the revelator.

To determine the actual temperature of the samples we calibrated the system by using an external heating system to change the temperature, in order to define a function between the temperature and the EuTTA PL intensity so as to obtain a calibration curve. In figure 2.29 we report the relative measured intensity of EuTTA as we change the temperature. Once normalized the fluorescence intensity for the first point ($22.2C$ in our case) all the three samples has the same decay rate.
With the aid of this calibration curve we were able to determinate the temperature reached by silver nanostructures as a function of the pump laser power. Figure 2.29 shows that silver nanoparticles illuminated by the $160mW$ Ar laser can reach temperature as high as 45°C, starting from room temperature = 21°C

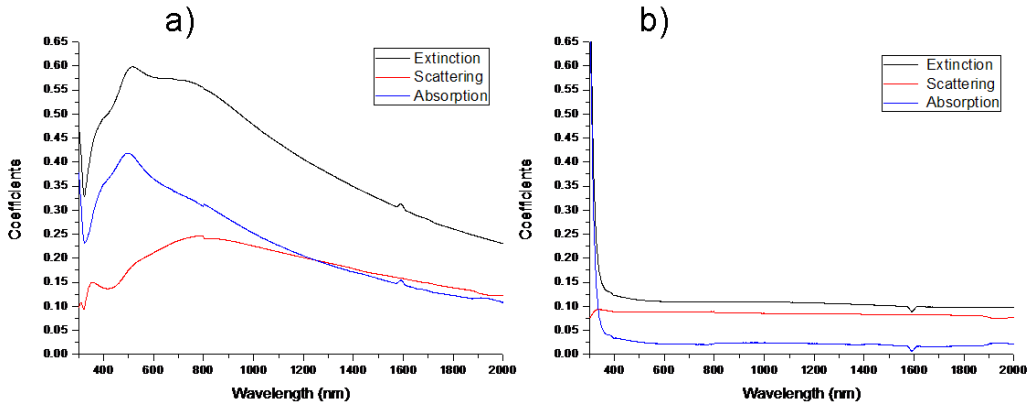


**Figure 2.28:** *Measured Extinction, Scattering, Absorption Cross Section of the PMMA covered Ag nanostructures* (a) *and the PMMA on bare sodalime glass sample* (b)

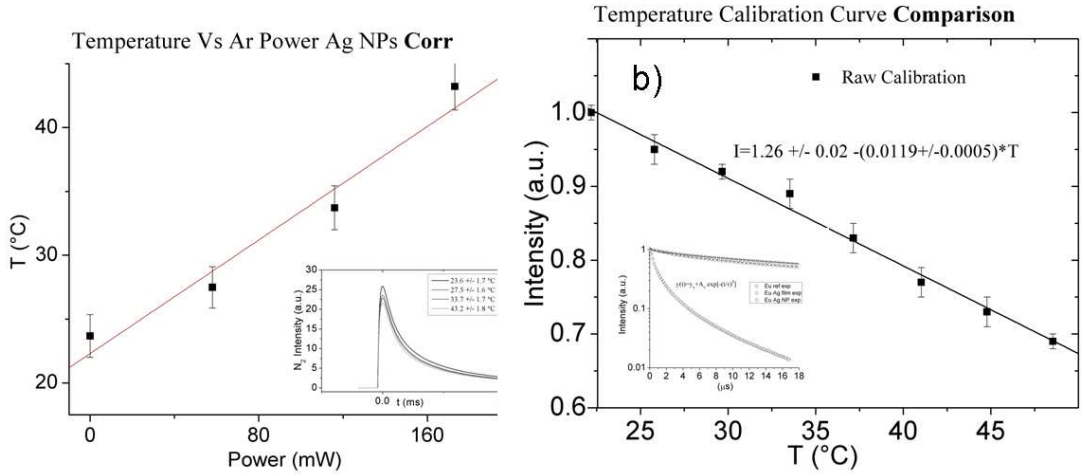


**Figure 2.29:** *Calibration curve (left) and temperature reached by the silver nanostructures as function of the Ar laser power.*

# Chapter 3

# Nano Hole Array

Since Ebbesen and co-workers [50] discovered extraordinary optical transmission (EOT) through sub-wavelength noble metal nanohole arrays (NHA) there has been significant effort to fabricate nanohole arrays with well-controlled electromagnetic properties. Extraordinary optical transmission is an optical phenomenon in which a structure containing subwavelength apertures in an opaque screen transmits more light than might naively be expected on the basis of either ray optics or even knowledge of the transmission through individual apertures. The phenomenon was discovered for two-dimensional periodic arrays of subwavelength holes in metals. In the original experiments, the holes were drilled in optically thick metal films and, therefore, the electromagnetic waves could only tunnel through the apertures in the transmission process. Surprisingly, such arrays may, for certain wavelengths, exhibit transmission efficiencies that, once normalized to the total area of the holes, exceed unity. In other words, for these wavelengths a periodic array of subwavelength holes transmits more light than a large macroscopic hole with the same area as the sum of all the small holes. Moreover, EOT may enable a multitude of applications as the remarkably high transmission efficiencies and, concomitantly, high local field enhancements can be achieved at wavelengths that can be engineered through the geometry of the metal surface. Surface plasmon (SP) waves, collective oscillations of conduction electrons, contribute directly to the EOT effect [51] while also facilitating surface-enhanced spectroscopies. For the most part, nanohole arrays have been fabricated using expensive and time-intensive high-resolution serial techniques such as electron beam lithography (EBL) [52] and focused ion beam (FIB) milling.[50] In some cases, advanced soft lithography methods such as PEEL (a combination of phase-shift lithography, etching, electron-beam deposition, and lift-off) or soft nanoimprint techniques have been successfully employed to fabricate nanohole arrays.[53] In a recent example, Chen et al. fabricated square lattice gold nanohole arrays with sub-250 nm diameter using UV nanoimprint lithography com-

bined with reactive ion etching and a Cr/Au lift-off process.[54] With this method, the authors varied the nanohole diameter and periodicity with well-ordered nanohole arrays up to $1cm^2$ and examined systematic shifts in the transmission spectra of structural variations, baths with varied refractive index, and thiol chemisorption. While these methods have facilitated important fundamental studies, the field would greatly benefit from a simpler massively parallel fabrication method that can pattern nanohole arrays with a deep ultraviolet (DUV) patterning resolution, i.e., around 200 nm, without using an exposure tool, photomask, or imprint mold. The approach followed on the present work relies on the nanosphere lithography (NSL) technique conceived of (as "natural lithography") by Deckman et al.[14] and popularized by Van Duyne and co-workers. [23] Instead of employing an as-assembled 2D colloidal array as a shadow mask for nanostructure deposition, we used a reactive ion etching (RIE) step to shrink the nanospheres before metal deposition, facilitating the formation of nanohole arrays after removal of the nanospheres. By controlling the original nanosphere size, etching time, metal deposition thickness, and metal deposition angle, it is possible to tune the nanohole spacing, size and aspect ratio, and, accordingly, the plasmonic properties.

## 3.1 RIE etching of SA masks

The standard technique for producing plasmonic nanostructures with nanospheres lithography consist in three steps: 1) self assembly of a monolayer of colloidal particles; 2) deposition of metal; 3) liftoff of the monolayer. We will insert a fourth step in the NSL process to modify the self assembled mask before the deposition. This step consists in the reduction of the dimensions of PS nanospheres, using a chemical ion-assisted etching. The result is a two-dimensional periodic non-close-packed array of PS nanospheres, that can be used as a mask for metal deposition to allow the formation of nanohole arrays, after removal of the nanospheres [55, 56]. The etching process should be able to reduce gradually and with a controlling rate the dimension of the PS nanospheres without altering the periodicity and the order created by self assembly. To dry etch the PS nanospheres, we used the Reactive Ion Etching (RIE) process. Reactive ion etching is an etching technology used in microfabrication. It uses a chemically reactive plasma to remove material deposited on Si substrate. The plasma is generated under low pressure (vacuum) by an electromagnetic field. High-energy ions from the plasma attack the sample surface and react with it. A typical (parallel plate) RIE system consists of a cylindrical vacuum chamber, with a wafer platter situated in the bottom portion of the chamber. The wafer platter is electrically isolated from the rest of the chamber, which is usually grounded. Gas enters

through small inlets in the top of the chamber, and exits to the vacuum pump system through the bottom. The types and amount of gas used vary depending upon the etch process. Gas pressure is typically maintained in a range between 1 - 500 mtorr. Plasma is initiated in the system by applying a strong RF (radio frequency) electromagnetic field to the wafer platter. The field is typically set to a frequency of 13.56 MHz, applied at a few hundred watts. The oscillating electric field ionizes the gas molecules by stripping electrons and creating a plasma. Because of the large voltage difference, positive ions tend to drift toward the wafer platter, where they collide with the samples to be etched. The ions react chemically with the materials on the surface of the samples, but can also knock off (sputter) some material by transferring part of their kinetic energy. Due to the mostly vertical delivery of reactive ions, reactive ion etching can produce very anisotropic etching profiles, which contrast with the typically isotropic profiles of wet chemical etching. Etch conditions in an RIE system depend strongly on the many process parameters, such as pressure, gas flows, and RF power. A modified version of RIE is DEEP Reactive Ion Etching, used to excavate deep steep-sided features in wafers, with aspect ratios of $20:1$ or more. What distinguishes DEEP-RIE from RIE is the etch depth: practical etch depths for RIE (as used in IC manufacturing) would be limited to around $10\,\mu m$ at a rate up to $1\,\mu m/min$, while DEEP-RIE can etch features much greater, up to $600\,\mu m$ or more with rates up to $20\,\mu m/min$ or more in some applications.
We studied three etching conditions: in the first we worked with a RIE system in an atmosphere of $CF_4 + O_2$ at a ratio $19:1$; in the second we use a RIE system but with a different as mixture: an atmosphere of Ar and $O_2$ in equal proportions; finally in the third we use a DEEP-RIE system in an atmosphere of $O_2$.
Table 3.1 summarizes all the parameters used in the three different RIE conditions.

| | $I^\circ$ condition | $II^\circ$ condition | $III^\circ$ condition |
|---|---|---|---|
| System | DEEP-RIE | RIE | RIE |
| Atmosphere | $O_2$ | Ar+$O_2$ | $CF_4 + O_2$ |
| Flux (sccm) | 40 | $15; 15$ | $28.5\,(CF_4); 1.5\,(O_2)$ |
| Bias (V) | 38 | 115 | 230 |
| Pressure | $4\,mTorr$ | $3.8 - 4.2 \cdot 10^{-1}\,mbar$ | $2.3 \cdot 10^{-1}\,mbar$ |
| Etching time | $50; 100; 150\,s$ | $1 - 12\,min$ | $2\,min$ |

**Table 3.1:** *RIE Etching conditions*

A self assembled monolayer of 722 nm and 330 nm PS nanoparticles was deposited on a $p$-doped (110) Silicon substrate. Si was used to make the SEM characterization easier to perform. The first condition for the etching of the self assembled monolayer was performed with a DEEP RIE system. We processed masks of PS NSs of both 330 nm and 722 nm,

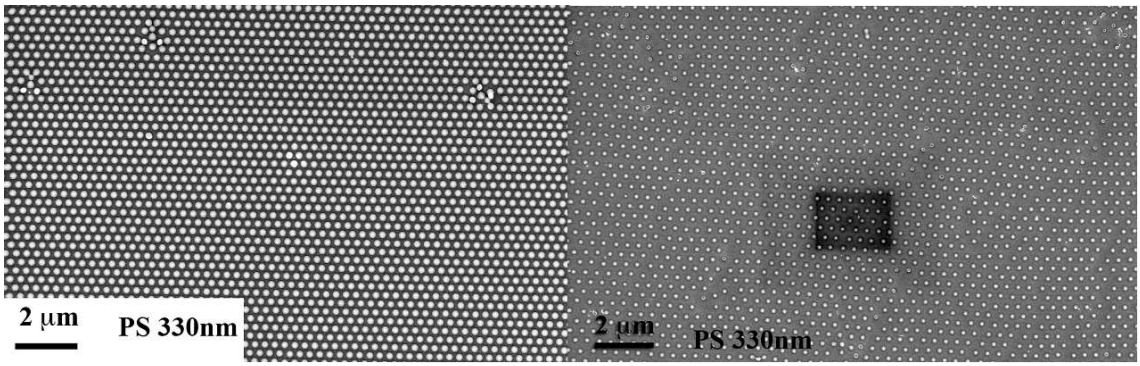


**Figure 3.1:** *SEM images of etched PS NSs masks of* 330 *nm: etching in atmosphere of* $O_2$

using the parameters listed in Table 3.1. We etched the smaller nanospheres for 50, 100 s and the bigger for 50, 100, 150 s. In Figure 3.1 SEM images of the samples of smaller nanospheres, etched for the different times are shown, Figure 3.2 shows SEM images of the samples of bigger nanospheres, etched for the different times and in Table 3.2 the mean values of the PS NSs size are summarized. The DEEP RIE system is able to produce a

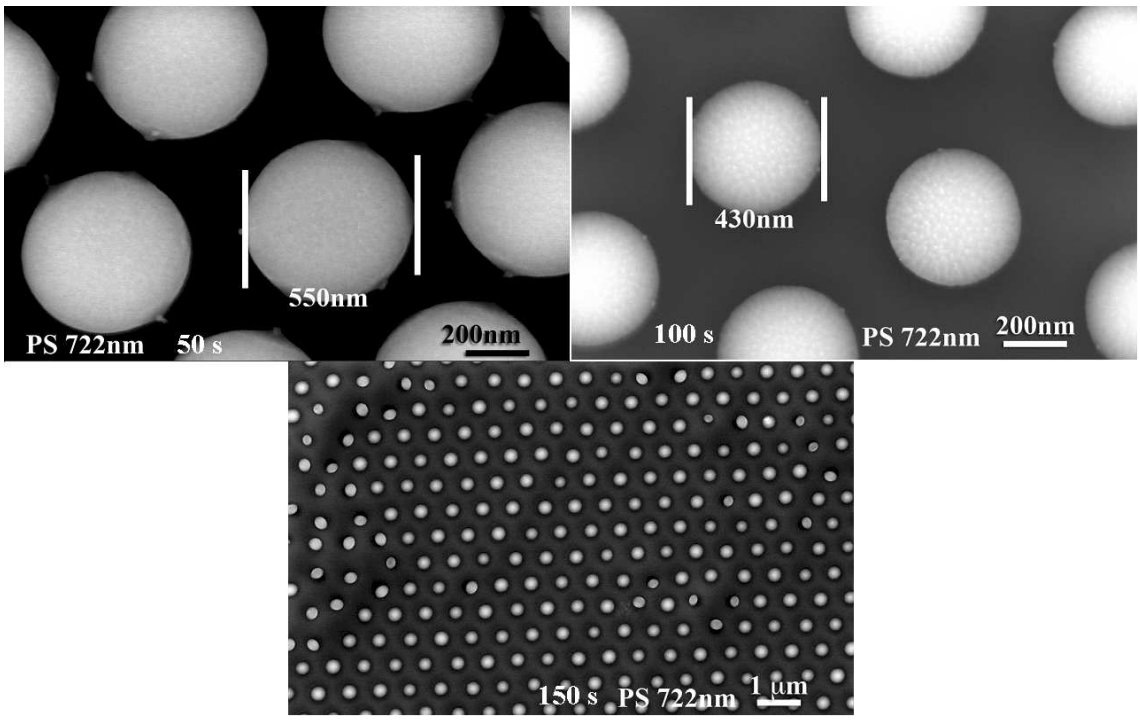


**Figure 3.2:** *SEM images of etched PS NSs masks of* 722 *nm: etching in atmosphere of* $O_2$

more dense plasma so, as could be expected, it has an etching rate much higher than the Ar + $O_2$ RIE: comparing figure 3.6 and 3.2 one can see that after 50 s of DEEP RIE PS

| Sample | Etching time (s) | Mean dimension (nm) | Standard deviation |
|---|---|---|---|
| PS 330 $nm$ | 0 | 325 | 7 |
| PS 330 $nm$ | 50 | 210 | 4 |
| PS 330 $nm$ | 100 | 110 | 6 |
| PS 722 $nm$ | 0 | 705 | 20 |
| PS 722 $nm$ | 50 | 600 | 20 |
| PS 722 $nm$ | 100 | 425 | 25 |
| PS 722 $nm$ | 150 | 265 | 25 |

**Table 3.2:** *Calculation of the PS NSs size for the DEEP-RIE process in atmosphere of* $O_2$

nanospheres were etched slightly more than after 3 min of RIE. In Figure 3.3 are shown the histograms describing the size distribution of the etched nanopsheres's dimensions starting from PS NSs of 330 nm and 722 nm respectively, while Figure 3.4 is a plot of the etched dimensions as function of the etching time: the experimental data are fitted with a linear fit. From the angular coefficient we derive the etching for the DEEP-RIE rate that in the two cases are:

$$\gamma_{DEEPRIE,722} = 2.6 \pm 0.4\, nm/s\; for\; PS\; NSs\, 722\, nm \tag{3.1}$$

$$\gamma_{DEEPRIE,330} = 2.1 \pm 0.4\, nm/s for\; PS\; NSs\, 330\, nm \tag{3.2}$$

For high etching times nanospheres do not seem to preserve the circular projection on the substrate. Figure 3.5 shows SEM images of the PS nanospheres after the DEEP RIE etching are shown. The sample were cut by cleavage along the silicon crystalline plane and measured with an angle of 75° from the normal to the surface. From the side view it is possible to see that nanoparticles are not etched isotropically but the etching along the vertical axis is much higher than the etch along the horizontal axis and this results in producing lens-shaped PS nanoparticles. For higher etching time these nanospheres show the tendency to lean on a side.

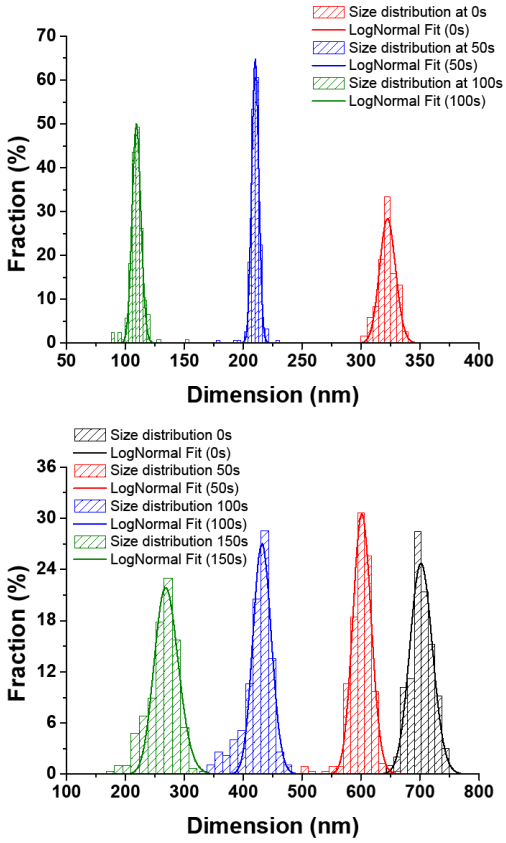


**Figure 3.3:** *Size distribution of etched dimension of nanospheres masks at different times: the starting dimension of the nanospheres was* 330 *nm in one case and* 722 *nm in the other case.*

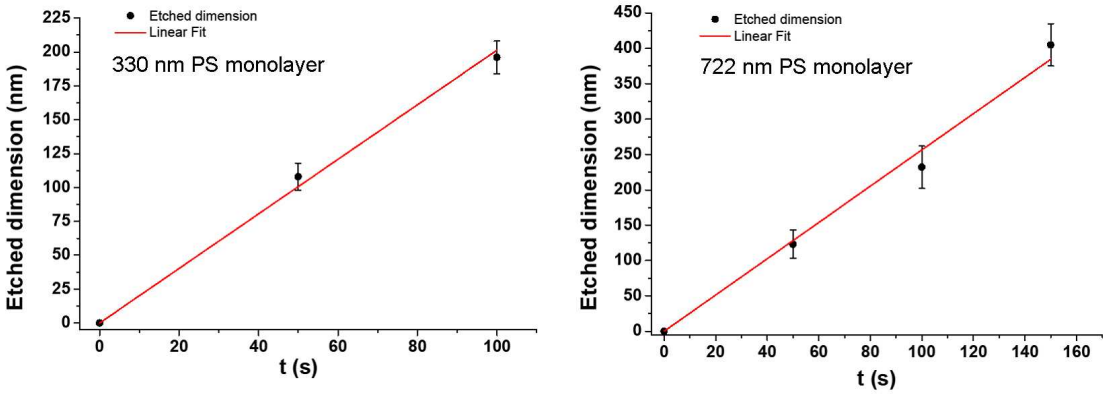


**Figure 3.4:** *DEEP RIE etching rate for PS NSs masks of* 330 *nm and* 722 *nm: points are the experimental data and line is the linear fit*

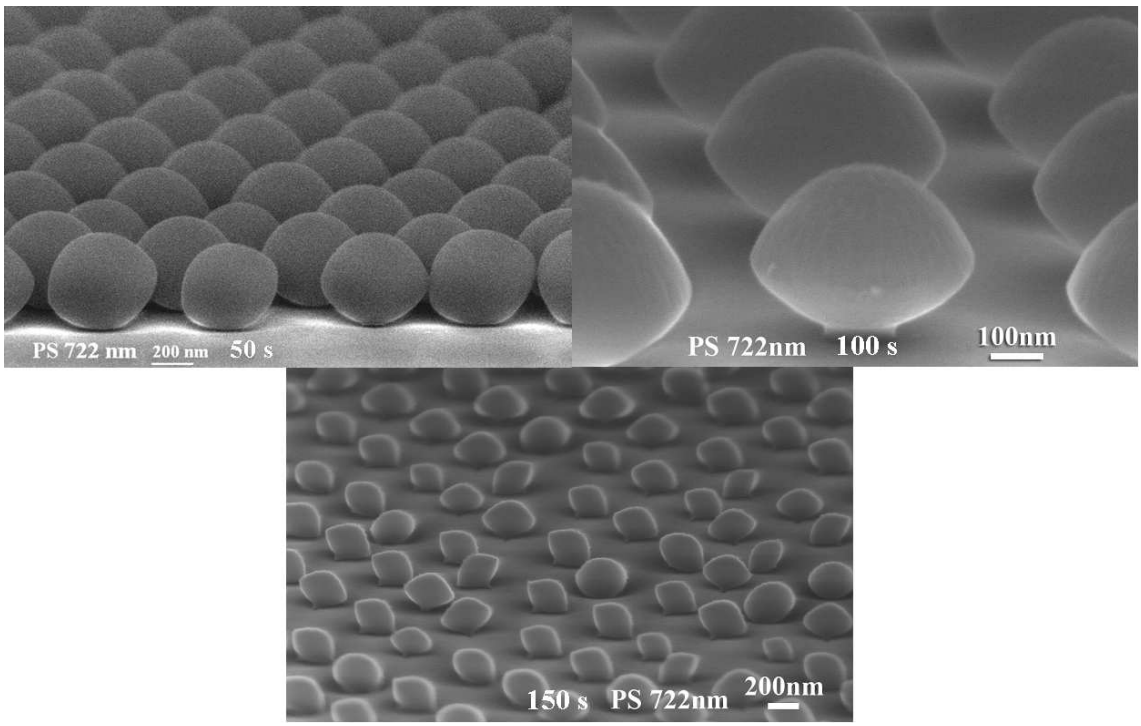


**Figure 3.5:** *Cross-SEM images of etched PS NSs masks of* 722 *nm: etching in atmosphere of* $O_2$

| Sample | Etching time (min) | Mean dimension (nm) | Standard deviation |
|---|---|---|---|
| PS 722 $nm$ | 0 | 705 | 20 |
| PS 722 $nm$ | 1 | 660 | 25 |
| PS 722 $nm$ | 3 | 605 | 20 |
| PS 722 $nm$ | 6 | 510 | 25 |
| PS 722 $nm$ | 12 | 0 | |

**Table 3.3:** *Calculation of the etched dimensions of PS NSs masks for the RIE process in atmosphere of* $Ar + O_2$

We also explored different way to etch the PS nanospheres. An attempt was made using a standard RIE system with a $Ar+O_2$ atmosphere and the parameters listed for the second condition in Table 3.1 to process masks of PS NSs of 722 nm. We used four different etching times, $1, 3, 6, 12\,min$, to estimate the etching rate. Figure 3.6 shows SEM images of the samples etched for the different times and Table 3.3 shows the results of the measurements of the PS NSs size after RIE processing of the four samples.

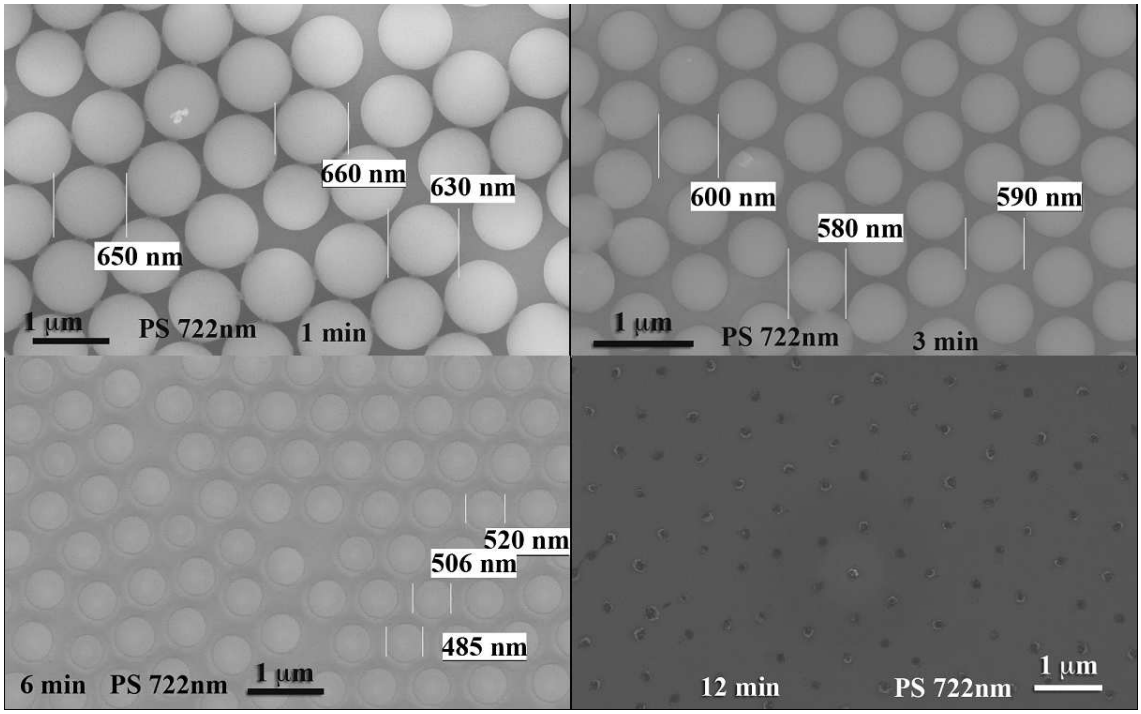


**Figure 3.6:** *SEM images of etched PS NS masks of 722nm: etching in atmosphere of* $Ar + O_2$

The mean values are obtained mediating $\approx 150$ data, which are plotted in different histograms and fitted with a LogNormal curve as is shown in Figure 3.7. It is clear

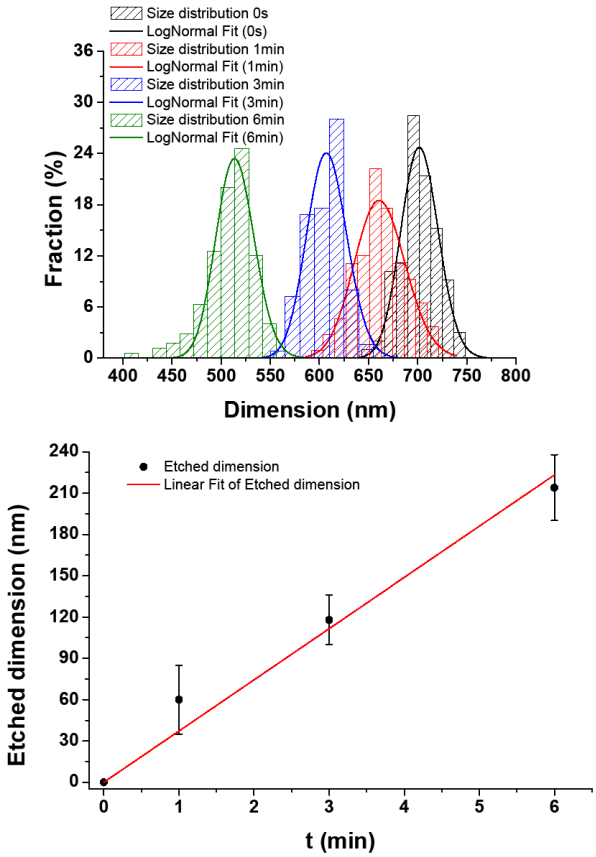


**Figure 3.7:** *Size distribution of the dimension of PS NSs masks at different etching times and estimation of the etching rate for PS NSs masks of* $722\,nm$*: points are the experimental data and line is the linear fit*

that after $12\,min$ no PS NSs remained on the substrate, so for the estimation of the RIE etching rate, we will not consider this sample, because it is possible that the same behaviour happens for etching time smaller. Figure 3.7 is a plot of the etched dimensions as function of the etching time. Data are fitted with a linear fit and from the angular coefficient of the fit we can derive the etching rate$\gamma_{RIE}$ , that in this case is:

$$\gamma_{RIE} = 0.65 \pm 0.05 \ nm/s \tag{3.3}$$

If we analyse, at higher magnification, the SEM images (Figure 3.8) we see that after RIE processing there is not only a reduction on the dimension of the nanospheres, but also a modification of their surfaces. The spheres's surfaces become more rough, with a surface similar to a golf ball. This is not a big problem for our purposes, since we use the spheres only as a mask for the metal deposition and then the mask is removed. It is important to

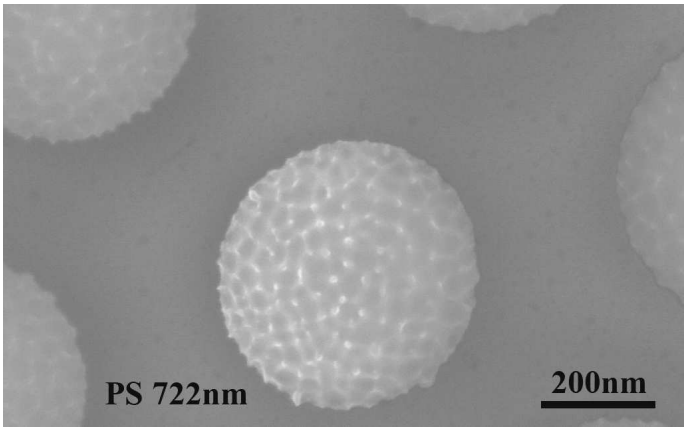


**Figure 3.8:** *SEM image of a nanosphere etched for* 6 *min with a RIE system in an atmosphere of* $Ar + O_2$

notice that after the etching the spheres still have their initial periodicity (i.e. the same center to center distance) and also their projection on the substrate surface is still a circle. So that circular hole is formed on the deposited metal film once the mask is removed.
We tried to use a third condition for nanospheres etching with a mixture of $CF_4$ and $O_2$, which is often used during etching process on materials deposited on silicon substrate. However, this condition was later excluded, because the reactive gases don't etch only the nanospheres, but also the substrate. Cl and F ions are used in the IC and MEMS manufacturing to etch the silicon to create nanostructures. In our experiments etching of the silicon layer is not necessary and could also have a detrimental effect because of the roughness induced in the substrate, so it was necessary to work in different conditions.
In the synthesis of the samples used for the optical characterization we decided to work with the DEEP-RIE system and the same etching parameters listed in table 3.1

## 3.2 Nano hole array synthesis

After the etching step, a thin layer of metal was deposited on the modified mask via magnetron sputtering. The metal layer has to be thick enough to be opaque for the incoming light, but if we deposit it too thick a continuous film between the metal on top of the spheres and the one on the substrate could be formed, making the liftoff step very difficult and reducing the quality of the nano hole array.

### 3.2.1 Structural characterization

722 nm PS nanoparticles were self assembled to create a colloidal mask according to the procedure described in chapter 1.4. Masks were deposited on glass slide, for optical characterization. DEEP RIE etching treatment for 50, 100, 150 s was done to reduce the PS nanospheres size. Silver or gold were deposited on the etched self assembled monolayer. Silver was deposited at 10 W for 800 s while gold was deposited at 20 W for 240 s. For both the samples sputtering parameters were chosen to obtain a $\approx$ 50 nm thick metal layer. The two metals were deposited on the three samples during the same deposition, to obtain the same thickness on all the three samples. Atomic force microscopy was used to characterize the resulting nano hole array. In Table 3.4 the measured thickness of the resulting nanohole array are summarized.
In Figure 3.9 the comparison between the mask after the etching step and the gold monolayer is presented. After the 50 s DEEP RIE etch an hybrid structure between the periodic particles array and the nano hole array is formed. The sample present a continuous metal grid, encircling the circular holes, which vertical profile features peaks and valleys. The resulting conformation could be caused by the non perpendicular flux of metal atoms, as we described in chapter 2.3.1: the PS nanoparticles are 100 nm far from each other, so during the deposition of 50 nm film the distance between the nanoparticles reduces significantly shadowing the substrate and producing a valley in the metal film. For the other two samples, the metal film is 50 nm thick and has only 2 nm or less valley for the 100 s DEEP RIE etched mask, while it is flat on top for the 150 s DEEP RIE etched mask. Figure 3.10 shows the profile for the 50 s and 100 s etched samples. Similar results were obtained for silver nano hole arrays.
Measured data for both silver and gold nanohole arrays are summarized in table 3.4; for the 50 s sample, maximum thickness is reported.

| Etching Time (s) | Au Thickness (nm) | Ag Thickness (nm) | Hole size (nm) |
|---|---|---|---|
| 50 | 44.1 ± 1.2 | 42.3 ± 1.5 | 520 ± 20 |
| 100 | 51 ± 2 | 56 ± 3 | 400 ± 20 |
| 150 | 50 ± 1.2 | 56 ± 2 | 300 ± 20 |

**Table 3.4:** *Structural proprieties (metal thickness and hole size) of synthesized nano hole arrays measured by AFM.*

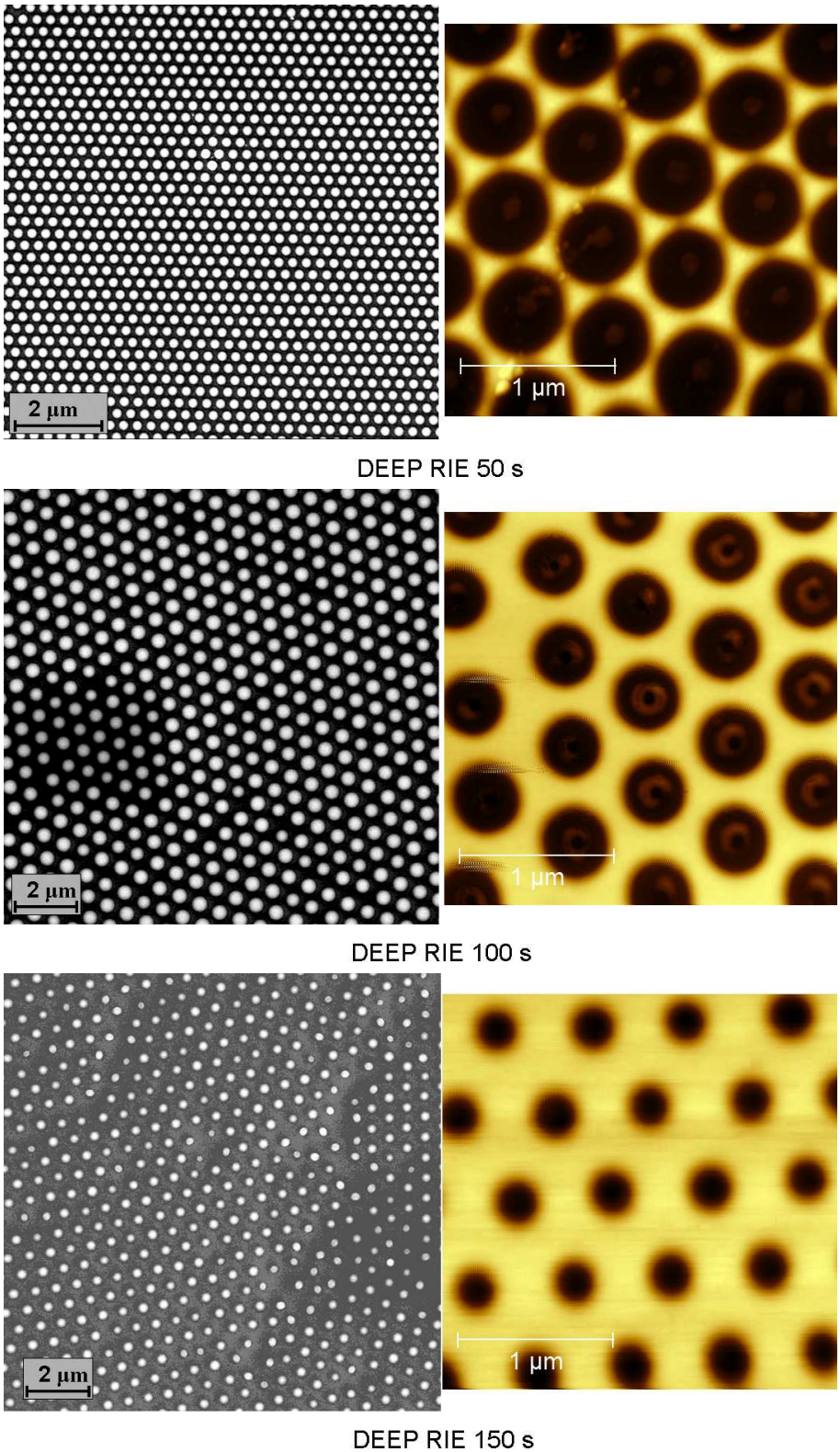


**Figure 3.9:** *Comparison between the PS mask obtained after the etching step (*left column*) and the deposited gold nano hole array (*right column*) for the three etching time.*

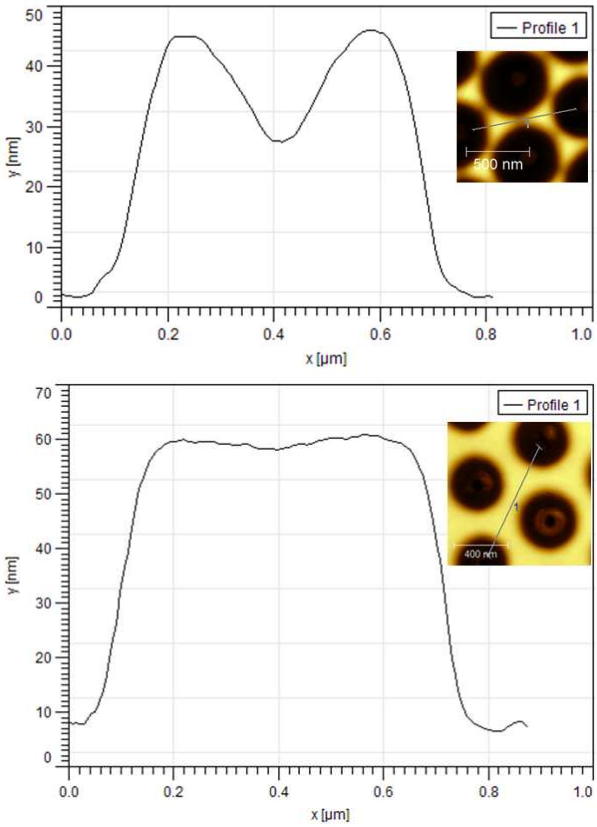


**Figure 3.10:** *AFM measured profiles in the Au layer between two holes for the* 50 *s DEEP RIE etched sample (*Left*) and for the* 100 *s DEEP RIE etched sample (*Right*).*

### 3.2.2 Optical characterization

From AFM measurements summarized in table 3.4 we can calculate the actual area of the hole in the film. Calculations are summarized in table 3.5. The area of the hole decrease with etching time and is in good agreement with the PS nanosphere size. In the last columns of Table 3.5 we calculate the expected transmittance for an opaque film with the respecive filling factor: $FF = 100\% - HoleArea$, as if no plasmonic effect (i.e. EOT) would take place. Filling Factor was calculated modifying equation 2.4

$$FF_{met} = \left(1 - \frac{\Sigma_{sphere}}{\Sigma_{cell}} = \frac{\pi R_{hole}^2}{2\sqrt{3}R_{pattern}^2}\right) \cdot 100 \tag{3.4}$$

where $R_{hole}$ is the hole radius as measured from AFM images and $R_{pattern}$ is the original radius of the nanospheres which determines the hole periodicity on the metal film. Obviously as the size of the hole decreases, and so the FF increases, we expect the transmittance to decrease. The expected transmittance was calculated dividing the extinction coefficient by the filling factor:

$$T = \frac{I}{I_0} = e^{-\alpha \cdot x} \;\Rightarrow\; T_{geometric}(\lambda) = e^{-\ln\left(T_{film}(\lambda)\right) \cdot FF} \tag{3.5}$$

where $T_{geometric}(\lambda)$ is the expected transmittance presuming a pure "geometrical" mechanism so that the transmittance of the nanohole array is equal to a metal film with a macroscopic hole with the same area as the sum of all the small holes, and $T_{film}(\lambda)$ is the transmittance of the continuous metal film at a certain wavelength.

| Etch time (s) | Hole size (nm) | $FF_{met}$ | $T_{Au}$ ($\lambda = 505nm$) | $T_{Ag}$ ($\lambda = 322nm$) | $T_{Au}$ ($\lambda = 1000nm$) | $T_{Ag}$ ($\lambda = 1000nm$) |
|---|---|---|---|---|---|---|
| 50 | 520 ± 20 | 53 % | 35.3 % | 46.0 % | 7.8 % | 1.1 % |
| 100 | 400 ± 20 | 73 % | 23.8 % | 34.7 % | 3.0 % | 0.22 % |
| 150 | 300 ± 20 | 84.3 % | 19.2 % | 29.0 % | 1.8 % | 0.09 % |
| Au Film | 0 | 100 % | 14.0 % | - | 0.82 % | - |
| Ag Film | 0 | 100 % | - | 23.2 % | - | 0.02 % |

**Table 3.5:** *Measured holes in the metal film and expected transmittance T of the NHA based on the pure geometrical filling factor of the metal in the sample, as if no EOT would take place. Au film is 51 nm thick, Ag film is 57 nm thick.*

For both metals we choose to calculate the optical transmittance at two meaningful wavelength: $\lambda_1 = 505\ nm$ and $\lambda_2 = 1000\ nm$ for gold and $\lambda_1 = 322\ nm$ and $\lambda_2 = 1000\ nm$ for silver. The latter wavelength ($\lambda_2 = 1000\ nm$) was chosen because it is the wavelength at an extraordinary behaviour is expected (see equation 3.6 and figure

3.12), while the first wavelength ($\lambda_1 = 505\ nm$ for gold, $\lambda_1 = 322\ nm$ for silver) is, for the two metals, the wavelength at which there is the separation between the interband transitions, which involve the $d$ electrons, and the intraband transitions which involve the $s$ conduction electrons. At these wavelength we do not expect plasmonic contributions to the transmittance (i.e. no extraordinary transmission effect) and so transmittance should scale with the geometrical filling factor. There is a simple approximate model to calculate the maximum of transmittance. For surface plasmon on a 2D lattice the momentum conservation is $k_{SP} = k_x + iG_x + jG_y$, where $k_{SP}$ is the surface plasmon wave vector, $k_x$ is the component of incident light that lies in the plane, $G_x$ and $G_y$ are the reciprocal lattice vectors and $i$, $j$ are integers. At normal incidence the wavelength of the maximum transmittance for a triangular lattice is [57]:

$$\lambda_{max} = a_0 \left[\frac{4}{3}\left(i^2 + ij + j^2\right)\right]^{-\frac{1}{2}} \left(\frac{\epsilon_d \epsilon_m}{\epsilon_d + \epsilon_m}\right)^{\frac{1}{2}} \tag{3.6}$$

Where $a_0$ is the lattice constant (722 nm in our case), $i$ and $j$ are the lattice order (as shown in figure 3.11), $\epsilon_d$ is the dielectric constant of the medium in contact with the metal and $\epsilon_m$ is that of the metal. The linear relationship between $a_0$ and the peak positions also becomes obvious. It should be noted that the metal - air and metal - quartz interfaces

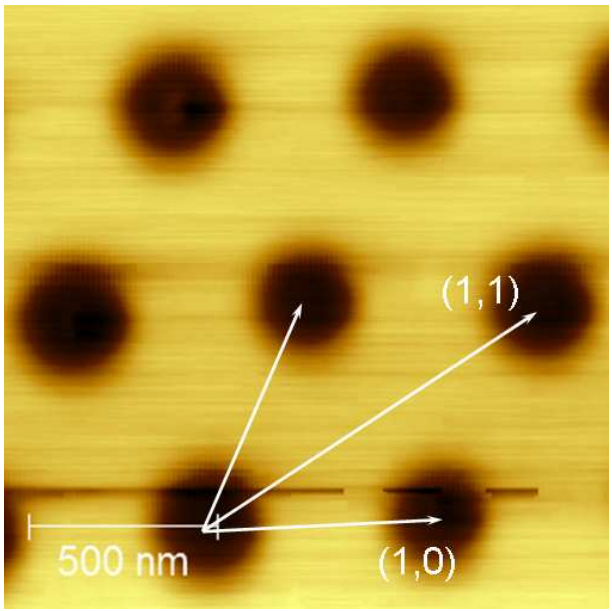


**Figure 3.11:** *Index i,j for the NHA lattice.*

each contribute a set of ($i$, $j$) maxima and minima that are distinguishable because the dielectric constants of air and quartz are significantly different. Both sets are apparent in

the transmission spectra, regardless of which side is illuminated [58]. $\epsilon_d$ and $\epsilon_m$ are both $\lambda$ dependent but as $\epsilon_d$ could be approximated with a constant in the visible region, $\epsilon_m$ is strongly dependent by $\lambda$. Equation 3.6 have to be solved by numerical iterative method, to have a estimation of the transmittance maximum, since $\epsilon_d$ and $\epsilon_m$ are wavelength dependent. We used the bulk dielectric function of gold or silver from [59] to calculate the expected $\lambda_{max}$. Values are summarized in table 3.6 Measured transmittance for gold

| order (i,j) | Ag $\lambda_{max}$ | Au $\lambda_{max}$ |
|---|---|---|
| air (1,0) | 642 nm | 650 nm |
| glass (1,0) | 930 nm | 934 nm |
| glass (1,1) | 568 nm | 595 nm |

**Table 3.6:** *Calculated wavelength at which transmittance maximum should occours*

and silver NHAs, compared to the transmittance of a continuous metal film, are shown in Figure 3.12 and summarized in Table 3.7. Transmittance spectra show an extraordinary

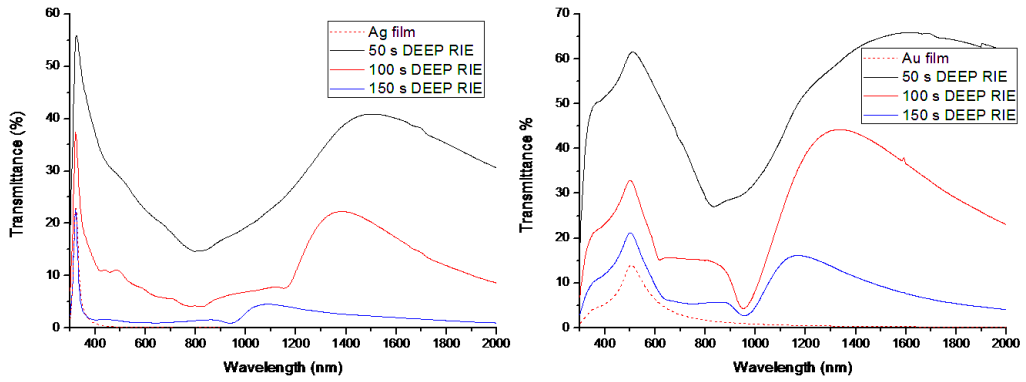


**Figure 3.12:** *Measured optical transmittance for gold and silver nanohole array deposited using different etched mask*

| sample | T($\lambda_1$) | $\lambda_{EOT,max}$ (nm) | T($\lambda_{EOT,max}$) |
|---|---|---|---|
| Ag 50sRIE | 55.8 % | 1501 | 40.9 % |
| Ag 100sRIE | 37.5 % | 1385 | 22.2 % |
| Ag 150sRIE | 23.0 % | 1094 | 4.56 % |
| Au 50sRIE | 61.7 % | 1623 | 65.9 % |
| Au 100sRIE | 32.9 % | 1337 | 44.3 % |
| Au 150sRIE | 21.3 % | 1171 | 16.3 % |

**Table 3.7:** *Measured value from transmittance spectra*

transmission peak for $\lambda > 1000$ nm for all the samples. The position of the peaks for

the various transmittance orders, as described by equation 3.6 should be fixed because it depends only on the lattice parameter ($a_0$), and in our case that correspond to the PS nanospheres size. For the synthesized samples $\lambda_{EOT,max}$ blue-shifts with the increase in etch time, and is red shifted with respect to the value calculated with equation 3.6. This could be due to the approximation that are underlying the model described in equation 3.6. The model describe the optical response for an array of hole in a semi-infinite metal film, so that the thickness of the metal is not taken into account as a variable [57] while in a real sample the peak position is influenced also by the aspect ratio of the holes in the films [56]. Consequently as the etch time becomes higher, the holes aspect ratio grows and the measured results approach the predicted values. Moreover from our AFM measurement (Figure 3.10) we found that the metallic film thickness is not homogeneous, but it exhibits peaks and valleys, especially for the 50 s RIE etched mask. Thickness inhomogeneity could also explain the difference in the low wavelength ($\lambda_1$) transmittance, where EOT should not be a major effect. In fact the measured transmittance is very different with respect to the calculated one, particularly for the 50 s RIE etched samples. A more precise calculation of the optical proprieties would require a more sophisticated modeling based on Finite Difference Time Domain (FDTD) [56] which is in progress.

Anyway this simple model could give some explanation of the features present in the optical spectra. For gold nanohole arrays we could assign the transmission peak at 1200-1300 nm at the (1,0) order glass-metal transmission peak, and the feature that appears as a large shoulder-like peak at about 700-800 nm at the convolution of (1,1) order glass-metal and (1,0) order air-metal peaks. For the same reason, the transmission peak at 1100 - 1300 nm in the silver nanohole array spectra could be ascribed at the (1,0) order glass-metal transmission peak, and the feature that appear as a small large peak at about 900 nm at the convolution of (1,1) order glass-metal and (1,0) order air-metal peaks, while the small feature at 500 nm could be assigned at higher order transmission (1,1) air-metal or (2,0) glass metal.

# Chapter 4

# Surface Patterning

Self assembly is a good method efficiently used also for surface patterning. The deposition of single layers of mono dispersed nanoparticles onto specific substrates is usually achieved through complex physical methods or multistep depositions. Complex nanolithography techniques, such as dip pen nanolitography,[60, 61] allow the dispersion of sub 50 nm particles on flat surfaces. Chemical solution deposition (CSD) techniques are already used to dispatch inorganic nanodomains on substrates, but they provide poor homogeneity. [62] Nanosphere lithography using $SiO_2$ or latex beads is used to prepare metallic nanoparticles arrays with excellent control of the particle shape and size, and the interparticle spacing, as we have demonstrated in the previous chapters.[63] Unfortunately, this method is limited to the fabrication of patterned surfaces with minimum feature sizes of 50 - 80 nm in diameter. At a smaller length scale, ordered monolayers of diblock-copolymer have been used to disperse metallic nanodots on surfaces by impregnation.[64, 65, 66] These latter works involved physical deposition techniques and aimed at distributing discrete nanoislands but not continuous bidimensional networks. Preparing ultrathin films exhibiting continuous bidimensional patterns and well-ordered motifs, such as inversed patterns of nanodot arrays, in the nanoscale range would be highly attractive for nanoengineering of surfaces. Nowadays, one of the more efficient and direct methods available to structure inorganic nanomaterials into organized networks is the surfactant-templating technique first reported by scientists at the Mobil oil company in 1992.[67] Since then, and because of the great number of potential applications associated with their various porous morphologies, this method has been widely studied and adapted to many types of materials. For instance mesoporous films were developed using the evaporation-induced selfassembly [68] technique, related to CSD, that can lead to high-quality materials when critical parameters are adjusted. Eventually, nanocrystalline, ordered mesostructures can be obtained upon careful thermal treatments.[69] Interesting materials such as $TiO_2$[69] and

$Al_2O_3$,[70], were made available in the form of highly ordered, thin mesoporous films.
In this chapter preliminary results will be presented on the use of self assembled monolayer of PS nanospheres to create patterned surfaces. Self assembled monolayers will be used for the synthesis of patterned $TiO_2$ thin film and will be used as mask for ion beam processing and patterning of Si surface.

## 4.1 Patterned titania thin film

The excellent properties of nanostructured titania makes it the material of choice in many applications. Nanostructured titania has been reported to enhance the performance of bio compatible implants [71] and has recently been proposed as a vehicle for gene therapy.[72] In addition to its biological uses, nanostructured titania finds applications in energy conversion,[73] catalysis,[74] and gas sensing.[75, 76] A number of techniques have been developed for synthesizing porous titania, such as screen printing,[73] reactive sputtering,[75] anodizing,[76], emulsion templating,[77] and sol-gel processing.[78] Although the aforementioned techniques are satisfactory for some applications, use of high annealing temperatures (more than 600° C) which precludes use of standard aluminium-based metallization in microelectronic circuits as well as issues of residual carbon incorporation, from organic precursors or binders, and crack formation in titania layers, render these techniques unsuitable for microsystems device applications.
Another promising technique used to synthesize porous thin films of $TiO_2$ is the templated assisted deposition. In template-assisted growth, a template is made by the self-assembly of bacteria,[79] emulsions,[77] colloidal suspensions,[80, 81] or block copolymers.[82] As a next step, the solid material is grown between the template by the use of, e.g., a chemical reaction in which a precipitate is formed. Other methods which can be used to infiltrate a template are filling with a saturated solution of a salt, a melt, a suspension of nanoparticles that settle between the template, sol-gels, or chemical vapor deposition.[80, 81, 83] Finally, the template is removed by etching or calcination and the porous material remains. Until now, this method has been applied to a host of different macroporous materials such as ceramics,[80, 81] carbon,[84] semiconductors, [82] and polymers.[85] It has become widely recognized that macroporous materials are important candidates for photonic crystals. Photonic crystals are three-dimensional periodic dielectric composites with lattice parameters on the order of the wavelength of light. They are especially pursued to achieve photonic band gaps that allow the control of spontaneous emission and the localization of photons. [86]
Here preliminary results on a simple method based on the use of self assembled monolayer

of PS nanospheres as a template to create patterned $TiO_2$ thin films is presented. Surface patterning of $TiO_2$ thin films was performed in collaboration with prof. Martucci's group at Department of Mechanical Engineer, Materials Section at University of Padova.

### 4.1.1 Patterning of $TiO_2$

In our work we use SAM of PS nanoparticles to create nanostructured thin films of $TiO_2$. Our synthesis method is based on the deposition of a self assembled monolayer of PS nanospheres, its infiltration with a $TiO_2$ precursor and the growth of the $TiO_2$ thin film. The $TiO_2$ precursor are layered titanates consisting, in their dried powder form, of nanometric layers with general composition $[Ti_mO_{2m+1}]^{2-}$ stacked in an ordered layered fashion with a cation intercalated between the layers. Layered titanates have been studied [87, 88, 89] and used as precursors for titania with controlled morphology and crystalline structure. These compounds are also very attractive due to optical, photochemical and electronic properties. Furthermore, ion-exchange, intercalation of functional organic molecules and possibility of hybrid assemblies can be applied to titanates materials [90, 91, 92]. Several types of layered titanates with different compositions have been studied. Common titanates incorporate alkaline metal cations to achieve charge neutrality. Their general formula can be written as $A_2Ti_nO_{2n+1}$ where $A$ represents the alkaline metal cation intercalated in the layered structure. The layers are composed of $[Ti_nO_{2n+1}]^{2-}$ polyanions arranged in a stepped fashion as shown below for a sodium trititanate and potassium tetratitanate. These types of structures generally have monoclinic unit cells. A consequence of their structure is the easiness with which it is possible to switch from titanate to anatase. In fact, an in-situ rearrangement is sufficient for phase changing resulting in lower temperatures of anatase formation as compared with other titania precursors. It has been found that acid environment and low temperatures are sufficient to induce phase change, which could be exploited to obtain very interesting morphologies. Layered titanates can undergo ion-exchange processes where the pristine metal cation can be substituted with $H^+$ (proton exchanged), with other metal cation or with organic cations such as protonated amines or ammonium cations. Very interestingly, UV irradiation has been shown to be a useful tool for material modification allowing for densification strategies different from heat treatment [93, 94].

### 4.1.2 Experimental and results

Our synthesis method require three steps: creation of a template by deposition of a self assembled monolayer of PS nanoparticles, infiltration of the monolayer with pre synthesized

layered titanate, UV induced condensation of layered nanoparticles into $TiO_2$, removal of the PS nanoparticles by calcination.
A 50:50 water-isopropanol 5% wt dispersion of PS nanoparticles was prepared and used to create a self assembled monolayer, according to the method described in section 1.4. Monolayer was deposited on fused silica substrate cleaned using a Pirahna solution (1:3 solution of $H_2O_2$ and $H_2SO_4$). Layered titanate nanoparticles were synthesized using a synthesis approach described in reference [95] and is based on acid-base reactions between hydrolysis products of titanium alkoxides and tetramethyammonium hydroxide [88]. The general pathway is summarized in the following reaction scheme:
hydrolysis :

$$mTi(OPr)_4 + (2m+1)H_2O \longrightarrow H_2Ti_mO_{2m+1} + 4mPrOH \tag{4.1}$$

and acid-base reactions :

$$H_2Ti_mO_{2m+1} + 2R_4N^+OH^- \longrightarrow [R_4N^+]_2[Ti_mO^{2-}_{2m+1}] + H_2O \tag{4.2}$$

The first stage is the hydrolysis and condensation of the alkoxide leading to polymeric titanic acid or hydrous titanium oxide. Then, depending on the alkaline strength of the base used, only the first or both of the subsequent acid-base reactions occurs where the hydrous titanium oxide can be deprotonated by the base assuming a negative charge. At this stage a layered structure can be formed. It may be partially exfoliated in the solution state or, in the dried powder state, it can be orderly layered. It was found that the exact type of titanate ($m$ value in the above reactions) changes with the type of used base. It was suggested that a mixture of trititanate, tetratitanate, hexatitanates and so on, is likely to be the product of this type of synthesis. Layered titanates were synthesized from ethylene glycol (EG), Titanium tetraisopropoxide ($Ti(OPri)_4$), water and Tetramethyammonium hydroxide (TMA). EG was heated with an heating mantle in a 50 mL three necked flask fitted with a refluxing condenser at 60°C under vacuum (3 mbar) for 20 minutes. Subsequently the temperature was raised to 110°C after switching to nitrogen flow using conventional Schlenk line setup. $Ti(OPri)_4$ was then injected with a syringe and the solution turned immediately opaque. A second injection consisting in tetramethylammonium hydroxide dissolved in water was quickly performed and an optically clear solution was obtained within few seconds. The synthesis was carried on at 110°C for 8 hours. Finally, the products were collected by centrifugation at 4000 rpm for 4 minutes after inducing flocculation with acetone. The obtained precipitate was washed two times with acetone and two times with methanol and dried under vacuum. Once synthesized

nanoparticles are stored as a dry powder.
A fiber coupled Hamamatsu Lightningcure LC5 UV lamp was used for UV treatments: lamp produces light in the 240 to 400 nm region (with a peak at 365 nm) with a total power of 410 mW/cm$^2$ and produce a circular spot of about 1.5 cm$^2$ at 3 cm from the fiber. Samples were put under the optical fiber keeping the fiber at 3 cm from the sample surface and exposed for the required time. Because of the high intensity of the UV light, to avoid thermal effect the total dose required was divided in short bunches and between them we waited for 5 minutes to let the sample cool down.
Once deposited on the substrate, self assembled nanospheres have been irradiated with UV lamp for a total time of 300 $s$. This preliminary exposure step is required to make the monolayer stable during the infiltration step. PS nanospheres can be mechanically removed from the substrate quietly easily, so to effectively use the monolayer as a template a step to produce a more sticky and stable mask is required. In fact during UV exposure necks among the nanospheres are formed as well as necks between nanospheres and substrate that make the monolayer more adherent to the substrate. Moreover the UV light cause the polystyrene to reticulate making it resistant to solvent swelling and dissolution. The drawback of this stabilization step is that the PS nanospheres cannot be removed by the usual liftoff step used in our previous experiments because of their accreased resistance to organic solvent, so we had to replace the liftoff step with a calcination treatement. After the mask stabilization step, samples are infiltrated with a concentrated solution of titanate. The UV irradiation make this process easier because the ozone that is formed during the exposure, makes the PS surface hydrophilic. 100 mg of titanate powder were dissolved in 1 mL of ultrapure MilliQ water adding a drop (20 $\mu$L) of tetramethylammonium hydroxide under vigorous agitation until a perfectly transparent solution is achieved. This solution was diluted before the infiltration with pure methanol or with a water methanol solution, to obtain the desired final concentration of titanate and in order to have a final water:methanol ratio of 1:1. 50 $\mu$L of the solution is dropped on the sample and spread all over the surface; excess of the solution is removed and sample are let to dry at ambient temperature. Dried infiltrated monolayer were irradiated to degrade the organic base intercalated on the layered structure inducing the phase transition from layered titanate nanoparticles to amorphous $TiO_2$ thin film. The UV exposure was performed by illuminating the sample from the backside, placing the fiber at 3 cm from the surface for a total time of 600 s divided in bunch of 150 s each; 5 minutes were waited between two bunches. Amorphous $TiO_2$ is deposited on the substrate and on the mask during this step. After the irradiation step, the samples are gently washed with deionized water, to eliminate the unreacted titanate. Finally samples were thermal treated at 500°C in air for

30 min to completely remove the organic PS nanospheres and the residual organic base in the deposited amorphous $TiO_2$ that have not be completely degradated by the UV treatment. From XRD study it is shown that during the thermal annealing $TiO_2$ crystallize in the anatase form [95]. In table 4.1 a list of the synthesized sample is presented.

| Label | PS size (nm) | [$TiO_2$] (mg/mL) | UV treatment |
|---|---|---|---|
| Ti-9-0 | 920 | - | 150 · 2 s * |
| Ti-7-25-NoUV | 722 | 25 | - |
| Ti-7-25 | 722 | 25 | 150 · 4 s |
| Ti-3-25 | 330 | 25 | 150 · 4 s |
| Ti-9-50 | 920 | 50 | 150 · 4 s |
| Ti-7-50 | 722 | 50 | 150 · 4 s |

**Table 4.1:** *List of sample analyzed on the present work. * for the mask sample, UV treatment refers to the stabilization step, for the other samples, UV treatment refers to the second UV-exposure.*

### 4.1.3 Structural characterization

The second step of the synthesis protocol, the UV treatment on the mask, was originally performed with a fiber-sample distance of 1 cm. This had some drawbacks on the nanospheres morphology. At this distance the lamp power output is 4500 mW/cm$^2$ (10 times higher) and the spot size is 0.5 cm$^2$. In Figure 4.1 an example of PS nanospheres

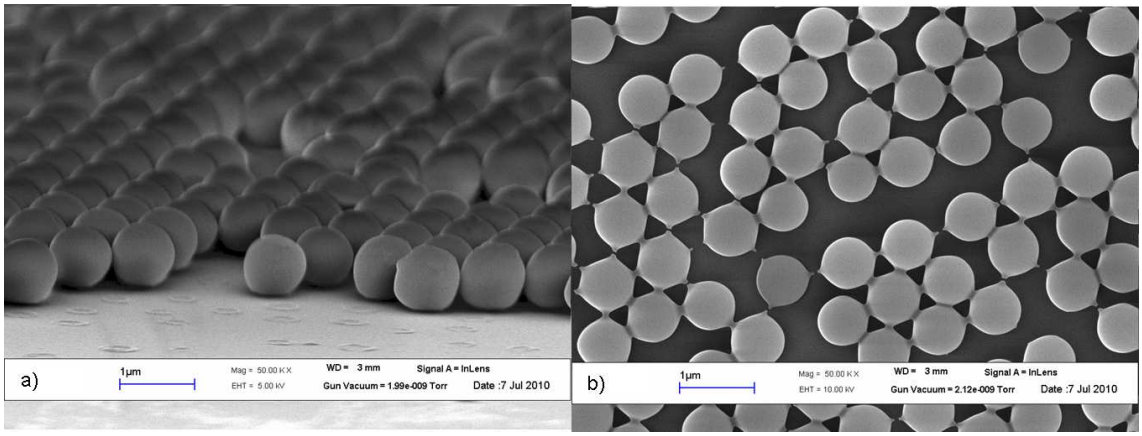


**Figure 4.1:** *SEM image of the Ti-9-0 sample: 920 nm self assembled monolayer irradiated by UV light.*

irradiated is shown. From the cross section image it is visible that thermal effect are not avoided with this treatment because nanoparticles are slightly collapsed, because during the exposure the rise in temperature softened the polystyrene. From the image it is well visible that with this treatment particles sticks to the substrate because a feature is visible where nanoparticles, removed during the cut of the sample, were sitting. From the top view (Figure 4.1 b) a shrinkage of the nanospheres can be observed. Nanospheres were originally 920 nm in size and after the UV exposure become 725 nm in size. This could be caused by the crosslinking of the polymer which is known to cause such an effect. We found that increasing the separation between the fiber and the sample, while keeping the exposure time at 300 s divided in two bunches of 150 s each, would make the self assembled monolayer stable during the infiltration step and would avoid such modification of the mask. All the samples presented in this work have been produced using these parameters for the monolayer stabilization step.

Samples were synthesized using two different concentrations of the titanate nanoparticles solution: 25 mg/mL and 50 mg/mL. To understand the thermal effect on the titanate condensation, a dried infiltrated sample (labeled *Ti-7-25-NoUV*) was annealed at 500°C without preforming the exposure and developing steps. A film of $TiO_2$ is produced with features that show a good replica of the self assembled monolayer. The $TiO_2$ film is thick

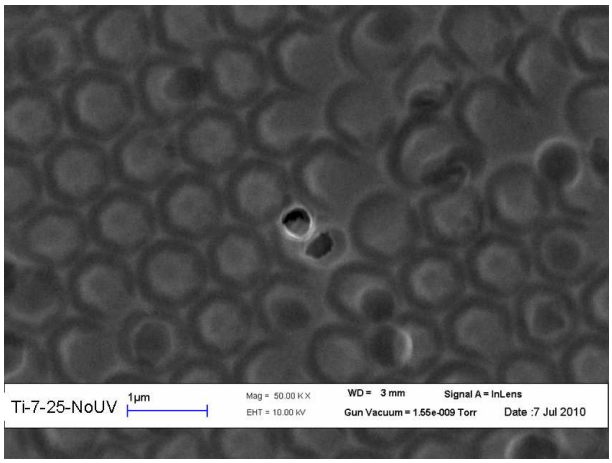


**Figure 4.2:** *SEM image of the Ti-7-25-NoUV sample. The infiltrated 722 nm PS monolayer was calcinated without performing the exposure and developing steps.*

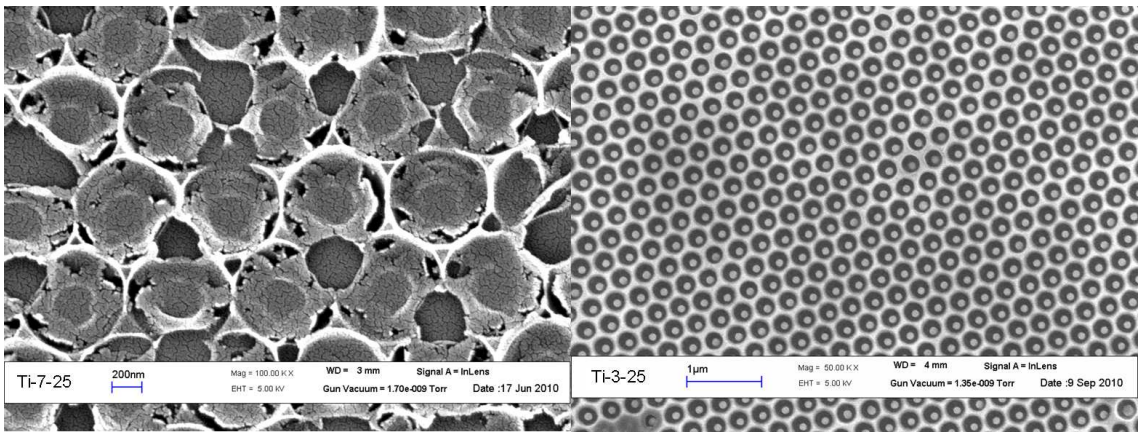


**Figure 4.3:** *SEM image of the Ti-7-25 and Ti-3-25 samples; $TiO_2$ films were deposited using 25mg/mL titanate solution and two different size of nanospheres*

and completely cover the monolayer and a structure similar to an inverse opal is formed.

In the two samples synthesized using the low titanate concentration (25 mg/mL) we can see that the monolayer actually worked as a template for the deposition of the $TiO_2$ film. For the bigger nanospheres the film has many cracks and synthesis parameter should be further optimized. On the other hand the sample synthesized using the smaller nanospheres is a very good replica of the monolayer. An array of nanobowls with a 330 nm periodicity is synthesized over a large area. To be able to synthesize such structure even with bigger nanospheres, a more concentrated solution of titanate was used.

Two $TiO_2$ films, deposited by infiltration of a 722 nm and a 920 nm PS monolayer with the 50 mg/mL titanate solution are presented here. SEM characterization of the two samples

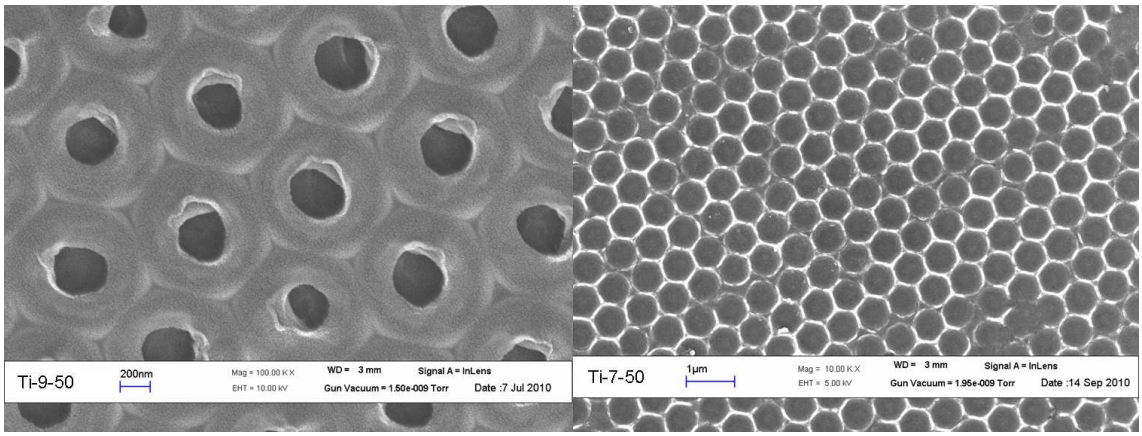


**Figure 4.4:** *SEM image of the Ti-9-50 and Ti-7-50 samples; $TiO_2$ film were deposited using 50 mg/mL titanate solution and two different size of nanospheres*

is shown in Figure 4.4. Pattern of hole in the $TiO_2$ film is visible in the Ti-9-50 sample, while a different structure A structure more similar to an array of nanobowls is obtained for the Ti-7-50 sample (Figure 4.4, right). This structure is similar to the one shown in figure 4.3 synthesized using the lower titanate concentration (25 mg/mL) but with a better replica of the nanoparticle shape and without the cracks that characterized the Ti-7-25 sample. AFM characterization was done on the hole perforated sample Ti-9-50, to measure the thickness of the film and we measured it to be 46 nm thick.

This synthesis method has two drawbacks caused by the UV exposing system: (1) the spot of the fiber is small compared to the size of the deposited monolayer producing an inhomogeneous exposure of the infiltrated sample, and (2) the light beam has a gaussian intensity profile, so that even inside the spot the UV dose is not homogeneous. As an example, sample Ti-7-50 is made of two different structures, as shown in figure 4.5. On the center of the sample the $TiO_2$ film is still a very good replica of the self assembled template, but the structure is more like an inverse opal: a $TiO_2$ film with an hexagonal lattice of holes in it, while on the side of the sample the arrays of bowl is formed. These results demonstrate the possibility to use self assembled monolayer of PS nanospheres to create patterned thin films of $TiO_2$. A more systematic study with a more reproducible setup sill be carried on, to study the possibility to obtain with the same technology two very different structures as the patterned "nanobowl" thin film or the ordered "inverse opal" macroporous structure.

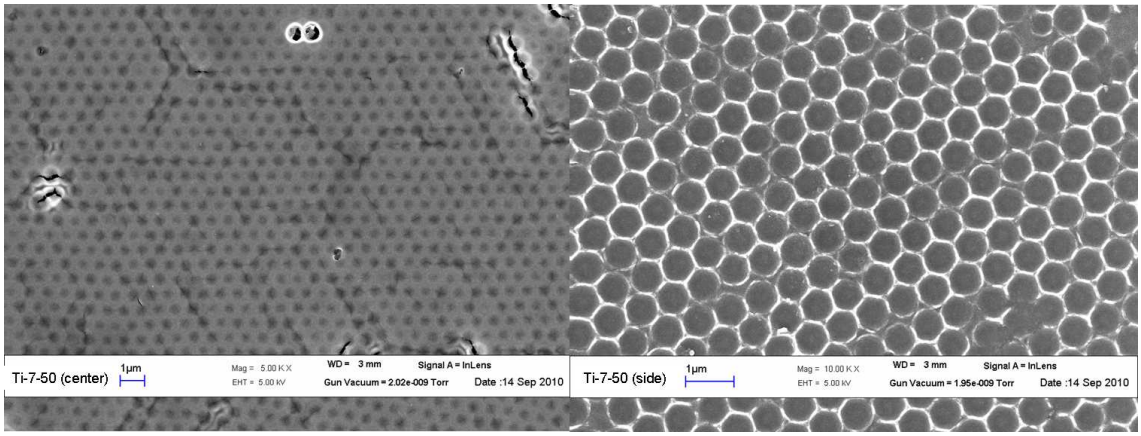


**Figure 4.5:** *SEM images of two different zone of the Ti-7-50 sample. The inhomogeneity of the synthesis method produce different structures on the sample.*

## 4.2 Ion Beam patterning

Along with the creation of plasmonic nanostructures and the use as a template for patterning, thin film self assembly of PS nanoparticles can be used also as a mask for processing and modification of the material underneath. We used the PS self assembled monolayer to mask the energetic ion beam of an ion implanter in order to pattern a Si substrate with nanometric features. Ion beam patterning is important for a great number of applications. Sub-micron scale lithography methods using deep UV, X-ray or electron beams allow further progress to be made in the field of highly integrated circuit hardware manufacturing. One drawback of high-end patterning methods, however, is firstly, the high cost of the equipment. Secondly, a major technical limitation of resist-based lithography is that it cannot be applied to mechanically unstable and bio/chemically functional surface layers. With the advent of nano/micro-electro-mechanical systems (NEMS/MEMS) having higher complexity and integrated functionality, polymer-based electronic devices, microfluidics, and bio-analytical systems, increased flexibility of the surface patterning methods becomes important.
Another important field in which ion beam patterning is of great interest is the creation of arrays of magnetic materials for data storage.[96] It is desirable to create discrete magnetic islands, with each island representing a single magnetic bit. Terris and co worker [96] report an interesting approach to accomplishing the ion-beam modification of a magnetic thin film through a silicon stencil mask. Localized modification of the magnetic coercivity and easy-magnetization axis in Co/Pt multilayers with ion irradiation was recently demonstrated by Chappert et al. with 30 keV $He^+$ ions [97] and by Jamet et al. [98]. At a high enough fluences, $\approx 10^{16}\ ions/cm^2$, the easy axis of magnetization is rotated into the plane of the film. In that work, micrometer-sized features were obtained using a polymer resist mask in contact with the sample. To pattern the magnetic film, the mask was placed on the film and bombarded with ions. Successful magnetic patterning of dots of 100 nm in diameter was confirmed via magnetic force microscope, and was achieved using three different ion species: $He^+$ at 2.3 MeV, $N^+$ at 700 keV, and $Ar^+$ at 1.2 MeV. All of these ions were stopped by the 10 mm silicon membrane and those ions passing through the holes and reaching the sample pass through the magnetic layer and are stopped in the substrate. While the use of such a technique is promising for the fabrication of patterned magnetic recording media, the feature size must clearly be much smaller to be of technological interest. For example, a pattern of 50 nm features spaced by 50 nm corresponds to a data density of 10 $Gb/cm^2$, which is in the regime of industrial interest for patterned media. To produce such small features it is possible to exploit the proprieties of a self assembled monolayer of nanospheres.

We study patterning of Si substrate to understand and demonstrate the possibility of using self assembled monolayer to effectively stop an energetic ion beam producing a pattern the underlying material. We use a self assembled monolayer of PS nanospheres for these preliminary study, but we expect better results by the use of $SiO_2$ nanospheres instead of the polystyrene. Indeed silica has a greater stopping power than PS because of its higher density ($\approx$ 2 g/cm$^3$ for silica synthesized with the Stöber method) and because silica is composed by heavier elements.
Patterning of Si is also a topic of a great interest for the development of high efficiency of solar cells. Silicon surfaces usually reflect more than 30% of the incoming light. To reduce these reflectivity losses surface texturing becomes important in addition to standard anti-reflection coatings (ARC). Different processes with a significant reduction of the reflection depending on geometric dimensions of textured surface structures are well known in the literature (for an overview, see [99]). Appropriate texturing is expected to replace expensive ARC. Laboratory cells with high efficiency, however, require more sophisticated texture schemes based on photolithography. For multicrystalline solar cells, the alkaline etch method allows only limited results because of the statistical grain orientation. RIE by "Natural lithography" is an interesting texturing method based on colloidal particle masking. One clear advantage of this method is the ability to control lateral periodicity of the mask via particle size. A second advantage is that standard etch processes can be used; no modification of industrial etch procedures in order to achieve automasking is required. The third advantage is that the honeycomb texture in known for its high conversion efficiency. [100] On the other hand, compared to maskless texturisation processes additional process steps for mask preparation and removal are required. The problem of consecutive homogeneity is transferred to the preparation of the mask.

### 4.2.1 Experimental and results

Boron doped (100) Silicon wafers where used as substrate. Wafers where cleaned by washing with Pirahna solution (1:3 solution of $H_2O_2$ and $H_2SO_4$) and rinsed with MilliQ water. A self assembled monolayer of PS nanoparticles was prepared and deposited on Si substrate according to the method described in section 1.4. The samples were then implanted with $N_2^+$ ions with a 200 kV high-current implanter (Danfysik 1090). All implants were performed at the Ion implantation facility in the INFN National Laboratory in Legnaro. Implants were made at 100 keV, with a total fluence of $1 \times 10^{16}$ $at/cm^2$; the ion flux was maintained at 0.1 $\mu A/cm^2$
To maximize the interaction between the ion beam and the silicon substrate, $N_2$ was chosen as ion source for the beam, because the $N_2^+$ ion has the same mass of the Si atom.

Simulations of the interaction between the ion beam and the sample were performed using SRIM [101]. Results are presented in Figure 4.6 SRIM calculation shows that $N_2^+$ ion

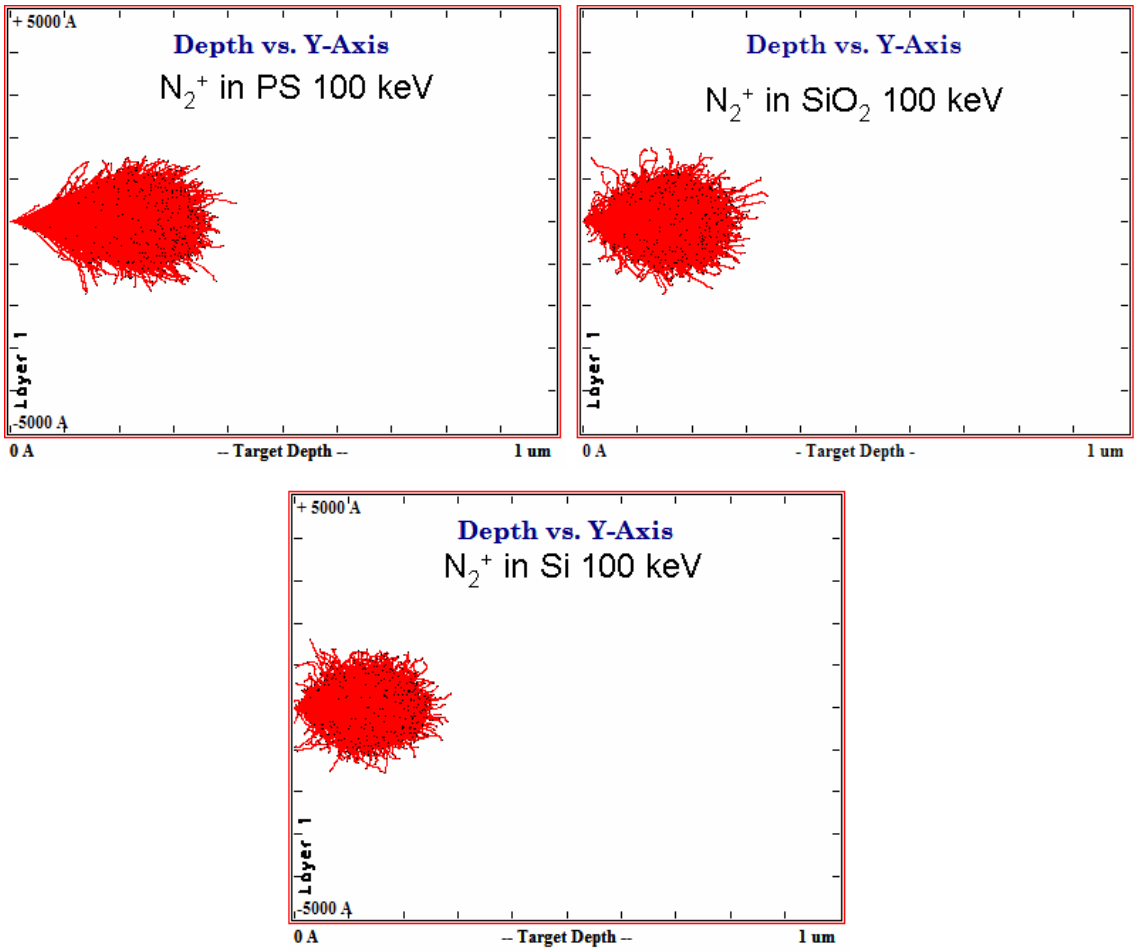


**Figure 4.6:** *SRIM calculation of the interaction between Nitrogen ($N_2^+$) ions and PS and $N_2^+$ ions and Silicon calculated at 100 keV and 150 keV*

can be efficiently stopped by the PS, and so self assembled monolayer could be used to transfer their ordered pattern to the substrate. For the implantations energy investigated (100 keV ) the ion beam has a projected range $Rp = 240$ nm with a $\Delta Rp = 50$ nm. PS nanospheres of 330 nm will not completely stop the ion beam, so it is necessary to use bigger nanospheres and this leads to bigger features in the substrate.
In Figure 4.7 calculation for 330 nm PS nanospheres over a silicon substrate. The beam is almost completely stopped by the nanosphere, and only a very small part could reach the substrate, but this happen only in the center of the sphere, where it is thick; on the sphere's side it is thinner and so a bigger part of the beam will reach the substrate.

This means that at these energies the pattern resolution is limited by the size of the nanospheres. SRIM calculations show also that the use of $SiO_2$ nanospheres instead of the PS nanospheres, should improve the lateral resolution achievable because $SiO_2$ will better stop the ion beam, allowing the use of smaller spheres and so obtaining smaller features.

Because of these calculation we decided to perform our experiments using 722 nm PS self

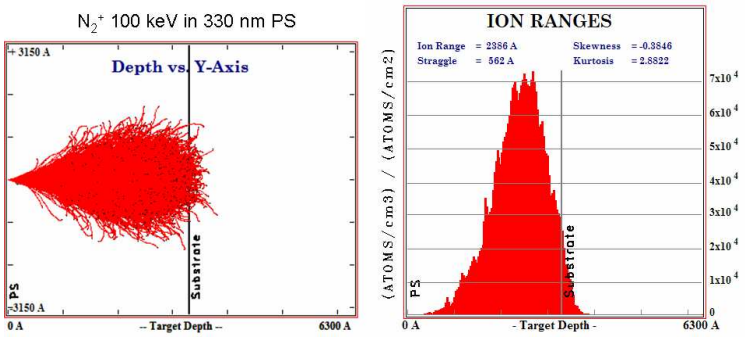


**Figure 4.7:** *SRIM calculation for a 330 nm PS layer on a silicon substrate.*

assembled monolayer. The implantation condition are summarized in table 4.2.

After the ion implantation PS nanospheres are modified by the damage induced by the

| PS size (nm) | Energy (keV) | Etch |
|---|---|---|
| 330 | 100 | - |
| 722 | 100 | - |
| 722 | 100 | BOE (HF-$NH_4F$ 6:1) |
| 722 | 100 | HF - $NHO_3$ - $CH_3COOH$ |

**Table 4.2:** *Synthesis parameters for the sample presented in this chapter*

irradiation. The effects of the damage in the monolayer is somehow similar to the UV irradiation damage: monolayer become resistant to organic solvent, and mask's color is slightly changed (mask appears darker). From SEM images, Figure 4.8, we can see necks among the nanospheres, suggesting that local temperature during the process should be high enough to partially soften or melt the PS. The increased chemical resistance suggest that some other mechanism of radiation induced damage should have occurred causing the PS to reticulate or graphitize (e.g radiolysis of carbon).

To remove the monolayer neither dissolution of the PS, nor scotch tape peeling are feasible: PS has become resistant to organic solvent and nanosphere are stuck on the substrate so that mechanical peeling has become difficult. On the other hand calcination of the sample could induce some modification in the substrate. We choose to lift off the mask by dissolving the native oxide layer which is always present at the silicon surface. Etching

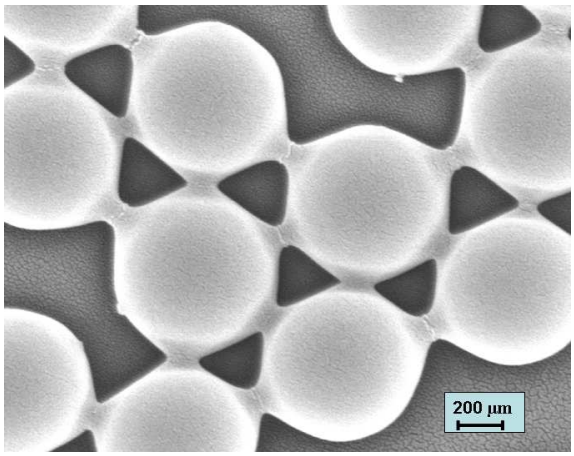


**Figure 4.8:** *SEM image of the PS mask after the implantation step. Necks are formed among the particles*

was performed using a Buffered Oxide Etch solution (BOE). This solution comprises a 6:1 volume ratio of 40% NH4F in water to 49% HF in water, BOE can be further diluited in water, to get a slower etching rate and making processing more controllable. Our samples were etched for 3 minutes in a 1:1 BOE - water solution.

A cross sectional TEM measurement was performed on the 722 nm PS monolayer implanted at 100 keV, to evaluate the effect of implantation in the sample, results are shown in figure 4.9. Having the same mass, the interaction between the $N_2^+$ ion beam and Si atoms of the substrate results in heavy nuclear damage which lead to the amorphization of unmasked Si. TEM images show the presence of a 200 nm thick amorphous region under the exposed silicon surface while under the PS mask the ion beam is completely stopped and silicon remains undamaged. EDX compositional analysis has not revealed the presence of N X-Ray signal in the amorphous-Si region, which means that no chemical reaction occurred. TEM results are in perfect agreement with SRIM calculation showed in figure 4.6.

AFM characterization of the implanted sample was performed and is shown in figure 4.10 From AFM image we can see that the the ion implantation created a good replica of the mask pattern. The sample surface has circular wells where the nanospheres were sitting while the masked area is higher. This phenomenon can also be seen in the TEM image an is related to the local swelling of the silicon induced by the radiation damage[96]. To exploit the difference in the chemical properties of the silicon induced by the radiation damage, samples have been etched to selectively remove the damaged region. We used a mixture of HF:HNO3:CH3COOH in the ratio 1:110:39. This solution will etch very slowly the crystalline silicon while it can etch the amorphous silicon with an etch rate of

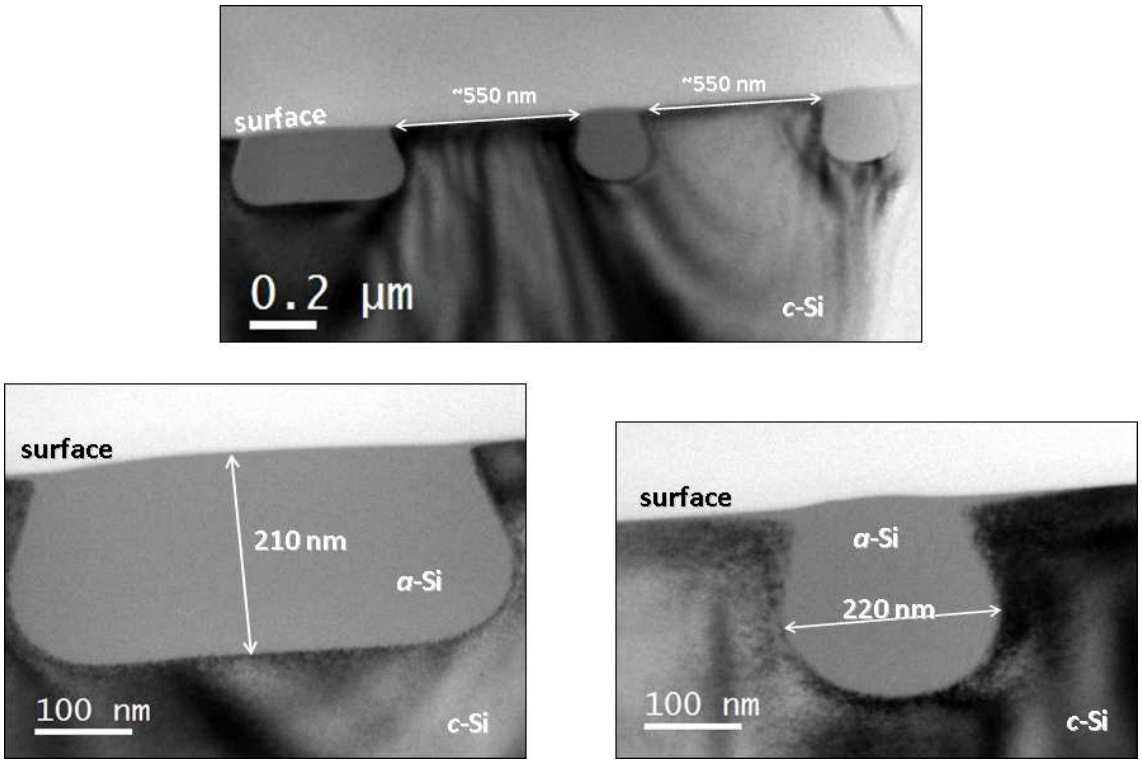


**Figure 4.9:** *Cross section TEM of the 722 nm PS monolayer implanted at 100keV. Amorphous Si is produced on the unmasked Si. EDX compositional analysis has not revealed the presence of N X-Ray signal in the amorphous-Si region.*

60 nm/min.

Etched sample where characterized via AFM and SEM and the measurements are presented in figure 4.11. After mask removal sample were immersed into the etch solution for 5 minutes, to completely remove the amorphized region. Deep etch of the sample is observed. SEM images shows the presence of pyramidal shaped features that we measured (via AFM) to be 140 nm in height. From TEM images we expect to obtain structures with a size of about 200 nm: the difference may be explained by the etch of the crystalline silicon due to the non perfect selectivity of the etch solution.

These preliminary results demonstrate the possibility of using self assembled monolayer of PS spheres as mask for ion beam processing of the substrate. A more systematic study should provide the possibility to better control the etching rate of the sample and so the morphology of the patterned nanostructures.

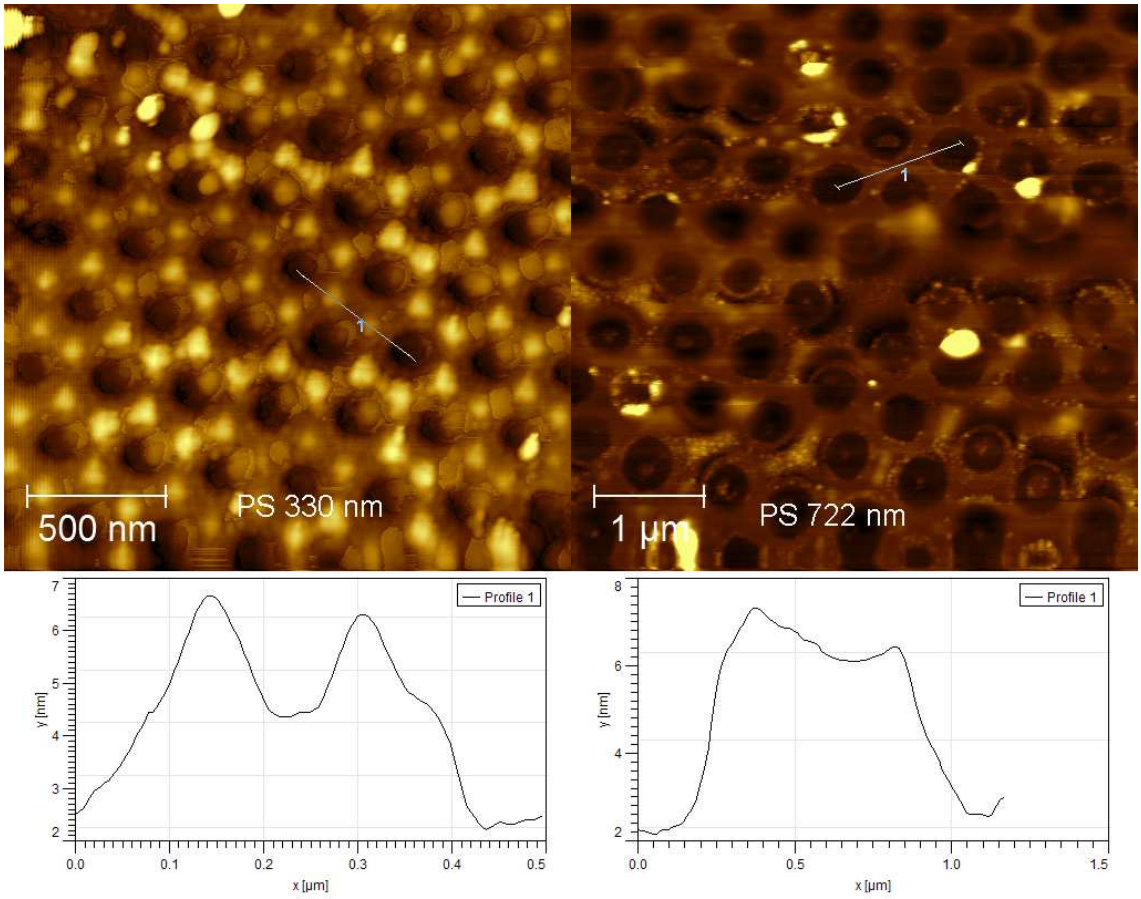


**Figure 4.10:** *AFM measurement of the 722 nm monolayer and the 330 nm monolayer implanted at 100 keV after the lift off process.*

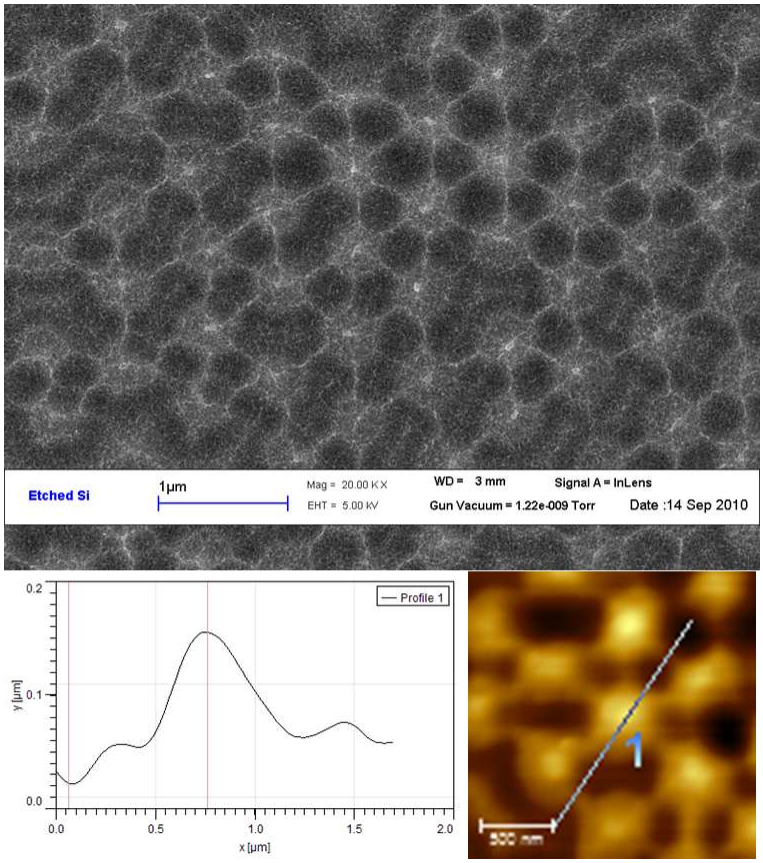


**Figure 4.11:** *Pyramid shaped structures obtained by HF:HNO3:CH3COOH wet etch of irradiated silicon sample.*

# Chapter 5

# Conclusions

In this work we presented the use of self assembled monolayers of PS nanospheres as a low cost, easy to use, flexible nanofabrication tool.
In chapter 1 we presented our method for the self assembly of PS nanospheres and for the deposition of such 2D colloidal crystals of PS nanospheres on several substrate. In the literature, the best results for method of self assembly based on capillary forces usually produce polycrystalline monolayers with iso oriented domains of $100 \times 100 \mu m^2$ in size [27]. Using the modified dip coating system presented in this work, we were able to produce routinely monolayers with such domain size over a large area ($2.5 \times 2.5 cm^2$) with a very good reproducibility from sample to sample. We reported also sample with even bigger domains, up to $750 \times 750 \mu m^2$).
2D colloidal crystals were used as a mask or as a template for producing nanostructures. In chapter 2 we used self assembled monolayer for nanosphere lithography (NSL) [23]. We produced arrays of metallic nanoparticles for plasmonics application. Gold and silver nanoparticles with size from $36nm$ to $215nm$ were produced by sputtering metal through the pore in the self assembled mask. NSL has the main advantage to allow a very good control on deposited nanoparticle's size and shape, giving a very good control on nanoparticle's plasmonic proprieties. We also reported some methods, based on the modification of the mask or on the modification of deposited nanoparticles, to finely tune the plasmonic proprieties (i.e. LSPR peak position) of metallic nanoparticles, giving the possibility to tailor them on the desired application.
Plasmonic nanoparticles were used for molecular sensing and SERS spectroscopy. Molecular sensing is based on the shift of the LSRP peak induced by the change in the nanoenvironment dielectric proprieties. We presented preliminary results on the use of nanoparticles arrays functionalized with a thiolated PEG. This will be the substrate upon which an innovative molecular sensor will be realized in the framework of the PLATFORMS project.

Arrays of plasmonic nanoparticles were used for SERS spectroscopy and we reported very interesting enhancement factors of the Raman signal induced by the surface enhancement of $\approx 10^5$. Finally we reported a simple method to measure the temperature reached by silver nanoparticles under illumination by an Ar laser resonant with the LSPR. Exploiting the temperature-dependent photoluminescence properties of an erbium complex (EuTTA), we measured a rise in temperature of 23°C under plasmonic excitation.
In chapter 3 we reported a method to modify the self assembled monolayer to produce another class of plasmonic nanostructures: the nano hole array (NHA). The interest in NHA arise from the Extraordinary Optical Transmission discovered by Ebbesen [50]. We produced NHA by a controlled etching of the PS nanospheres prior to the metal deposition. We used a plasma based dry etching (RIE and DEEP RIE) to reduce the nanospheres's size of the colloidal crystal without affecting their periodicity and the order created by self assembly. We demonstrated to the hole diameter in the metal film by adjusting the etching time, while changing the periodicity of the 2D hole lattice by varying the NS size.
In chapter 4 we reported different uses of such 2D colloidal crystals. We used them as a template to create nano-patterned $TiO_2$ thin films. We were able to implement a simple, cheap and flexible method to create different kinds of nanostructured titania thin films. By infiltration of the monolayer with a $TiO_2$ precursor and UV exposure of the sample, different nanostructured $TiO_2$ thin films could be obtained: from macroporous films with a ordered porosity (with a structure similar to the "inverse opal") to patterned $TiO_2$ surfaces with a ordered nanobowl array structure.
Moreover we demonstrated the possibility of using self assembled monolayers as a mask for ion beam processing. 2D colloidal crystal of PS nanoparticles have been efficiently used to mask the ion beam resulting in nanostructured implantation 2D pattern. Preliminary experiment were done using a Si substrate that was later etched exploiting the difference in chemical proprieties induced by the implantation process.

In conclusion we showed that self assembled monolayers are a cheap, bench top, flexible tool for nanofabrication. They can be used to synthesize a variety of nanostructures: from deposition of nanoparticles with an excellent control on nanoparticles's size and shape, to the preparation of patterned surfaces of both metal and oxide, to the use coupled with standard IC process such as ion implantation. Application of such nanostructures are found in many fields: plasmonics [23, 56, 63], data storage [27, 97, 102], catalysis [74, 80], biochemistry [54, 103, 104], solar cells [73, 100, 105] to mention a few.

# Bibliography


[1] Douglas Philp and J. Fraser Stoddart. Self-Assembly in natural and unnatural systems. *Angewandte Chemie International Edition in English*, 35(11):1154–1196, 1996. 7

[2] J. Rodrguez-Hernndez, F. Chcot, Y. Gnanou, and S. Lecommandoux. Toward [']smart' nano-objects by self-assembly of block copolymers in solution. *Progress in Polymer Science*, 30(7):691–724, July 2005. 7

[3] Philippe Cordier, Francois Tournilhac, Corinne Soulie-Ziakovic, and Ludwik Leibler. Self-healing and thermoreversible rubber from supramolecular assembly. *Nature*, 451(7181):977–980, February 2008. 7

[4] Paul W. K. Rothemund. Folding DNA to create nanoscale shapes and patterns. *Nature*, 440(7082):297–302, March 2006. 7

[5] Chengde Mao, Thomas H. LaBean, John H. Reif, and Nadrian C. Seeman. Logical computation using algorithmic self-assembly of DNA triple-crossover molecules. *Nature*, 407(6803):493–496, 2000. 7

[6] GM Whitesides and B Grzybowski. Self-assembly at all scales. *SCIENCE*, 295(5564):2418–2421, March 2002. 7

[7] C. Jeffrey Brinker, Yunfeng Lu, Alan Sellinger, and Hongyou Fan. Evaporation-Induced Self-Assembly: nanostructures made easy. *Advanced Materials*, 11(7):579–585, 1999. 9

[8] Peng Jiang and Michael J. McFarland. Large-Scale fabrication of Wafer-Size colloidal crystals, macroporous polymers and nanocomposites by Spin-Coating. *Journal of the American Chemical Society*, 126(42):13778–13786, October 2004. 9, 11, 12, 14

[9] P. Pieranski. Colloidal crystals. *Contemporary Physics*, 24:25, January 1983. 9

[10] PN PUSEY and W VANMEGEN. PHASE-BEHAVIOR OF CONCENTRATED SUSPENSIONS OF NEARLY HARD COLLOIDAL SPHERES. *NATURE*, 320(6060):340–342, March 1986. 9

[11] KE DAVIS, WB RUSSEL, and WJ GLANTSCHNIG. DISORDER-TO-ORDER TRANSITION IN SETTLING SUSPENSIONS OF COLLOIDAL SILICA - X-RAY MEASUREMENTS. *SCIENCE*, 245(4917):507–510, August 1989. 9

[12] P Jiang, JF Bertone, KS Hwang, and VL Colvin. Single-crystal colloidal multilayers of controlled thickness. *CHEMISTRY OF MATERIALS*, 11(8):2132–2140, August 1999. 9, 10

[13] Yurii A. Vlasov, Xiang-Zheng Bo, James C. Sturm, and David J. Norris. On-chip natural assembly of silicon photonic bandgap crystals. *Nature*, 414(6861):289–293, November 2001. 10

[14] H. W. Deckman and J. H. Dunsmuir. Natural lithography. *Applied Physics Letters*, 41(4):377–379, 1982. 11, 27, 66

[15] G. A. Ozin and S. M. Yang. The race for the photonic chip: Colloidal crystal assembly in silicon wafers. *Advanced Functional Materials*, 11(2):95–104, 2001. 11

[16] SH Sun, CB Murray, D Weller, L Folks, and A Moser. Monodisperse FePt nanoparticles and ferromagnetic FePt nanocrystal superlattices. *SCIENCE*, 287(5460):1989–1992, March 2000. 13

[17] B. J. Ackerson and N. A. Clark. Shear-induced partial translational ordering of a colloidal solid. *Physical Review A*, 30(2):906, 1984. 13

[18] B J Ackerson. Shear induced order of hard sphere suspensions. *Journal of Physics: Condensed Matter*, 2(S):SA389–SA392, 1990. 13

[19] M. D. Haw, W. C. K. Poon, and P. N. Pusey. Direct observation of oscillatory-shear-induced order in colloidal suspensions. *Physical Review E*, 57(6):6859, June 1998. 13

[20] ND DENKOV, OD VELEV, PA KRALCHEVSKY, IB IVANOV, H YOSHIMURA, and K NAGAYAMA. MECHANISM OF FORMATION OF 2-DIMENSIONAL CRYSTALS FROM LATEX-PARTICLES ON SUBSTRATES. *LANGMUIR*, 8(12):3183–3190, December 1992. 16, 17, 19

[21] P. Kralchevsky, V. Paunov, I. Ivanov, K. Nagayama, KRALCHEVSKY, PAUNOV, IVANOV, and NAGAYAMA. CAPILLARY MENISCUS INTERACTION BETWEEN COLLOIDAL PARTICLES ATTACHED TO a LIQUID-FLUID INTERFACE. *Journal of colloid and interface science*, 151(1):79–94, 1992. 16, 19, 20

[22] ND DENKOV, OD VELEV, PA KRALCHEVSKY, IB IVANOV, H YOSHIMURA, and K NAGAYAMA. 2-DIMENSIONAL CRYSTALLIZATION. *NATURE*, 361(6407):26–26, January 1993. 16

[23] John C. Hulteen and Richard P. Van Duyne. Nanosphere lithography: A materials general fabrication process for periodic particle array surfaces, 1995. 21, 22, 27, 66, 101, 102

[24] Christy L. Haynes, Adam D. McFarland, Matthew T. Smith, John C. Hulteen, and Richard P. Van Duyne. Angle-Resolved nanosphere lithography: manipulation of nanoparticle size, shape, and interparticle spacing. *The Journal of Physical Chemistry B*, 106(8):1898–1902, February 2002. 22

[25] A Kosiorek, W Kandulski, H Glaczynska, and M Giersig. Fabrication of nanoscale rings, dots, and rods by combining shadow nanosphere lithography and annealed polystyrene nanosphere masks. *SMALL*, 1(4):439–444, April 2005. 22, 48

[26] A. Kosiorek, W. Kandulski, P. Chudzinski, K. Kempa, and M. Giersig. Shadow nanosphere lithography: simulation and experiment. *Nano Letters*, 4(7):1359–1363, July 2004. 22

[27] J. Rybczynski, U. Ebels, and M. Giersig. Large-scale, 2D arrays of magnetic nanoparticles. *Colloids and Surfaces A: Physicochemical and Engineering Aspects*, 219(1-3):1–6, June 2003. 22, 24, 101, 102

[28] Heather A. Bullen and Simon J. Garrett. TiO2 nanoparticle arrays prepared using a nanosphere lithography technique. *Nano Letters*, 2(7):739–745, July 2002. 22

[29] yue Wang, Shubo Han, Alejandro Briseno, Raymond Sanedrin, and Feimeng Zhou. A modified nanosphere lithography for the fabrication of aminosilane/polystyrene nanoring arrays and the subsequent attachment of gold or DNA-capped gold nanoparticles. *Journal Cover:J. Mater. Chem., 2004, 14, 3488-3494 Journal of Materials Chemistry*, 24:3488–3494, 2004. 22

[30] Yuguang Cai and Benjamin M. Ocko. Large-Scale fabrication of protein nanoarrays based on nanosphere lithography. *Langmuir*, 21(20):9274–9279, 2005. 22

[31] F. Lenzmann, K. Li, A. H. Kitai, and H. D. H. Stover. Thin-film micropatterning using polymer microspheres. *Chemistry of Materials*, 6(2):156–159, February 1994. 22

[32] Werner Stber, Arthur Fink, and Ernst Bohn. Controlled growth of monodisperse silica spheres in the micron size range. *Journal of Colloid and Interface Science*, 26(1):62–69, January 1968. 23

[33] G.H. Bogush, M.A. Tracy, and C.F. Zukoski IV. Preparation of monodisperse silica particles: Control of size and mass fraction. *Journal of Non-Crystalline Solids*, 104(1):95–106, August 1988. 23

[34] W Knoll. Interfaces and thin films as seen by bound electromagnetic waves. *ANNUAL REVIEW OF PHYSICAL CHEMISTRY*, 49:569–638, 1998. 27

[35] T Jensen, L Kelly, A Lazarides, and GC Schatz. Electrodynamics of noble metal nanoparticles and nanoparticle clusters. *JOURNAL OF CLUSTER SCIENCE*, 10(2):295–317, June 1999. 27

[36] Sonia Kumar, Nathan Harrison, Rebecca Richards-Kortum, and Konstantin Sokolov. Plasmonic nanosensors for imaging intracellular biomarkers in live cells. *Nano Letters*, 7(5):1338–1343, May 2007. 28

[37] Andr M. Gobin, Min Ho Lee, Naomi J. Halas, William D. James, Rebekah A. Drezek, and Jennifer L. West. Near-Infrared resonant nanoshells for combined optical imaging and photothermal cancer therapy. *Nano Letters*, 7(7):1929–1934, July 2007. 28

[38] ME Stewart, CR Anderton, LB Thompson, J Maria, SK Gray, JA Rogers, and RG Nuzzo. Nanostructured plasmonic sensors. *CHEMICAL REVIEWS*, 108(2):494–521, February 2008. 28

[39] JP Camden, JA Dieringer, J Zhao, and RP Van Duyne. Controlled plasmonic nanostructures for Surface-Enhanced spectroscopy and sensing. *ACCOUNTS OF CHEMICAL RESEARCH*, 41(12):1653–1661, December 2008. 28

[40] O Stranik, R Nooney, C McDonagh, and BD MacCraith. Optimization of nanoparticle size for plasmonic enhancement of fluorescence. *PLASMONICS*, 2(1):15–22, March 2007. 28

[41] Gustav Mie. Beitrge zur optik trber medien, speziell kolloidaler metallsungen. *Annalen der Physik*, 330(3):377–445, 1908. 30

[42] H. A. Lorentz. *Theory of Electrons*. Teubner, Leipzig, 1909. 42

[43] K. Lance Kelly, Eduardo Coronado, Lin Lin Zhao, and George C. Schatz. The optical properties of metal nanoparticles: the influence of size, shape, and dielectric environment. *The Journal of Physical Chemistry B*, 107(3):668–677, January 2003. 44

[44] CL Haynes and RP Van Duyne. Plasmon-sampled surface-enhanced raman excitation spectroscopy. *JOURNAL OF PHYSICAL CHEMISTRY B*, 107(30):7426–7433, July 2003. 46, 51

[45] Mariano Bossi, Jonas Folling, Vladimir N. Belov, Vadim P. Boyarskiy, Rebecca Medda, Alexander Egner, Christian Eggeling, Andreas Schonle, and Stefan W. Hell. Multicolor Far-Field fluorescence nanoscopy through isolated detection of distinct molecular species. *Nano Letters*, July 2008. 46

[46] Mohammad Kamal Hossain, Toru Shimada, Masahiro Kitajima, Kohei Imura, and Hiromi Okamoto. Near-Field raman imaging and electromagnetic field confinement in the Self-Assembled monolayer array of gold nanoparticles. *Langmuir*, July 2008. 46

[47] XY Zhang, AV Whitney, J Zhao, EM Hicks, and RP Van Duyne. Advances in contemporary nanosphere lithographic techniques. *JOURNAL OF NANOSCIENCE AND NANOTECHNOLOGY*, 6(7):1920–1934, July 2006. 55

[48] Bharathi Bai J. Basu and N. Vasantharajan. Temperature dependence of the luminescence lifetime of a europium complex immobilized in different polymer matrices. *Journal of Luminescence*, 128(10):1701–1708, October 2008. 61

[49] D. L. Barton and P. Tangyunyong. Fluorescent microthermal imaging – theory and methodology for achieving high thermal resolution images. *Microelectronic Engineering*, 31(1-4):271–279, February 1996. 62

[50] T. W. Ebbesen, H. J. Lezec, H. F. Ghaemi, T. Thio, and P. A. Wolff. Extraordinary optical transmission through sub-wavelength hole arrays. *Nature*, 391(6668):667–669, February 1998. 65, 102

[51] Hanwei Gao, Joel Henzie, and Teri W. Odom. Direct evidence for surface Plasmon-Mediated enhanced light transmission through metallic nanohole arrays. *Nano Letters*, 6(9):2104–2108, 2006. 65

[52] Erwin Altewischer, Cyriaque Genet, Martin P. van Exter, J. P. Woerdman, Paul F. A. Alkemade, Arjan van Zuuk, and EmileW. J. M. van der Drift. Polarization tomography of metallic nanohole arrays. *Optics Letters*, 30(1):90–92, January 2005. 65

[53] Eun-Soo Kwak, Joel Henzie, Shih-Hui Chang, Stephen K. Gray, George C. Schatz, and Teri W. Odom. Surface plasmon standing waves in Large-Area subwavelength hole arrays. *Nano Letters*, 5(10):1963–1967, October 2005. 65

[54] Jing Chen, Jian Shi, Dominique Decanini, Edmond Cambril, Yong Chen, and Anne-Marie Haghiri-Gosnet. Gold nanohole arrays for biochemical sensing fabricated by soft UV nanoimprint lithography. *Microelectronic Engineering*, 86(4-6):632–635, 2009. 66, 102

[55] W. A. Murray, S. Astilean, and W. L. Barnes. Transition from localized surface plasmon resonance to extended surface plasmon-polariton as metallic nanoparticles merge to form a periodic hole array. *Physical Review B*, 69(16):165407, April 2004. Copyright (C) 2008 The American Physical Society; Please report any problems to prola@aps.org. 66

[56] Si Hoon Lee, Kyle C. Bantz, Nathan C. Lindquist, Sang-Hyun Oh, and Christy L. Haynes. Self-Assembled plasmonic nanohole arrays. *Langmuir*, 25(23):13685–13693, December 2009. 66, 82, 102

[57] Tineke Thio, H. F. Ghaemi, H. J. Lezec, P. A. Wolff, and T. W. Ebbesen. Surface-plasmon-enhanced transmission through hole arrays in cr films. *Journal of the Optical Society of America B*, 16(10):1743–1748, October 1999. 80, 82

[58] H. F. Ghaemi, Tineke Thio, D. E. Grupp, T. W. Ebbesen, and H. J. Lezec. Surface plasmons enhance optical transmission through subwavelength holes. *Physical Review B*, 58(11):6779, 1998. 81

[59] Edward D. Palik. *Handbook of Optical Constants of Solids*. Academic Press, 1 edition, October 1997. 81

[60] Richard D. Piner, Jin Zhu, Feng Xu, Seunghun Hong, and Chad A. Mirkin. "Dip-Pen" nanolithography. *Science*, 283(5402):661 –663, January 1999. 83

[61] Seunghun Hong, Jin Zhu, and Chad A. Mirkin. Multiple ink nanolithography: Toward a Multiple-Pen Nano-Plotter. *Science*, 286(5439):523 –525, October 1999. 83

[62] I. Szafraniak, C. Harnagea, R. Scholz, S. Bhattacharyya, D. Hesse, and M. Alexe. Ferroelectric epitaxial nanocrystals obtained by a self-patterning method. *Applied Physics Letters*, 83(11):2211, 2003. 83

[63] A. J Haes, C. L Haynes, A. D McFarland, G. C Schatz, R. P Van Duyne, and S. Zou. Plasmonic materials. *MRS bulletin*, 30:369, 2005. 83, 102

[64] Martin Mller, Joachim P. Spatz, and Arno Roescher. Gold nanoparticles in micellar poly(styrene)-b-poly(ethylene oxide) filmssize and interparticle distance control in monoparticulate films. *Advanced Materials*, 8(4):337–340, 1996. 83

[65] Roman Glass, Martin M ller, and Joachim P Spatz. Block copolymer micelle nanolithography. *Nanotechnology*, 14(10):1153–1160, 2003. 83

[66] Yao Lin, Alexander Boker, Jinbo He, Kevin Sill, Hongqi Xiang, Clarissa Abetz, Xuefa Li, Jin Wang, Todd Emrick, Su Long, Qian Wang, Anna Balazs, and Thomas P. Russell. Self-directed self-assembly of nanoparticle/copolymer mixtures. *Nature*, 434(7029):55–59, March 2005. 83

[67] C. T. Kresge, M. E. Leonowicz, W. J. Roth, J. C. Vartuli, and J. S. Beck. Ordered mesoporous molecular sieves synthesized by a liquid-crystal template mechanism. *Nature*, 359:710–712, October 1992. 83

[68] Yunfeng Lu, Hongyou Fan, Aaron Stump, Timothy L. Ward, Thomas Rieker, and C. Jeffrey Brinker. Aerosol-assisted self-assembly of mesostructured spherical nanoparticles. *Nature*, 398(6724):223–226, March 1999. 83

[69] David Grosso, Galo J. de A. A. Soler-Illia, Eduardo. L. Crepaldi, Florence Cagnol, Christophe Sinturel, Alexis Bourgeois, Aline Brunet-Bruneau, Heinz Amenitsch, Pierre A. Albouy, and Clment Sanchez. Highly porous TiO2 anatase optical thin films with cubic mesostructure stabilized at 700 C. *Chemistry of Materials*, 15(24):4562–4570, December 2003. 83

[70] Monika Kuemmel, David Grosso, Cdric Boissire, Bernd Smarsly, Torsten Brezesinski, Pierre A. Albouy, Heinz Amenitsch, and Clement Sanchez. Thermally stable nanocrystalline -Alumina layers with highly ordered 3D mesoporosity. *Angewandte Chemie International Edition*, 44(29):4589–4592, 2005. 84

[71] Thomas J. Webster, Richard W. Siegel, and Rena Bizios. Osteoblast adhesion on nanophase ceramics. *Biomaterials*, 20(13):1221–1227, July 1999. 84

[72] Tatjana Paunesku, Tijana Rajh, Gary Wiederrecht, Jorg Maser, Stefan Vogt, Natasa Stojicevic, Miroslava Protic, Barry Lai, Jeremy Oryhon, Marion Thurnauer, and Gayle Woloschak. Biology of TiO2-oligonucleotide nanocomposites. *Nat Mater*, 2(5):343–346, May 2003. 84

[73] Michael Gratzel. Photoelectrochemical cells. *Nature*, 414(6861):338–344, November 2001. 84, 102

[74] M. P. Harold, C. Lee, A. J. Burggraaf, K. Keizer, V. T. Zaspalis, and R. S. de Lange. Catalysis with inorganic membranes. *Mrs Bulletin*, 19(4):3439, 1994. 84, 102

[75] Giorgio Sberveglieri, Laura E. Depero, Paolo Nelli, Cesare Perego, Luigi Sangaletti, Matteo Ferroni, Vincenzo Guidi, and Giuliano Martinelli. A novel method for the preparation of nanosized tio2 thin films. *Advanced Materials*, 8(4):334–337, 1996. 84

[76] O.K. Varghese, D. Gong, M. Paulose, K.G. Ong, E.C. Dickey, and C.A. Grimes. Extreme changes in the electrical resistance of titania nanotubes with hydrogen exposure. *Advanced Materials*, 15(78):624–627, 2003. 84

[77] A. Imhof and D. J. Pine. Ordered macroporous materials by emulsion templating. *Nature*, 389(6654):948–951, October 1997. 84

[78] Koichi Kajihara, Kazuki Nakanishi, Katsuhisa Tanaka, Kazuyuki Hirao, and Naohiro Soga. Preparation of macroporous titania films by a Sol-Gel Dip-Coating method from the system containing poly(ethylene glycol). *Journal of the American Ceramic Society*, 81(10):2670–2676, 2005. 84

[79] Sean A. Davis, Sandra L. Burkett, Neil H. Mendelson, and Stephen Mann. Bacterial templating of ordered macrostructures in silica and silica-surfactant mesophases. *Nature*, 385(6615):420–423, January 1997. 84

[80] Brian T. Holland, Christopher F. Blanford, and Andreas Stein. Synthesis of macroporous minerals with highly ordered Three-Dimensional arrays of spheroidal voids. *Science*, 281(5376):538 –540, July 1998. 84, 102

[81] Judith E. G. J. Wijnhoven and Willem L. Vos. Preparation of photonic crystals made of air spheres in titania. *Science*, 281(5378):802 –804, 1998. 84

[82] Paul V. Braun and Pierre Wiltzius. Microporous materials: Electrochemically grown photonic crystals. *Nature*, 402(6762):603–604, December 1999. 84

[83] D. J. Norris and Yu. A. Vlasov. Chemical approaches to Three-Dimensional semiconductor photonic crystals. *Advanced Materials*, 13(6):371–376, 2001. 84

[84] Anvar A. Zakhidov, Ray H. Baughman, Zafar Iqbal, Changxing Cui, Ilyas Khayrullin, Socrates O. Dantas, Jordi Marti, and Victor G. Ralchenko. Carbon structures with Three-Dimensional periodicity at optical wavelengths. *Science*, 282(5390):897 –901, October 1998. 84

[85] Samson A. Jenekhe and X. Linda Chen. Self-Assembly of ordered microporous materials from Rod-Coil block copolymers. *Science*, 283(5400):372 –375, January 1999. 84

[86] Eli Yablonovitch. Inhibited spontaneous emission in Solid-State physics and electronics. *Physical Review Letters*, 58(20):2059, May 1987. 84

[87] Thomas P. Feist and Peter K. Davies. The soft chemical synthesis of TiO2 (B) from layered titanates. *Journal of Solid State Chemistry*, 101(2):275–295, December 1992. 85

[88] Tomokazu Ohya, Aki Nakayama, Takayuki Ban, Yutaka Ohya, and Yasutaka Takahashi. Synthesis and characterization of halogen-free, transparent, aqueous colloidal titanate solutions from titanium alkoxide. *Chemistry of Materials*, 14(7):3082–3089, July 2002. 85, 86

[89] Tao Gao, Helmer Fjellvag, and Poul Norby. Defect chemistry of a Zinc-Doped lepidocrocite titanate CsxTi2x/2Znx/2O4 (x = 0.7) and its protonic form. *Chemistry of Materials*, 21(15):3503–3513, 2009. 85

[90] Alexander Riss, Michael J. Elser, Johannes Bernardi, and Oliver Diwald. Stability and photoelectronic properties of layered titanate nanostructures. *Journal of the American Chemical Society*, 131(17):6198–6206, May 2009. 85

[91] Q. Chen, W. Zhou, G.H. Du, and L.-M. Peng. Trititanate nanotubes made via a single alkali treatment. *Advanced Materials*, 14(17):1208–1211, 2002. 85

[92] N. A. Kotov, F. C. Meldrum, C. Wu, and J. H. Fendler. Monoparticulate layer and Langmuir-Blodgett-Type multiparticulate layers of Size-Quantized cadmium sulfide clusters: A Colloid-Chemical approach to superlattice construction. *The Journal of Physical Chemistry*, 98(11):2735–2738, March 1994. 85

[93] Takayoshi Sasaki and Mamoru Watanabe. Semiconductor nanosheet crystallites of Quasi-TiO2 and their optical properties. *The Journal of Physical Chemistry B*, 101(49):10159–10161, December 1997. 85

[94] Takayoshi Sasaki, Yasuo Ebina, Katsutoshi Fukuda, Tomohiro Tanaka, Masaru Harada, and Mamoru Watanabe. Titania nanostructured films derived from a titania Nanosheet/Polycation multilayer assembly via heat treatment and UV irradiation. *Chemistry of Materials*, 14(8):3524–3530, 2002. 85

[95] Alessandro Antonello. *Multifunctional Nanostructured Materials Based on CdSe and TiO2 Nanoparticles*. PhD thesis, University of Padova, Padova, 2009. 86, 88

[96] BD Terris, L Folks, D Weller, JEE Baglin, AJ Kellock, H Rothuizen, and P Vettiger. Ion-beam patterning of magnetic films using stencil masks. *APPLIED PHYSICS LETTERS*, 75(3):403–405, July 1999. 93, 97

[97] C. Chappert, H. Bernas, J. Ferr, V. Kottler, J.-P. Jamet, Y. Chen, E. Cambril, T. Devolder, F. Rousseaux, V. Mathet, and H. Launois. Planar patterned magnetic media obtained by ion irradiation. *Science*, 280(5371):1919 –1922, June 1998. 93, 102

[98] T. Devolder, C. Chappert, Y. Chen, E. Cambril, H. Bernas, J. P. Jamet, and J. Ferre. Sub-50 nm planar magnetic nanostructures fabricated by ion irradiation. *Applied Physics Letters*, 74(22):3383, 1999. 93

[99] M. A Green, University of New South Wales. Centre for Photovoltaic Devices, and Systems. *Silicon solar cells : advanced principles & practice / Martin A. Green*. Centre for Photovoltaic Devices and Systems, University of New South Wales, Kensington, N.S.W. :, 1995. 94

[100] Jianhua Zhao, Aihua Wang, Martin A. Green, and Francesca Ferrazza. 19.8% efficient honeycomb textured multicrystalline and 24.4% monocrystalline silicon solar cells. *Applied Physics Letters*, 73(14):1991, 1998. 94, 102

[101] James F. Ziegler. SRIM-2003. *Nuclear Instruments and Methods in Physics Research Section B: Beam Interactions with Materials and Atoms*, 219-220:1027–1036, June 2004. 95

[102] G. Ctistis, E. Papaioannou, P. Patoka, J. Gutek, P. Fumagalli, and M. Giersig. Optical and magnetic properties of hexagonal arrays of subwavelength holes in optically thin cobalt films. *Nano Letters*, 9(1):1–6, January 2009. 102

[103] M.A Wood. Colloidal lithography and current fabrication techniques producing in-plane nanotopography for biological applications. *Journal of the Royal Society Interface*, 4(12):1–17, February 2007. PMID: 17015295 PMCID: 2358954. 102

[104] X.D. Hoa, A.G. Kirk, and M. Tabrizian. Towards integrated and sensitive surface plasmon resonance biosensors: A review of recent progress. *Biosensors and Bioelectronics*, 23(2):151–160, September 2007. 102

[105] WA Nositschka, C Beneking, O Voigt, and H Kurz. Texturisation of multicrystalline silicon wafers for solar cells by reactive ion etching through colloidal masks. *SOLAR ENERGY MATERIALS AND SOLAR CELLS*, 76(2):155–166, March 2003. 102